Shaping Spatial and Temporal Gradients during the Development of *Caenorhabditis elegans*: an Antagonistic Balance

by

Dong hyun Kim

B.S. in Physics
Yonsei University, 2006

Submitted to the Department of Physics
in partial fulfillment of the requirements for the degree of

Doctor of Philosophy in Physics

at the
Massachusetts Institute of Technology

June 2012

Signature of author : _____
Department of Physics
May 4, 2012

Certified by : _____
Alexander van Oudenaarden
Professor of Physics and Biology
Thesis Supervisor

Accepted by :_____
Krishna Rajagopal
Professor of Physics
Associate Department Head for Education

Shaping Spatial and Temporal Gradients during the Development of *Caenorhabditis elegans*: an Antagonistic Balance

by
Dong hyun Kim
submitted to the Department of Physics
on May 4, 2012, in partial fulfillment of
the requirements for the degree of
Doctor of Philosophy in Physics

Abstract

How the tissues of a developing organism are reproducibly patterned has been a major question in biology. Under adequate conditions, a single fertilized cell can generate a full variety of mature cell types and organize them into a developed organism. In order to accomplish these complex tasks of self-organization, positional and temporal information must be provided to individual cells to ensure that the right developmental events occur at appropriate times. This is at least partially assisted by the specification of spatial and temporal axes formed and maintained during development. One way to define position and time within a developing organism is to form spatial or temporal gradients of signaling molecules, which patterns tissues in a concentration-dependent manner. A critical challenge of such gradient based patterning mechanisms is to maintain the desired gradient profiles of signaling molecules in a heterogeneous and fluctuating cellular environment. In this thesis, I describe how spatial and temporal gradients of signaling molecules can be refined and maintained during development of the model organism *Caenorhabditis elegans*. Using quantitative measurement techniques and analyses, I find that such tasks can be achieved by the balance between the activities of gradient forming signaling molecules and their antagonistic counterparts.

Thesis supervisor: Alexander van Oudenaarden
Title: Professor of Physics and Biology

Acknowledgments

First, I would like to thank my thesis supervisor Alexander van Oudenaarden, who welcomed me to join his research group twice, first when I came to MIT and later when I returned to him after spending 10 months in a different group only to realize how important it is to have an understanding person as a mentor during one's graduate study. Alexander was not only an inspiring scientist who had extraordinary visions and the passion towards science, but also an outstanding mentor who listened and showed respect to his student as an independent person. Five years ago, Alexander generously allowed me to spend months reading introductory cell biology textbooks because I knew no biology. I still remember the time when Alexander kindly brought me to his lab bench to teach me how to spread bacterial cells on an agar plate with pasteur pipettes. When I was struggling with personal issues and not focusing on my research project, Alexander let me take my time off rather than taking my name off his group. I will always be privileged that I had worked with Alexander.

I sincerely thank my thesis committee members, Dr. Mehran Kardar, Dr. Jeff Gore and Dr. Bob Horvitz for their support and advice throughout my graduate years. I also sincerely thank my collaborators, Dr. Adam Saffer, and Dr. Rik Korswagen and Dr. Martin Haterink.

I am indebted to the previous and current members of the van Oudenaarden group. Jeff Gore was also a great mentor especially during my earlier times at MIT. Jeff taught me how to do good science and I learned how to become a successful scientist and person by watching how Jeff did. I hope I made a significant enough contribution to this promising scientist's life by helping him meet his wife Sena. Christoph Engert and Apratim Sahay were the two fellow graduate students and good friends who not only shared the excitement of worm biology, but also personal emotions, student hardships and fun. Jeroen van Zon, Rui zhen Tan and Miaoqing Fang were funny and friendly office mates who made me realize what the truth of life was and who also made me laugh a lot. I will not forget Gregor Neuert, another incredibly warm hearted post-doc, who spent six years together since we joined the lab in the same year. My graduate life would not have been successful without these tremendous people.

I would also like to thank some of my Korean fellow students and post-docs at MIT: Taesin Kwak, Hongchul Jang, Hyowon Gweon, Andre Sungho Yoon, Jeewoo Lim, Woonju Song, Jeewoo Park, Sungmin Son, Wonjung Kim, Wonjoon Choi, Jeong Gon Son, Johnny Hyungryul Choi. I thank you for your sincere support throughout my graduate years.

My friends, Junggil Kim, Taewoo Kim and Joongoo Lee, I will be indebted to you for the rest of my life for your never-ending support. And of course, my cousins, Boony, Hyukjin, Nany and Juyun, thank you for your warmth. Thank you my brother, Dong hee, for mental support and fun chats on the phone. And finally my parents, you are the reason I exist and thank you for your love, endless support and encouragement. I will always love you.

Table of contents

Chapter 0. Motivation

> *Quantification had never been applied to studies on inheritance before Mendel's work (1856-1863). – Griffiths et al., Introduction to Genetic Analysis 8th ed. W. H. Freeman and Company (2005).*

In the mid-nineteenth century, an Austrian monk, Gregor Mendel, performed historical experiments in his monastery's two hectare garden which led him to discover the pattern of inheritance. Mendel first bred pure lines of garden peas with different characters, such as petal color, seed shape, *etc*. A pure line is a population of species which shows no variation in one or more particular characters of study. He then either self- or cross-pollinated peas with different characters and investigated the characters of their offspring. Based on his observations, Mendel creatively deduced a model that seemed to govern the patterns of (autosomal) inheritance, which contained important concepts that are still valid nowadays such as the existence of hereditary particles (*genes*) and that they usually form pairs (*alleles*) but gametes can only carry one of each pair with random chance.

What had led Mendel to these brilliant insights and made him the founder of genetics was his quantitative experimental and analytical approach: he *counted* the numbers of offspring with each character(s) and found what is now known as the *3:1 or 9:3:3:1 Mendelian ratios*. Others before Mendel have also obtained similar results but it was Mendel alone who succeeded in quantifying the data to come up with a solid and accurate understanding of heredity variations.

Scientific advances have been indeed inevitably influenced by the development of advanced measurement techniques with unprecedented resolutions and scales. It was the development of atomic clocks with great temporal precision that had allowed physicists to test gravitational time dilation the theory of general relativity have long predicted. Particle physicists are hoping that with the world's largest high-energy particle accelerator LHC (Large Hadron Collider), the mystery of the theoretical Higgs

particle will be solved which will expand our understanding of the existence of mass. Due to its enormous complexity and lack of high-resolution measurement techniques, biological science has historically remained relatively qualitative. However, the use of green fluorescent protein (GFP) as a tool for molecular biology which only began in the 1990's [1], has provided opportunities for quantifying gene expression levels in individual cells and revolutionized our understanding of the control of the intrinsically variable, or noisy, gene expression [2]. During the last decade, the use of high-precision laser and optical traps in biology has allowed us to visualize how molecular motor proteins walk along their intracellular tracks and even measure their nanometer-scale step sizes [3]. Nowadays, numerous highly sensitive and high-throughput technologies are being developed and used, and the number of new exciting biological reports is growing faster than ever. The better we see, the better we understand.

In this thesis, we attempt to demonstrate this simple truth by taking advantage of state-of-the-art measurement techniques and using novel data quantification approaches to revisit some of the classic but still the most dynamic and sophisticated biological phenomena – the process of animal development, focusing on how the spatial and temporal axes are controlled and maintained using the nematode *Caenorhabditis elegans* as a model organism.

Chapter 1. Global axis specification in animal development

1.1 Building an organism – placing the right cell at the right location at the right time

Life of any multi-cellular organism begins as a zygote, or a fertilized egg. It is a single cell that has the ability to give rise to every type of cell in the adult body (totipotentcy). Inside the nucleus of this cell is the genome, a long DNA sequence which carries both a list of building parts and instructions on how to build an organism, which drives this single cell to undergo numerous symmetric and asymmetric divisions and fate diversifications to reach maturity. The result is what we call “an organism”, a structurally organized heterogeneous group of cells forming spatially segregated functional units, such as tissues and organs that interact with one another to maintain the life of their host. Surprisingly, each cell of an adult organism exhibits unique gene (more specifically, protein) expression signatures and chromatin states representing its commitment to a particular cell type and function, even though the genomic contents are identical. Such cell diversification process is called *development* and it involves an orchestration of genetically programmed molecular events which continuously controls growth, differentiation and migration of individual cell to reach a desired structure.

All multi-cellular organisms regardless of their shapes face the same fundamental challenge during development: cells of distinct types and functions must be generated at an appropriate number and must be positioned at proper locations. Furthermore, this process should not risk the organism’s survival. It seems that evolutionary forces have led multi-cellular species to not only come up with a robust mechanism for such tasks, but also to perform optimally under certain fitness constraints. For instance, stem cells in the developing intestinal crypt divide asymmetrically to give birth to a differentiated cell only at the end of tissue formation in order to spend the minimal amount of time to

generate functional intestine, which seems crucial for survival of a fetus [4]. Every developing cell knows where and when to undergo rounds of symmetric or asymmetric divisions and terminate its cell cycle and undergo morphogenesis, what specific type of cell fate to commit to form tissues and organs. Often, cells know when and where to commit suicide (programmed cell death) for the sake of structure formation [5]. Normal animals do not have gut cells growing in their brains. Terrestrial animals are born after their lungs are formed so that they can breathe air, which would otherwise be detrimental.

Here, we ask how these developmental patterning processes can be achieved. Do cells have precise measures of reading out (1) their own positions with respect to the body as a whole and (2) at which developmental stage they are in, before making any commitment to specific cell fates and undergo morphogenesis?

1.2 Formation of body axis – setting up spatial gradients

Extensive comparative studies across multi-cellular model organisms, such as flies, worms, frogs and mice have revealed a hierarchical sequential spatial patterning strategy, which is consistently found throughout species:

1. Initial spatial symmetry-breaking of an oocyte by external / environmental polarizing cues, such as sperm entry or extra-embryonic tissues → localization of critical regulatory proteins and cytoplasmic rearrangement
2. Anterior-posterior (AP) and dorsal-ventral (DV) body axes specification and maintenance (*e.g.*, generation of morphogenetic field and its refinement via inhibitors and shuttling proteins) → *generation of body axis* → generation of position-dependent precursor cell types in broad length scales

3. Finer patterning of group of cells in shorter length scales by interactions between neighboring cells or lineage-dependent fate adoptions.

The initial formation of body axis of an organism is triggered by symmetry-breaking events at very early stages of development, and they are sufficient to elaborate full regional diversity of adult organism at the end. In *Drosophila*, polarity of an oocyte is determined by the structure of its surrounding ovary during early oogenesis [6]. The *C. elegans* oocytes are also polarized as they pass through the oviduct before fertilization, but studies have shown that the site of sperm entry can override the original AP axis establishment: no matter where the sperm enters, it is one of the two poles closer to this site which becomes the posterior pole [7]. Once this polarity is established, long-range signaling mechanisms (*e.g.*, formation of morphogenetic gradients) function to set up "body axes" to confer positional information of each cell within the developmental field (a set of cells forming a developing structure) throughout the rest of animal development.

Early pioneering works in morphogenetic fields largely involved micro-surgical transplantation studies performed in developing embryos. Puzzling and rather contradictory experimental results were emerging in the late 19th century. For instance, scientists have noticed a salamander egg growing into an animal with two heads when the blastomeres of a fertilized egg were constricted. When one of the two blastomeres was killed, the remaining one developed into a half embryo. In contrast, when the blastomeres in an embryo of the same stage were separated, each fully developed into individual animals with reduced sizes. It was Han Spemann (1869-1941), a German experimental embryologist renowned for his constriction experiments who soon realized that the outcomes of such disruptions were strongly dependent on the direction (or plane) of such disruptions. Later on, he transplanted different parts of a developing embryo into another site of a different embryo and found that there exist areas that are capable of inducing particular parts of an animal. Spemann called these areas "organiser centres", and hypothesized that they produce molecules that induce developmental responses in surrounding tissues [8]. This was the beginning of our understanding of diffusive-chemical-dependent tissue type segregation in developing

embryos (without any molecular details at that time!) which triggered theoretical studies of morphogens such as that of Turing's in the mid 20th century, which hypothesized that instabilities in homogenous medium can create patterns [9].

In recent years, advanced molecular genetic studies have started to allow an unprecedented understanding of morphogenetic pathways. Most importantly, the emergence of biological imaging techniques such as *in situ* hybridization, immuno-fluorescence techniques, and fluorescent protein tags allowed direct semi-quantitative visualization of morphogenetic gradients in tissues [10] (Figure 1.1 A-B). Indeed, the observations so far support the model that the concentration gradients generated by these diffusive morphogen molecules secreted from a local specialized group of cells act as a source of positional information which the remainder of cells in the body receives. This so called "Synthesis-Diffusion-Degradation (SDD)" model predicts the formation of an exponentially decaying morphogenetic gradient profile [11] (Figure 1.1C). The gradients of these molecules can typically span from few to dozen cell diameters. Each cell within the morphogenetic field receives and interprets the resulting region-specific concentrations (in some cases, local gradients or duration of exposure) of one or more of these morphogens [12]. This results in transcriptional responses leading to executions of the corresponding developmental programs (*e.g*., commitment to become a certain precursor cell type).

A handful of gene families encoding diffusive signaling pathway molecules have been identified in different organisms, such as Bicoid and Hunchback from *Drosophila*, BMP (bone morphogenetic protein) from *Xenopus*, Wnt, from other higher organisms which specifies AP axis, and Sonic Hedgehog from mammals, Dorsal in *Drosophila* which specifies DV axis [11,13,14]. The source location can be set by local deposition of maternally contributed factors (*e.g.*, *bicoid* mRNA in *Drosophila* embryos [15]), or by a lineage-dependent expression of related genes in a spatially limited group of cells.

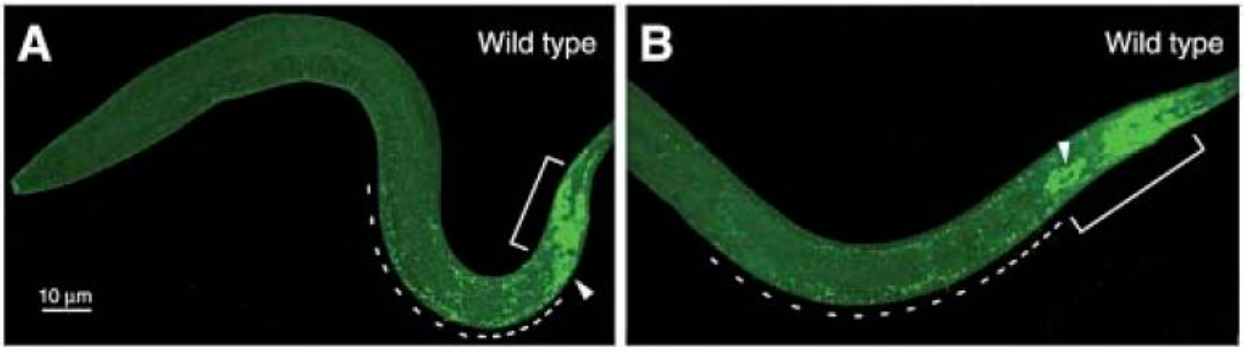

C

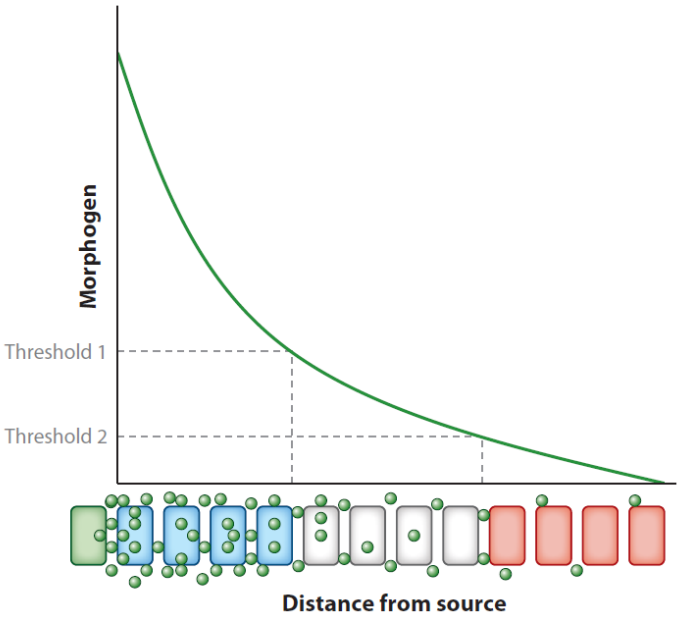

Figure 1.1 (A)-(B) Posterior EGL-20/Wnt gradient is visualized in *C. elegans* hatchlings carrying *Pegl-20::egl-20::proteinA* transgene. White bars delimit the group of *egl-20* expressing cells and dashed lines represent the range of gradient. Figure adopted from Damien Y. M. Coudreuse, *et al.*, Wnt gradient formation requires retromer function in Wnt-producing cells. *Science* **312**, 921-924 (2006) [16]. (C) A schematic of morphogenetic gradient activity in one dimensional tissue. This is so-called the French flag model. Figure adopted from Rogers, K. W. and Schier, A. F. Morphogen gradients: from generation to interpretation. *Annu Rev. Cell Dev. Biol.* **27**:377-407 (2011) [11].

Our current knowledge on the formation of morphogen gradient is, however, still incomplete to devise general principles. For instance, it is not entirely clear how morphogen molecules move and several possible models exist. They can either diffuse through extracellular space, or can undergo planar transcytosis, or perhaps both depending on the developmental context [13]. Differential morphogen receptor expression can transform the original morphogenetic gradient into a completely different downstream signaling pattern in space. Sensitive live imaging technologies have revealed dynamic Dorsal gradient and its target gene expression, suggesting a signal time averaging mechanism [17]. Moreover, additional mechanisms and related molecular factors such as morphogen inhibitors and transporters have been recently discovered and characterized in *Drosophila*. Given the highly conserved signaling pathways throughout species, it is likely that morphogen activities would depend on many different factors that are still waiting to be discovered.

1.3 Refinement of spatial gradients

The SDD model provides a simple intuitive explanation of the body axis generation mechanism during animal development. According to the SDD model, the morphogenetic gradient is an exponentially decaying function which depends on two physical properties: diffusion constants and lifetimes of morphogens in extracellular environments. However, diffusion and degradation alone are not sufficient to explain the robustness of patterning observed in nature [18]. Even though the rates of biochemical processes such as protein production are intrinsically variable and embryos are never identical in size, the developmental patterning of isogenic animals is nevertheless organized and stereotyped. This suggests that these gradients are tightly controlled by additional regulatory mechanisms. Indeed, nonlinear processes capable of providing robustness to spatial patterning processes have been discovered and characterized [19]. For example, BMP gradient can be robustly scaled via active shuttling and self-enhanced degradation to compensate for variability in the size of

Xenopus embryos [18,20]. In addition, local expression of diffusive or membrane-bound proteins which are often morphogen receptors themselves can inhibit morphogenetic activities by ligand sequestration or by other regulatory feedback mechanisms which suppress its downstream signaling [21]. This provides means to modulate local morphogenetic activities and allows extra freedom of refining the overall spatial gradient. Although there is yet no evidence, such antagonistic layers of regulation might also play a role in robust developmental patterning [22].

Because of aforementioned reasons, understanding the mechanisms of generating and fine-tuning of morphogenetic spatial gradients not only requires the knowledge about interactions among the underlying protein machineries, but also a detailed map of where and how much those relevant genes are expressed. In chapter 2 and 3, we use a novel sensitive mRNA *in situ* hybridization method [23] to characterize the dynamic expression patterns of Wnt morphogen encoding genes, and discuss a novel gene encoding secreted proteins that inhibits Wnt morphogen activity by forming opposing gradients in *C. elegans.* With this method, we obtained absolute endogenous mRNA levels of Wnt genes at the single cell resolution and avoided artifacts of previously used exogenous reporters which often lacked unidentified key regulatory elements such as untranslated regions (UTRs), intronic sequences, etc. The forthcoming abundance of such mechanisms will clearly reflect the importance of accurate primary body axis formation during early development – since ill-positioned precursor cells will “pre-curse” its numerous daughter cells to adopt undesired cell fates.

1.4 Tracking developmental time – setting up temporal gradients

> *“The only reason for time is so that everything doesn’t happen at once.”*
> *– Albert Einstein (1879-1955)*

At the event of fertilization of an oocyte, developmental time begins. The entry of a sperm not only sets up the early spatial gradients, but it also initiates the cell cycle of the zygote. During development, this single cell continuously divides and its daughter cells undergo numerous developmental events, such as migration, differentiation and programmed cell death in proper order at precise times (as well as at proper locations, as described above) to result in a fully organized animal at the end. It is possible that the timing of developmental events result from a cascade of biochemical processes and simply “appears” to be scheduled due to relatively constant times required for one biochemical process to occur before the execution of the next, and so on. Supportively, raising the culturing temperature tend to increase developmental rates of many species. However, given the intricacy of animal development in general as well as the stochastic nature of molecular interactions and environmental fluctuations organisms can encounter at any random time, it is difficult to conceive how such robust orchestration of developmental events in individual animals in almost all species can be achieved. In fact, phenotypic characterizations of mutations in certain developmental genes have demonstrated that the order of their execution can be altered without any effect on the integrity of the program itself, implying fundamental modularity might exist in developmental programs [24]. In this case, a separate cell autonomous or centralized time keeping mechanism must exist to assist the ordering and timing of such modular developmental programs. How could a developing organism track developmental time? What are the temporal patterning mechanisms? Timing mechanisms in living systems, so-called biological clocks, have been typically classified into two classes based on the dynamics: oscillatory clocks and hourglass clocks [25].

Oscillatory clocks

Cyclicity is probably the most fundamental and widespread temporal pattern in life. In every living cell, feedback controls of various metabolic pathways, forming a “metabolic cycle”, are critical for metabolic homeostasis [26]. An oscillatory clock is usually referred to a free-running cyclic molecular process which can drive periodic biological events. When the level of a “time-keeper” molecular substance is above a certain

threshold, a corresponding biological event is triggered and this can repeat regularly as the substance level increase and decrease periodically around the threshold (Figure 1.2a). For example, cells periodically replicate and divide for reproduction with the frequency controlled by cyclic waves of cell cycle gene expressions: a cell cycle clock [27]. Circadian clocks regulate numerous metabolic and reproductive activities of an organism [28,29] and allows better adaptation to the environment by being synchronized to the periodic switching of days and nights, keeping its period approximately 24 hours. Rhythmic activities of individual cells are inevitably coupled to environmental conditions, or "*zeitgebers*" which are external synchronization cues for endogenous clocks, such as daylight which keeps our circadian clock on track every day [30]. Behaviors of species ranging from insects to mammals are often influenced by circadian rhythms. Nutrient availability and temperature obviously have strong influence on the speed of cell cycle clocks [31].

Studies have suggested that oscillatory biological clocks might play a crucial role in multi-cellular organism development. Common regulation of circadian clock activities and developmental timing has been observed in *D. Melanogaster* [32]. Notably, many of the clock protein orthologs in *C. elegans*, including LIN-42 which exhibits an oscillatory expression dynamics, are also involved in development and developmental timing [33]. Nuclear hormone receptors (NHR) exhibiting oscillatory mRNA abundance are critical regulators of molting process in *C. elegans* [34]. In fact, cyclic gene expression is widely observed in animals and plants and it may reflect the underlying fundamental reiterative aspect of normal development [35].

There are also frequently observed mechanisms in animal and plant development which can convert oscillatory temporal signals into spatial patterns. For example, spatial segmentation during vertebrate somitogenesis is achieved by the dynamic wavefront formation of oscillatory *hairy* expression which provides a template for the repetitive spatial patterning [36]. Similarly, during *Arabidopsis* root growth the pre-branch sites are marked by cyclic expression pulses of gene expression as the root extends [37].

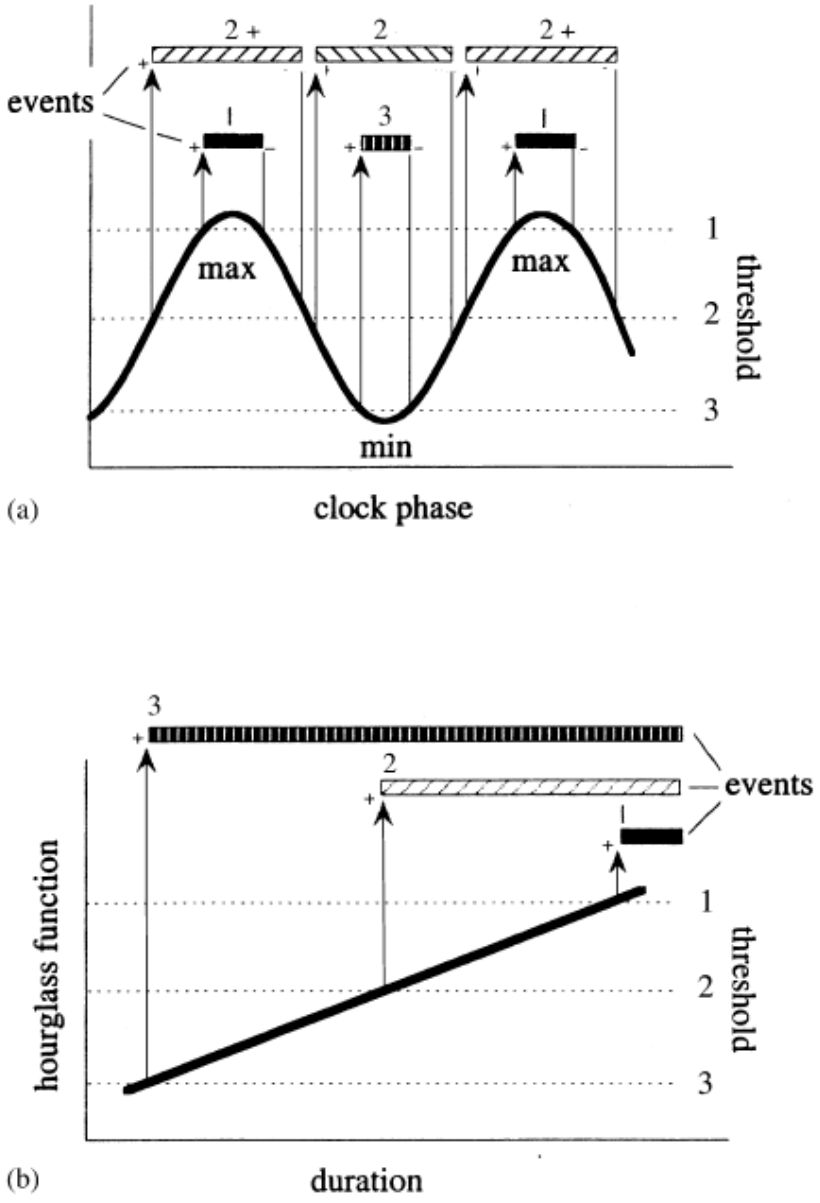

Figure 1.2 Triggering of events (a) by an oscillatory clock and (b) by an hourglass clock. Multiple events can be triggered at different thresholds (1, 2, 3). Figure adopted from Rensing, L., Meyer-Grahle, U. and Ruoff, P. Biological timing and the clock metaphor: oscillatory and hourglass mechanisms. *Chronobiology Intl*. **18**(3), 329-369 (2001) [38].

Hourglass clocks

Development, however, is a uni-directional irreversible process. It is more than a reiterative process that requires a temporal “direction” to sequentially execute different developmental programs at desired times. It is unlikely that monotonous rhythmic signals alone could provide such information. An hourglass clock can provide temporal direction by utilizing a continuous accumulation or dispersion of a “time-keeper” substance which functions as sand in an hourglass. Hourglass clocks can therefore measure the duration of time by triggering events or processes when the amount of certain substance or variable reaches threshold values (Figure 1.2b). Interestingly, a handful of observations from studies of animal and plant development suggest that certain developmental programs of higher organisms have evolved to realize such hourglass clocks by utilizing the cyclic properties of various underlying cellular processes. A well established example is the mid-blastula transition. During the embryogenesis of insects and vertebrates, zygotic transcription is activated when the nucleo-cytoplasmic ratio reaches a certain threshold [39], indicating the existence of a cell cycle counting mechanism built into early developmental programs. *Hayflick phenomenon* is another similar example, where the division of somatic cells ceases when the length of shortening telomere reaches a threshold [40]. Aging of a cell is also considered to some extent a process timed by accumulation of DNA damage.

It can be argued that cells passively figure out when to carry out specific tasks by counting the number of divisions it went through, because in many cases of development cells undergo a defined number of divisions. However, such mechanisms have not been reported and moreover, experimental results in *C. elegans* have demonstrated that the expression timings of several differentiation marker genes do not depend on cell cycle progression [41]. Therefore, it has been suggested that there exists an intrinsic developmental time counting mechanism that is independent from cell cycles or other downstream developmental programs.

An active way to time developmental events is to create a temporal gradient of signaling molecules [42]. Perhaps the only known characterized examples to date are the members of the *C. elegans* “heterochronic” pathway [43] which form temporal gradients

and specify the timing of larval stage specific developmental events. During early post-embryonic development, a decreasing temporal gradient of the nuclear protein LIN-14 [44,45] and the cytoplasmic protein LIN-28 [46] sequentially triggers dosage-dependent larval stage-specific programs. During later development, a novel RBCC (Ring finger-B box-Coiled coil) protein LIN-41 forms a decreasing temporal gradient and triggers larva-to-adult transition which involves cell cycle termination [47]. Genetic analyses and expression level studies have demonstrated that cells in wild-type animals can distinguish distinct levels of heterochronic gene activity at specific times during post-embryonic development to execute corresponding developmental programs [44].

1.5 Refinement of temporal gradients

At the molecular level, the robust performance of biological clocks implies that expression levels of these time-keeping genes must be tightly controlled, effectively dampening any fluctuations that can potentially perturb the temporal expression patterns. Cell cycle clock studies have demonstrated to some extent how oscillatory networks can control their own robustness [48,49], but it is barely understood how hourglass clocks can function robustly. Despite the fact that the *C. elegans* heterochronic genes *lin-14*, *lin-28* and *lin-41* are the first and the most extensively characterized temporal gradient forming genes, mechanisms that control the onset of their expressions and how the integrity of these temporal gradients are maintained are largely unexplored. In principle, temporal integrity of developmental events can be disrupted in many possible ways which may result in misplacement of cells or induction of wrong cell fates at wrong times, risking the overall fitness of an organism. For instance, Intrinsic fluctuations due to stochastic nature of molecular events [50] or extrinsic fluctuations due to environmental fluctuations or random partitioning of molecular components during cell divisions can randomize the dosage of developmental timing genes. Also, coupling or crosstalk can exist between different developmental gene expression programs, given the hierarchical architecture of eukaryotic genome

where change in the level of a typical transcription factor, can affect the expression of many different genes [51]. Any dynamical processes that are involved in developmental processes could potentially introduce fluctuations.

With no doubt, a detailed understanding of how the temporal gradients of dose-sensitive developmental regulators are robustly shaped requires precise measurement of its expression dynamics. However, accurate quantification of gene expression has been challenging due to technical limitations of traditional RNA quantification assays such as Northern blotting and RT-PCR. Moreover, cellular resolution is lost because these methods require lysis. As mentioned earlier, reporter constructs are often not reliable because they lack unidentified endogenous genetic regulatory elements and they differ in lifetime characteristics. In chapter 4, we circumvented these limitations by counting individual developmental time keeping gene transcripts in intact *C. elegans* larvae using a single molecule fluorescence *in situ* hybridization method [23]. We also used each animal's body length as a measure of developmental age to obtain temporal information from fixed specimen. By simultaneously obtaining "molecule count" and "body length" information, we were able to measure the number of mRNA molecules in an animal at a particular age, thereby allowing us to map a gene's expression dynamics during larval growth. We report a new regulatory mechanism that actively insulates a temporal gradient of developmental gene expression from global transcriptome fluctuations – analogous to noise-cancelling headphones from Bose^{TM} that actively filters out ambient noise.

Chapter 2. Opposing gradients of morphogen and its inhibitor control cell migration

This work was published in *Development* **138**, 2915 (2011), in collaboration with Korswagen group at the Hubrecht Institute, the Netherlands. The paper was titled “Neuroblast migration along the anteroposterior axis of *C. elegans* is controlled by opposing gradients of Wnts and a secreted Frizzled related protein - Martin Haterink**, Dong hyun Kim**, Teije C. Middelkoop, Thang Dinh Doan, Alexander van Oudenaarden and Hendrik C. Korswagen”.

** These authors contributed equally to this work. My contribution to this study was to conceive, design, perform and analyze single molecule RNA *in situ* hybridization experiments.

The migration of neuroblasts along the anteroposterior body axis of *C. elegans* is controlled by multiple Wnts that act partially redundantly to guide cells to their precisely defined final destinations. How positional information is specified by this system is however still largely unknown. Here, we used a novel fluorescent *in situ* hybridization method to generate a quantitative spatio-temporal expression map of the *C. elegans* Wnt genes. We found that the five Wnt genes are expressed in a series of partially overlapping domains along the anteroposterior axis, with a predominant expression in the posterior half of the body. Furthermore, we show that a secreted Frizzled related protein is expressed at the anterior end of the body axis, where it inhibits Wnt signaling to control neuroblast migration. Our findings reveal that a system of regionalized Wnt gene expression and anterior Wnt inhibition guides the highly stereotypic migration of neuroblasts in *C. elegans*. Opposing expression of Wnts and Wnt inhibitors has been observed in basal metazoans and in the vertebrate neurectoderm. Our results in *C. elegans* support the notion that a system of posterior Wnt signaling and anterior Wnt inhibition is an evolutionarily conserved principle of primary body axis specification.

2.1 Introduction

Wnt proteins control many aspects of metazoan development, with prominent functions in cell fate determination, cell proliferation and cell migration [52]. The activity of Wnt proteins is counteracted by a range of inhibitors, including secreted proteins such as the secreted Frizzled related proteins (SFRPs) [22,53] and Dickkopf [54], and intracellular inhibitors such as the TCF/Lef transcription factor Tcf3 [55]. During neurectoderm development in vertebrates, these inhibitors are expressed in the anterior and counteract the activity of posteriorly expressed Wnts to enable the formation of anterior brain structures and the eyes [53,56,57]. Opposing expression of Wnts and Wnt inhibitors has also been observed in basal metazoan organisms such as the cnidarians *Hydra* and *Nematostella vectensis* [58–61] and in the planarian *Schmidtea mediterranea* [62], which led to the hypothesis that a system of posterior Wnt signaling and anterior Wnt inhibition is an ancient mechanism that may be used across animal phyla to pattern the primary body axis [63].

The nematode *Caenorhabditis elegans* expresses five different Wnt proteins that control many aspects of development, including cell fate specification, cell polarity and the highly stereotypic migration of neuroblasts along the anteroposterior body axis [64,65]. Neuroblasts that migrate in a Wnt dependent manner include the HSN neurons, which migrate from the posterior to the mid-body region [66–68], the ALM and CAN neurons, which migrate from the anterior to positions in the mid-body region [66,67,69] and the Q neuroblast descendants, which migrate in opposite directions on the left and right lateral sides [70,71]. With the exception of the left Q cell descendants, the migration of these neuroblasts is controlled through multiple, partially redundantly acting Wnt proteins [72] . The expression patterns of the *C. elegans* Wnt genes have been analyzed using transgenic reporter constructs. These studies revealed a predominantly posterior expression for the Wnt genes *lin-44*, *egl-20* and *cwn-1* [68,73,74], whereas *mom-2* and *cwn-2* were reported to be generally expressed along the anteroposterior axis [75], with a more prominent expression of *cwn-2* in the pharynx and anterior muscle cells [76,77]. Although there is a large degree of overlap between the reported

expression patterns, there are also important differences in the extent of expression along the anteroposterior axis and in the specific cell types that are involved, complicating the analysis of Wnt gene function in neuroblast migration and other aspects of development.

Here, we used single molecule mRNA fluorescent *in situ* hybridization (smFISH) to quantitatively determine the spatio-temporal expression patterns of the five *C. elegans* Wnt genes. Our results show that the different Wnt genes are expressed in a series of partially overlapping expression domains, with a predominant expression in the posterior body half and a single Wnt gene with an anterior expression domain. Furthermore, we show that the *C. elegans* genome contains a single SFRP ortholog that is specifically expressed at the anterior end of the body axis. SFRP-1 functions as an inhibitor of Wnt signaling that represses the most anteriorly expressed Wnts to control the migration of neuroblasts in the anterior body region. Our results demonstrate that opposing Wnt and Wnt inhibitory activities are also key to anteroposterior patterning in *C. elegans* and provide further support for the evolutionary conservation of this system in primary body axis specification.

2.2 The five *C. elegans* Wnt genes are expressed in a series of partially overlapping domains along the anteroposterior axis

To quantitatively determine the spatio-temporal expression patterns of the five *C. elegans* Wnt genes, we performed single molecule mRNA FISH (smFISH) to measure endogenous transcript levels in staged larvae and during embryonic development [23]. Using this technique, we were able to simultaneously label and visualize individual transcripts of up to three Wnt genes as bright diffraction-limited fluorescent spots in animals with preserved shape (Fig. 2.1 A). Counting of these spots using a custom program written in MATLAB allowed us to measure transcript levels in any three-dimensional region of the animal (Fig. 2.1 B, C, F). These measurements revealed that the expression patterns of the five Wnt genes are strikingly reproducible in wild type animals of the same developmental stage (Fig. 2.1 A, F). In general, the overall

transcript expression profile of the different Wnt genes agreed with previous expression patterns obtained with transgenes expressing transcriptional or translational reporter constructs, but as detailed below, there were a number of important differences.

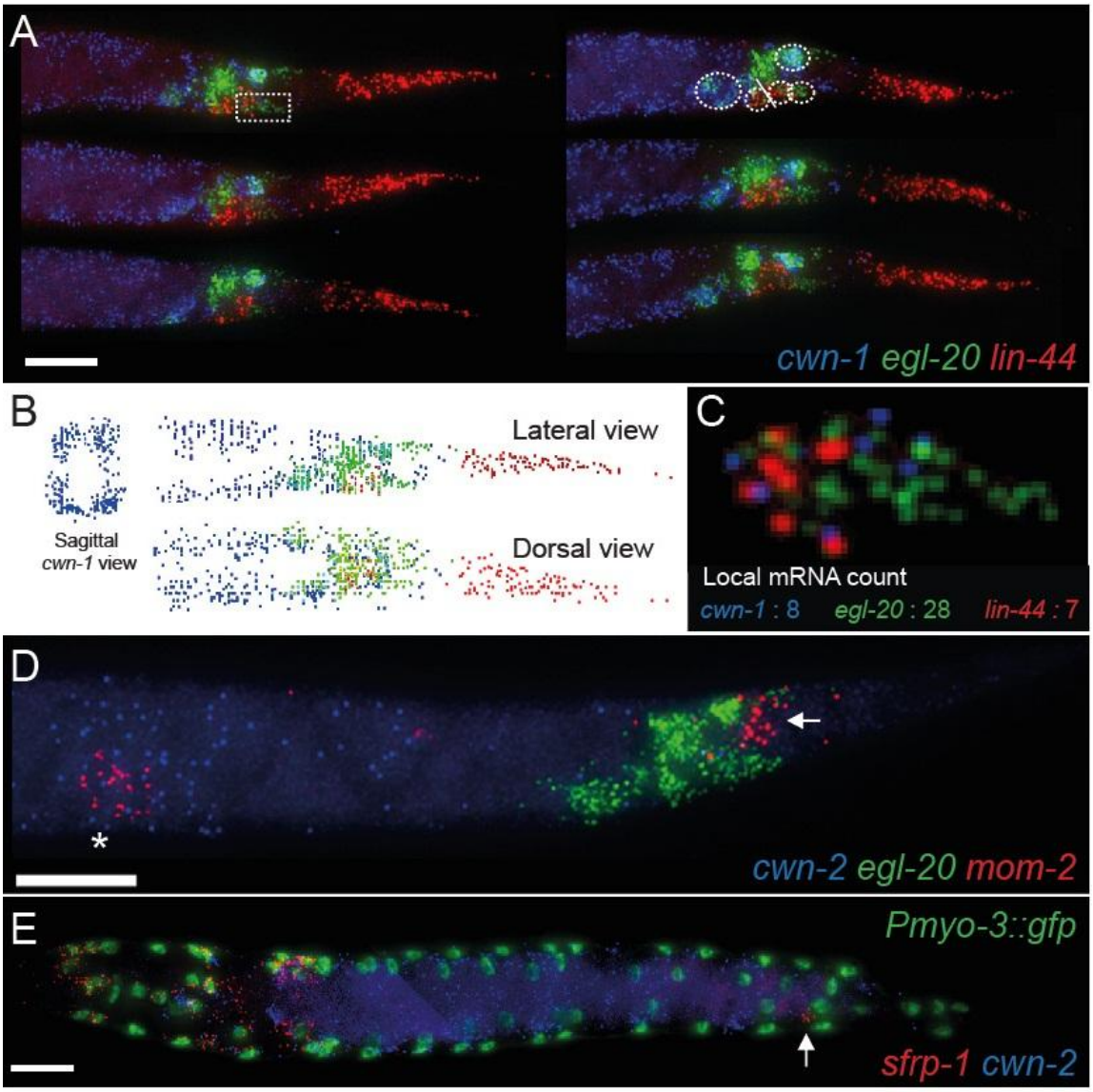
A
cwn-1 egl-20 lin-44
B
Lateral view
Dorsal view
Sagittal
cwn-1 view
C
Local mRNA count
cwn-1 : 8
egl-20 : 28
lin-44 : 7
D
*
cwn-2 egl-20 mom-2
E
Pmyo-3::gfp
sfrp-1 cwn-2
F
Number of smFISH spots
cwn-1
cwn-2
egl-20
lin-44
mom-2
sfrp-1
DAPI

Figure 2.1 Single molecule mRNA FISH analyses of the *C. elegans* Wnt genes and *sfrp-1* in staged L1 animals. Images are maximum intensity projections of lateral z-stacks. (**A**) Detection of *cwn-1*, *egl-20* and *lin-44* transcripts in the L1 larval tail of 6 individual animals. The indicated cells in the top right image are: top, the anal depressor muscle; from bottom left to right, P11/P12, Y, B and the body wall muscle cells VL23/VL24. The rectum is indicated by a solid line. Scale bar is 10 µm. (**B**) Transcript identification using a custom program written in MATLAB. A sagittal view of *cwn-1* smFISH spots shows predominant expression in the four body wall muscle quadrants. (**C**) Magnification of the area indicated in panel A. smFISH spot counts of *cwn-1*, *egl-20* and *mom-2* are indicated. (**D**) Expression of *cwn-2*, *egl-20* and *mom-2* in the posterior half of the animal. The asterisk indicates the Z2 and Z3 germ line precursor cells, the arrow the position of the tail cells that transiently express *mom-2*. Scale bar is 10 µm. (**E**) Expression of *sfrp-1* and *cwn-2* in an L1 larva. The nuclei of body wall muscle cells are highlighted by nuclear GFP. The posterior ventral nerve cord neuron expressing *sfrp-1* was identified as DA7 (indicated by arrow). Scale bar is 10 µm. (**F**) Quantification of Wnt and *sfrp-1* smFISH spots along the anteroposterior axis of early L1 stage larvae. A DAPI stained animal is included for orientation. For all images anterior is to the left and posterior to the right. Error bars indicate standard error of the mean (*cwn-1*, n=10; *cwn-2*, *egl-20* and *lin-44*, n=13; *mom-2*, n=6 and *sfrp-1*, n=9).

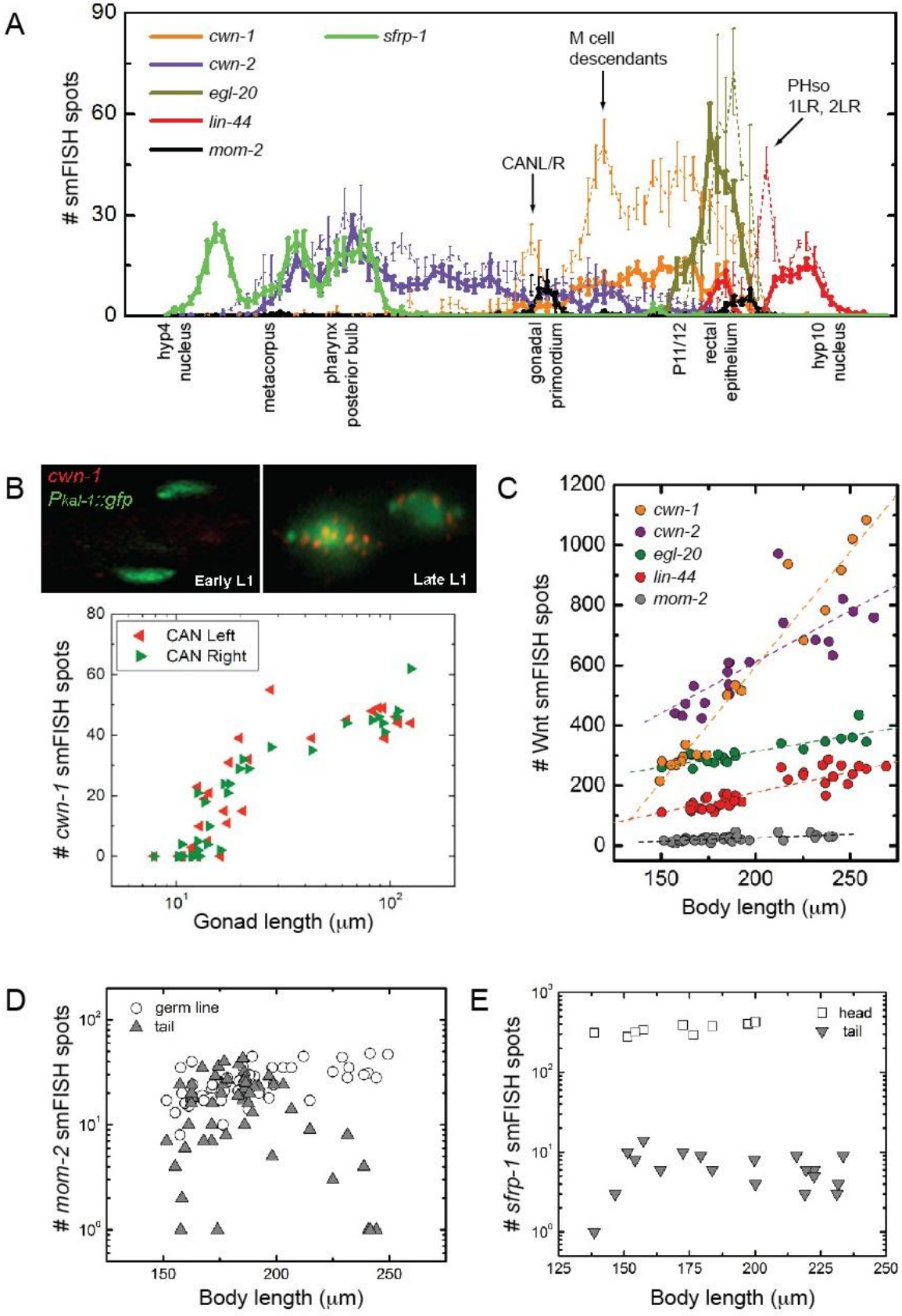
A
smFISH spots
cwn-1
cwn-2
egl-20
lin-44
mom-2
sfrp-1
M cell descendants
PHso 1LR, 2LR
CANL/R
hyp4 nucleus
metacorpus
pharynx posterior bulb
gonadal primordium
P11/12
rectal epithelium
hyp10 nucleus
B
cwn-1
Pkal-1::gfp
Early L1
Late L1
CAN Left
CAN Right
cwn-1 smFISH spots
Gonad length (μm)
C
Wnt smFISH spots
Body length (μm)
D
germ line
tail
mom-2 smFISH spots
Body length (μm)
E
head
tail
sfrp-1 smFISH spots
Body length (μm)

Figure 2.2 Expression of the *C. elegans* Wnt genes during the first stage of larval development. (**A**) Expression of the five Wnt genes in early (closed lines) and late (dotted lines) L1 larvae. (**B**) The left and the right CAN neurons simultaneously induce *cwn-1* expression during L1 development. The CAN neurons are visualized using a *Pkal-1::gfp* reporter. (**C**) Quantification of total Wnt smFISH spots during L1 larval development. (**D**) Measurements of *mom-2* smFISH spots in the germline precursor cells and cells in the tail during L1 larval development. (**D**) Quantification of *sfrp-1* smFISH spots in the head and in tail neurons during L1 larval development.

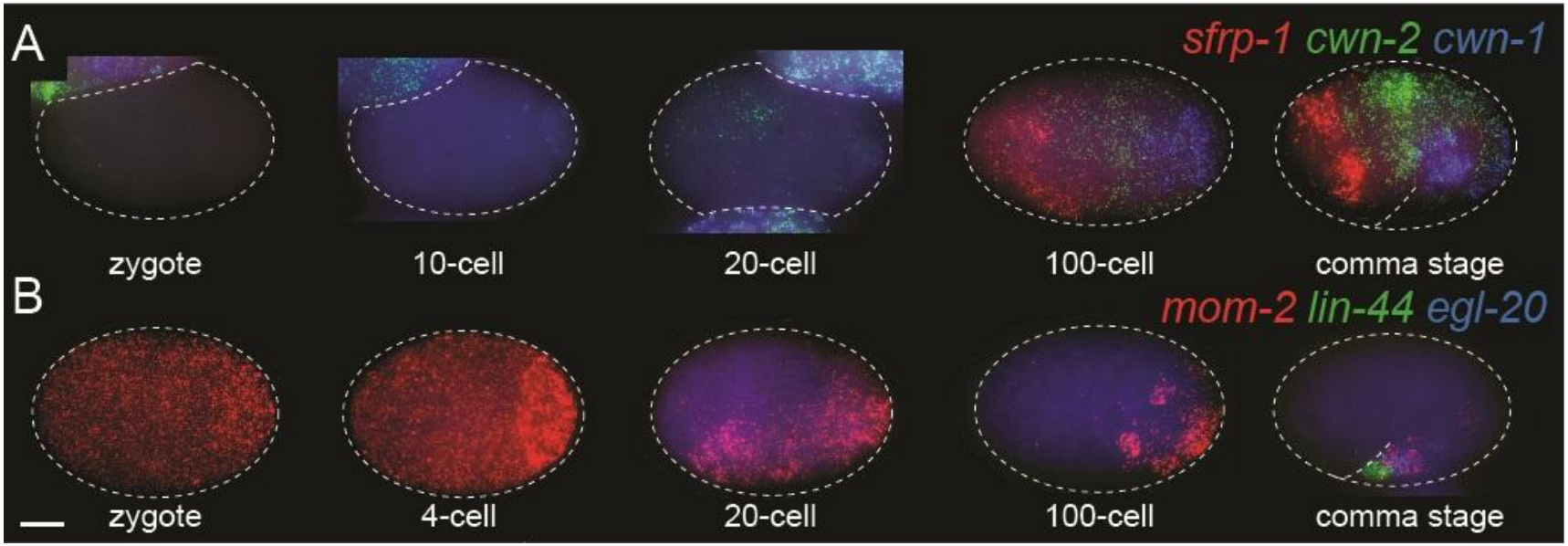
A
sfrp-1 cwn-2 cwn-1
zygote
10-cell
20-cell
100-cell
comma stage
B
mom-2 lin-44 egl-20
zygote
4-cell
20-cell
100-cell
comma stage

Figure 2.3 Single molecule mRNA FISH analyses of the *C. elegans* Wnt genes and *sfrp-1* during embryonic development. Images are maximum intensity projections of lateral z-stacks. Detection of *sfrp-1*, *cwn-1* and *cwn-2* (**A**) and *mom-2*, *lin-44* and *sfrp-1* transcripts (**B**). Embryos were staged using DIC microscopy and DAPI staining of nuclei. Scale bar is 10 µm.

We found that of the five Wnt transcripts, three (*lin-44*, *egl-20* and *cwn-1*) were mostly localized to the posterior half of L1 larvae (Fig. 2.1 A, F), in a pattern that was already present at the comma stage of embryonic development (Fig. 2.3 A, B). *lin-44* transcripts were present in the tail hypodermal cells hyp8, hyp9, hyp10 and hyp11 and at later larval stages in the phasmid socket cells PHso1 and PHso2 (Fig. 2.2 A), as previously reported [73]. In addition, we found that *lin-44* is expressed in the rectal epithelial cells B and Y, demonstrating that *lin-44* has a more anterior expression domain than has been observed using reporter transgenes. *egl-20* was expressed in the rectal epithelial cells K, F, U and B, in the anal depressor muscle and in P11/12, which is in agreement with previous reporter studies [74]. However, we found that in L1 larvae, *egl-20* was also expressed in the posterior ventral body wall muscle quadrants VL23 and VR24 and the rectal epithelial cell Y. *cwn-1* was mainly expressed in posterior body wall muscle cells (Fig. 2.1 A, B) and in the M cell descendants that give rise to body wall muscle cells and the vulva and uterine muscle cells (Fig. 2.1 F, Fig. 2.2 A). In addition, several cells were found to co-express *cwn-1* and *egl-20*, including the anal depressor muscle, the body wall muscle quadrants VL23 and VR24 and P11/12. Interestingly, we observed that the two lateral canal associated neurons (CANs) simultaneously induce *cwn-1* expression during late L1 (Fig. 2.2 A, B), an expression that persists throughout larval development.

mom-2 was previously reported to be widely expressed along the anteroposterior axis of developing larvae, with expression in body wall muscle cells, ventral cord neurons, intestinal cells and seam cells [75]. In contrast, we found that *mom-2* shows a restricted expression pattern, with *mom-2* transcripts only localizing to the germ cell precursors Z2 and Z3 and their descendants and a few unidentified cells in the tail (Fig. 2.1 D). *mom-2*

expression in the germ cells continued throughout larval development, while the tail expression reached a maximum at the mid L1 stage and disappeared before the L1 to L2 molt (Fig. 2.2 D). Also, one or two *mom-2* transcripts were occasionally detected in posterior seam cells in early L1 larvae. Consistent with the early embryonic function of *mom-2* [78], we found that *mom-2* transcripts were already present in the zygote (Fig. 2.3 B). At the 4 cell stage, *mom-2* transcripts were enriched in the P2 blastomere. During later stages of embryonic development, *mom-2* transcripts were restricted to the posterior, with expression remaining in the tail and in the region of the Z2 and Z3 germ line precursors in comma stage embryos.

The larval expression of *cwn-2* has been described using different reporter transgenes, showing either a general expression in body wall muscle cells and ventral nerve cord neurons along the whole body axis [75], or a more restricted expression in the pharynx, anterior muscle cells and the intestine [76,77]. We found that *cwn-2* transcripts mainly localized to head neurons, anterior body wall muscle cells, anterior P.n cells and the intestine (Fig. 2.1 E, F, Fig. 2.2 A). The highest *cwn-2* transcript count was observed around the terminal bulb of the pharynx, with a gradual decline in expression levels in more posterior cells. The mostly anterior expression of *cwn-2* and posterior expression of *cwn-1* was already observed at the 100 cell stage of embryonic development (Fig. 2.3 A).

Quantification of Wnt transcripts along the anteroposterior axis of staged L1 larvae revealed that the five Wnt genes are expressed in a series of partially overlapping expression domains (Fig. 2.1 F). At the posterior end of the animal, only *lin-44* is expressed. Around the rectum, the most abundantly expressed Wnt gene is *egl-20*. In the posterior region between the gonad premordium and the rectum, *cwn-1* is the dominant Wnt, while the anterior half of the animal is the domain of *cwn-2* expression. This overall anteroposterior expression profile was already present at the comma stage of embryonic development (Fig. 2.3 A, B) and remained essentially unchanged during the remainder of L1 larval development, although quantification of total Wnt transcript numbers revealed changes in the expression levels of the five Wnt genes (Fig. 2.2 A, C). Thus, whereas *mom-2* expression remained mostly unchanged during early larval

development and there was only a gradual increase in the expression of *lin-44* and *egl-20*, there was a sharp increase in the expression of *cwn-1* and *cwn-2*.

2.3 The anteriorly expressed secreted Frizzled related protein gene *sfrp-1* controls neuronal migration along the anteroposterior axis

The activity of Wnt proteins is modulated by secreted Wnt binding proteins such as members of the secreted Frizzled related proteins (SFRPs), an ancient family of Wnt regulators that are present in organism ranging from sponges to vertebrates [22] (Fig. 2.4 A). Sequence similarity searches revealed that the *C. elegans* genome contains a single SFRP ortholog encoded by the predicted gene Y73B6BL.21, which we renamed *sfrp-1*. Similar to other SFRP family members, SFRP-1 contains a cysteine rich Frizzled related domain (CRD) and a netrin-related (NTR) domain (Fig. 2.4 B), which is characterized by positively charged residues and six conserved cysteines [79].

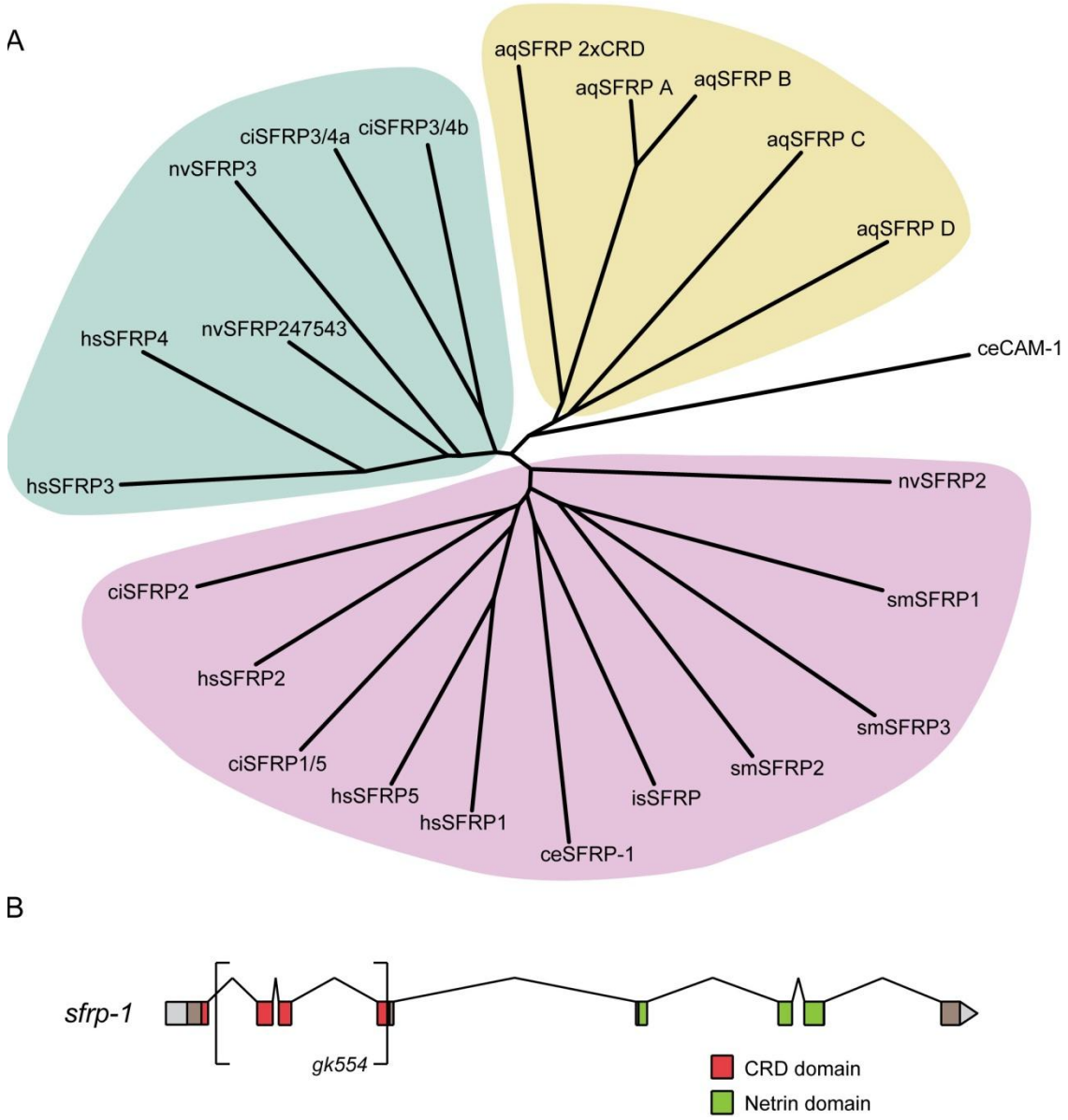

Figure 2.4 (**A**) Phylogenetic analysis of SFRPs family members of the chordates *Ciona intestinalis* (ci) and *Homo sapiens* (hs), the planarian *Schmidtea mediterranea* (sm), the nematode *Caenorhabditis elegans* (ce), the arthropod *Ixodes scapularis* (is), the cnidarian *Nematostella vectensis* (nv) and the sponge *Amphimedon queenslandica* (aq). SFRPs cluster in two clades [80]: the SFRP1/2/5 cluster (pink), which includes *C. elegans sfrp-1*, and the SFRP3/4 cluster (green). The *A. queenslandica* SFRPs cluster separately, suggesting that the species diverged before the SFRP duplication. *C. elegans* CAM-1/ROR contains a CRD domain that is related to the CRD domain of

SFRPs. The phylogenetic tree was constructed with clustalw (using default parameter settings) (**B**) Schematic representation of the *C. elegans sfrp-1* (Y73B6BL.21) gene structure and protein domains. The *sfrp-1* deletion *gk554* is a 1261 base pair deletion which truncates the *sfrp-1* gene upstream of the CRD and NTR domains.

To determine the expression pattern of *sfrp-1*, we analyzed *sfrp-1* mRNA localization using smFISH. As shown in Fig. 2.1 E, *sfrp-1* is expressed in four stripes of cells in the head region, an anterior specific expression that is already present at the 100 cell stage of embryonic development (Fig. 2.3 A). Using a muscle specific marker, these cells were identified as head body wall muscle cells. In addition, we found that *sfrp-1* is expressed at low levels in a single posterior ventral nerve cord neuron and occasionally in one or more cells around the rectum (Fig. 2.1 E and Fig. 2.2 E). The predominantly anterior expression of *sfrp-1* indicates that SFRP-1 and the posteriorly expressed Wnts form opposing gradients. Although we have not been able to directly visualize such an SFRP-1 concentration gradient, the genetic analysis of *sfrp-1* function described below demonstrates that SFRP-1 has both short and long-range functions in modulating Wnt activity.

To investigate the function of *sfrp-1*, we used the deletion allele *gk554*, which truncates the *sfrp-1* gene upstream of the CRD and NTR domains and likely represents the null phenotype (Fig. 2.4 B). *sfrp-1(gk554)* is viable and does not induce obvious morphological defects. However, *sfrp-1* mutants show clear alterations in the Wnt dependent anteroposterior positioning of migrating neuroblasts.

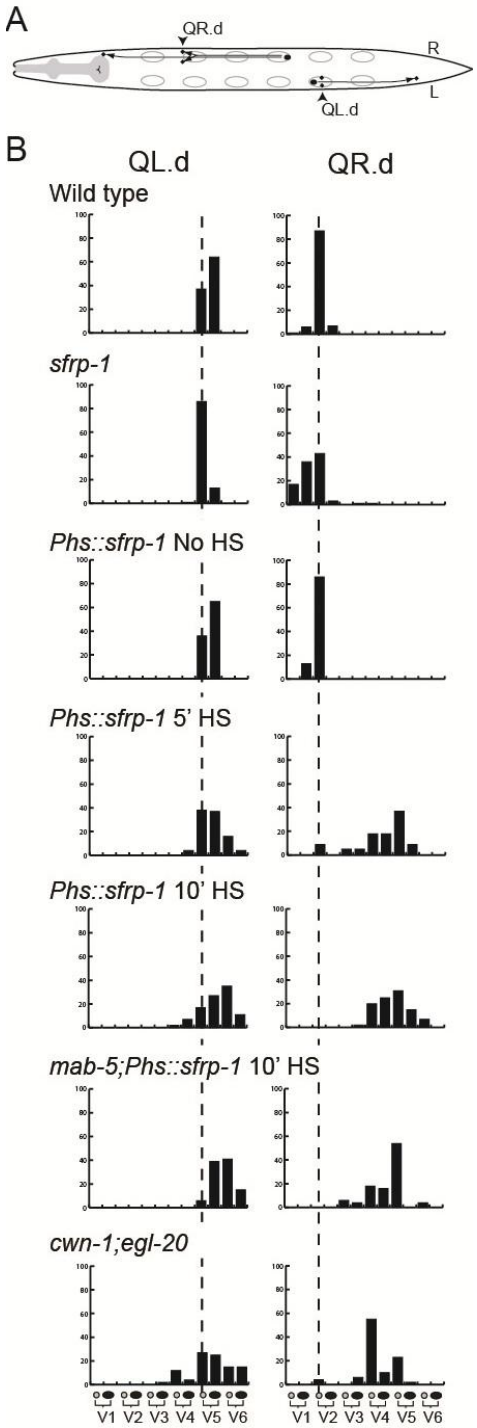

Figure 2.5 *sfrp-1* is required for the migration of the QR descendants. (**A**) Schematic representation of Q neuroblast descendant migration. Arrowheads indicate the final positions of the Q.paa and Q.pap cells. (**B**) The final positions of the left and right Q.paa and Q.pap cells are indicated relative to the invariant positions of the seam cells V1 to

V6 (n>100 for wild type and *sfrp-1*; for the other conditions, n>50). The dashed line indicates the wild type position.

One group of neuroblasts that migrates along the anteroposterior axis are the Q neuroblast descendants [67,70]. At the end of embryogenesis, two Q neuroblasts are generated at equivalent positions on the left (QL) and right (QR) lateral side of the animal (Fig. 2.5 A). During the first stage of larval development, the two Q neuroblasts each generate three descendants that migrate in opposite directions: on the left side, the QL descendants (QL.d) migrate towards the posterior, whereas on the right side, the QR.d migrate towards the anterior. Both anterior and posterior migration is controlled by Wnt signaling. The posterior migration of the QL.d is mediated by EGL-20, which triggers a canonical Wnt/β-catenin pathway to induce expression of the target gene *mab-5* and to direct migration towards the posterior [71,74,81]. The anterior migration of the QR.d is also dependent on EGL-20, but here EGL-20 functions together with CWN-1 to activate a β-catenin independent Wnt signaling pathway that is required for anterior directed migration [72]. Although the mechanism remains to be established, current models suggest that a difference in response threshold to EGL-20 determines which pathway is activated [74]. Thus, QL is primed to activate canonical Wnt/β-catenin signaling in response to EGL-20, whereas QR will only activate this pathway when EGL-20 is overexpressed. At intermediate levels, overexpression of EGL-20 induces overmigration of the QR.d, indicating that Wnt signaling activity not only specifies the direction of migration, but also influences the position at which the cells terminate their migration [74]. To investigate whether *sfrp-1* regulates the Wnt dependent migration of the Q descendants, we determined the final positions of the Q descendants Q.paa and Q.pap relative to the hypodermal seam cells V1 to V6. We found that the QL.d localized around their normal positions in *sfrp-1* mutants (Fig. 2.5 B). There was, however, a clear change in the final position of the QR.d, with the QR.d migrating significantly further into the anterior than in wild type animals ($p<0.001$, Fisher's exact test). As this phenotype is similar to the extended migration induced by EGL-20 overexpression, these data are consistent with a negative regulatory role for *sfrp-1* in QR.d migration. Loss of this

negative regulatory activity is however insufficient to trigger canonical Wnt/β-catenin signaling and *mab-5* expression in QR.

In addition to the defect in the anterior migration of the QR.d, we found that *sfrp-1* mutants show misplacement of the ALM and CAN neurons (Fig. 2.10 A, Fig. 2.11 A). Both neurons migrate during the end of embryogenesis from the anterior to final positions in the mid-body region [66,67]. In both cases, posterior migration depends on the combined activity of CWN-1 and CWN-2 [72]. In *sfrp-1* mutants, the posterior migration of the ALM neurons was significantly truncated ($p<0.001$) (Fig. 2.10 B). Also in case of the CAN neurons, mutation of *sfrp-1* induced undermigration ($p<0.001$), although this effect was less pronounced as observed with the ALM neurons (Fig. 2.11 B).

Mutation of *sfrp-1* did not significantly affect other Wnt dependent processes (Table 2.1 and data not shown). Thus, there were no defects in the anterior migration of the HSN neurons [68], the polarization of the mechanosensory neurons ALM and PLM [82], the polarization of the division of the hypodermal seam cells V5 and T [73,83], the positioning of the nerve ring [76], or the specification of P12 fate [84]. With the exception of nerve ring positioning, all of these processes control cells in the posterior or mid-body region, whereas the migration of the QR.d, ALM and CAN neurons takes place in the anterior. These results are therefore consistent with the anterior specific expression of *sfrp-1* and a function of SFRP-1 in modulating Wnt activity in the anterior body region.

Table 2.1 Wnt phenotypes in *sfrp-1* and hypomorphic Wnt secretion mutants.

	Wild type	*sfrp-1*	*vps-35*	*vps-35; sfrp-1*	*mig-14(mu71)*	*mig-14(mu71); sfrp-1*
ALM polarity	0	1	21	16	0	N.D.
PLM polarity	0	0	29	31	15	N.D.
P12 to P11	0	0	6	6	4	2
T cell polarity	1	0	12	0	11	4
V5 polarity	0	0	32	2	0	0
Nerve ring placement	1	0	4	1	0	1

Numbers indicate percentage defective (n>100). The polarity of the ALM and PLM mechanosensory neurons was scored using *a mec-7::gfp (muIs32 or muIs35)* expressing transgene [85]. The polarity of the V5 division and P12 to P11 fate transformation were scored using Nomarski microscopy at the appropriate developmental stage. Effects on T cell polarity were determined by DiO staining of the T derived phasmid structure in young adults [86]. Nerve ring placement was determined by DiO staining of the amphid neurons.

2.4 SFRP-1 is a global inhibitor of Wnt signaling

One of the main functions of SFRPs is to negatively regulate Wnt signaling [87]. There are, however, also examples of SFRPs functioning as facilitators or direct mediators of Wnt signaling, for example by assisting the spreading of Wnt in the tissue or by directly interacting with the Wnt receptor Frizzled [88,89]. To investigate potential Wnt inhibitory or stimulatory functions of *sfrp-1*, we overexpressed *sfrp-1* using a heat-shock inducible

promoter (Fig. 2.5 B). A short induction of *sfrp-1* expression before the Wnt dependent migration of the Q descendants resulted in an almost complete loss of the anterior migration of the QR.d, a phenotype that is also observed in double mutants of *egl-20* and *cwn-1* or mutants in which all five Wnt genes have been deleted [72]. Also the effect of *sfrp-1* overexpression on the QL.d was similar to *egl-20; cwn-1* double mutants, with a more variable and posterior localization of the cells (Fig. 2.5 B). Taken together, these results show that the migration phenotype induced by overexpression of *sfrp-1* closely resembles that of mutants defective in multiple Wnts, consistent with a negative regulatory role for SFRP-1 in the Wnt dependent control of Q.d migration. This conclusion is further supported by the observation that overexpression of *sfrp-1* induces a similar loss of anterior QR.d and QL.d migration in a *mab-5* null mutant background (Fig. 2.5 B), demonstrating that the posterior localization of the QR.d and QL.d does not result from activation of the EGL-20 target gene *mab-5*. We found that *sfrp-1* overexpression also inhibited the EGL-20 dependent anterior migration of the HSN neurons as well as other Wnt dependent processes, such as the polarized division of the seam cell V5 (data not shown), indicating that SFRP-1 can inhibit the activity of most if not all of the Wnt proteins of *C. elegans*. Importantly, no phenotypes were observed that suggest a stimulatory function of SFRP-1 in Wnt signaling.

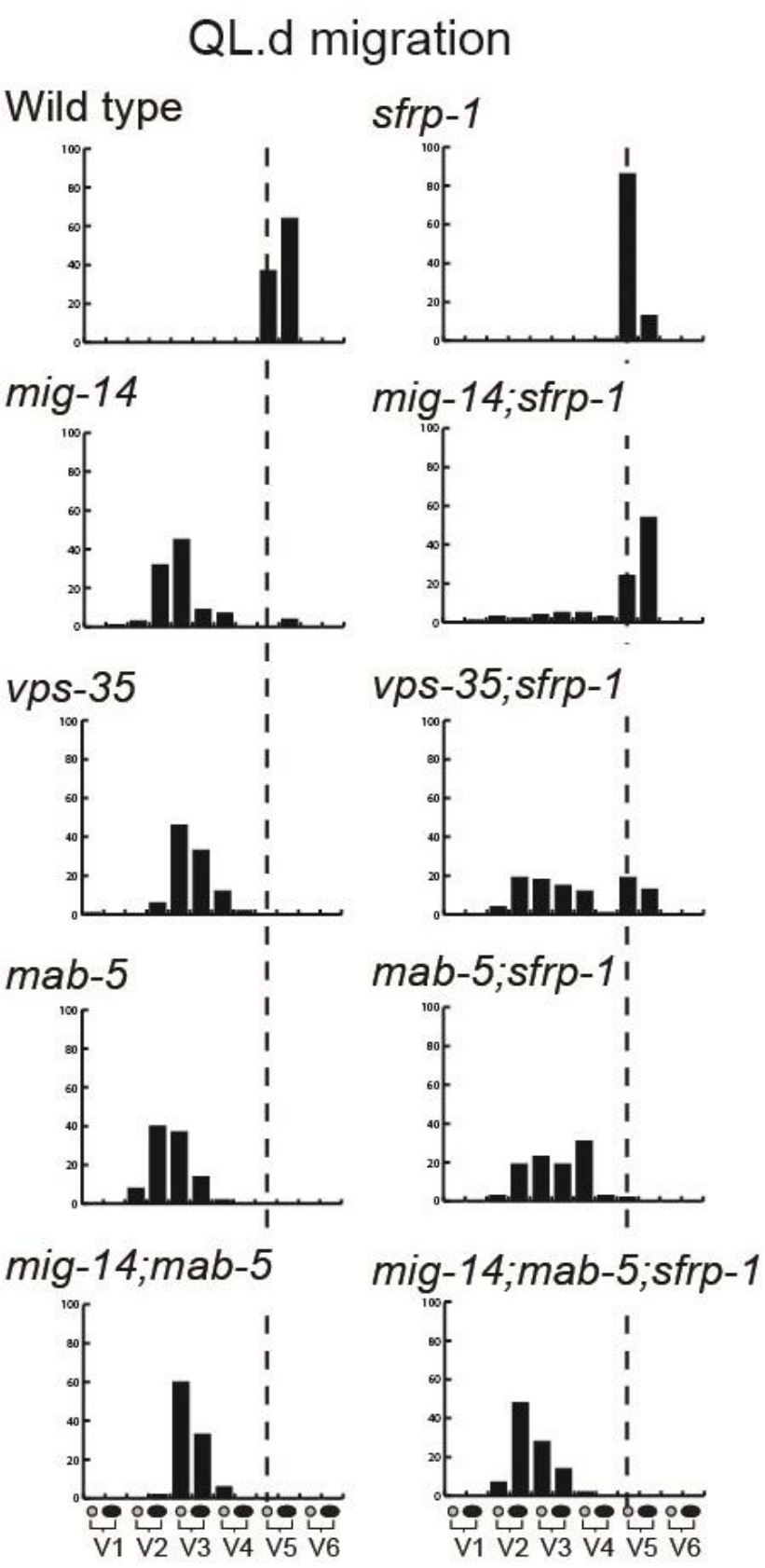
QL.d migration
Wild type
sfrp-1
mig-14
mig-14;sfrp-1
vps-35
vps-35;sfrp-1
mab-5
mab-5;sfrp-1
mig-14;mab-5
mig-14;mab-5;sfrp-1
V1 V2 V3 V4 V5 V6
V1 V2 V3 V4 V5 V6

Figure 2.6 *sfrp-1* rescues QL.d migration in hypomorphic Wnt secretion mutants. The final positions of QL.paa and QL.pap cells are indicated relative to the seam cells V1 to V6 (n>50). The dashed line indicates the wild type position.

To further investigate the function of *sfrp-1* in modulating Wnt activity, we analyzed double mutants between *sfrp-1* and mutants in which Wnt secretion is reduced: a hypomorphic allele (*mu71*) of the Wnt sorting receptor *mig-14*/Wls [90,91] and a null allele of the retromer subunit gene *vps-35* [16]. By assaying whether specific Wnt phenotypes are suppressed or enhanced, these mutants provide a sensitive assay to test negative or positive effects of *sfrp-1* on Wnt signaling. In *mig-14(mu71)* and *vps-35* single mutants, a reduction in EGL-20 levels leads to a loss of *mab-5* expression in QL [71] and anterior migration of the QL.d (Fig. 2.6). We found that in double mutants with *sfrp-1*, posterior migration was almost fully restored in *mig-14(mu71)* and significantly rescued in *vps-35*. Importantly, the rescue of posterior migration depended on activation of *mab-5* expression. Thus, mutation of *sfrp-1* failed to restore posterior QL.d localization in a *mig-14(mu71); mab-5* double mutant background (Fig. 2.6). Furthermore, *mab-5* expression was markedly increased in the QL.d of *mig-14(mu71); sfrp-1* double mutants (20% of *mig-14(mu71)* versus 75% of *mig-14(mu71); sfrp-1* animals showed activation of a *mab-5::lacZ* reporter, whereas the reporter was expressed in 86% and 83% of wild type and *sfrp-1* single mutants, respectively. In each case, n>50). These results suggest that the reduction in EGL-20 signaling can be overcome by removal of SFRP-1, consistent with a negative regulatory role of SFRP-1 in the EGL-20 dependent activation of canonical Wnt/β-catenin signaling in QL. We observed a similar inhibitory role for *sfrp-1* in QR.d migration. Thus, whereas the QR.d showed reduced anterior migration in *mig-14(mu71)* and *vps-35* mutants, the QR.d localized at their correct positions in double mutants with *sfrp-1* (Fig. 2.7). A comprehensive analysis of other Wnt phenotypes in *mig-14(mu71)* and *vps-35* mutants showed that loss of *sfrp-1* also suppressed defects in the migration of the ALM neurons and the polarity of the seam cells V5 and T (Fig. 6.6.2 B and Table 2.1). Importantly, there were no instances in which the *vps-35* or *mig-14(mu71)* phenotype was enhanced

by loss of *sfrp-1*. Taken together with the strong Wnt inhibitory activity of *sfrp-1* overexpression, these results support the conclusion that SFRP-1 functions as a global inhibitor of Wnt signaling in *C. elegans*.

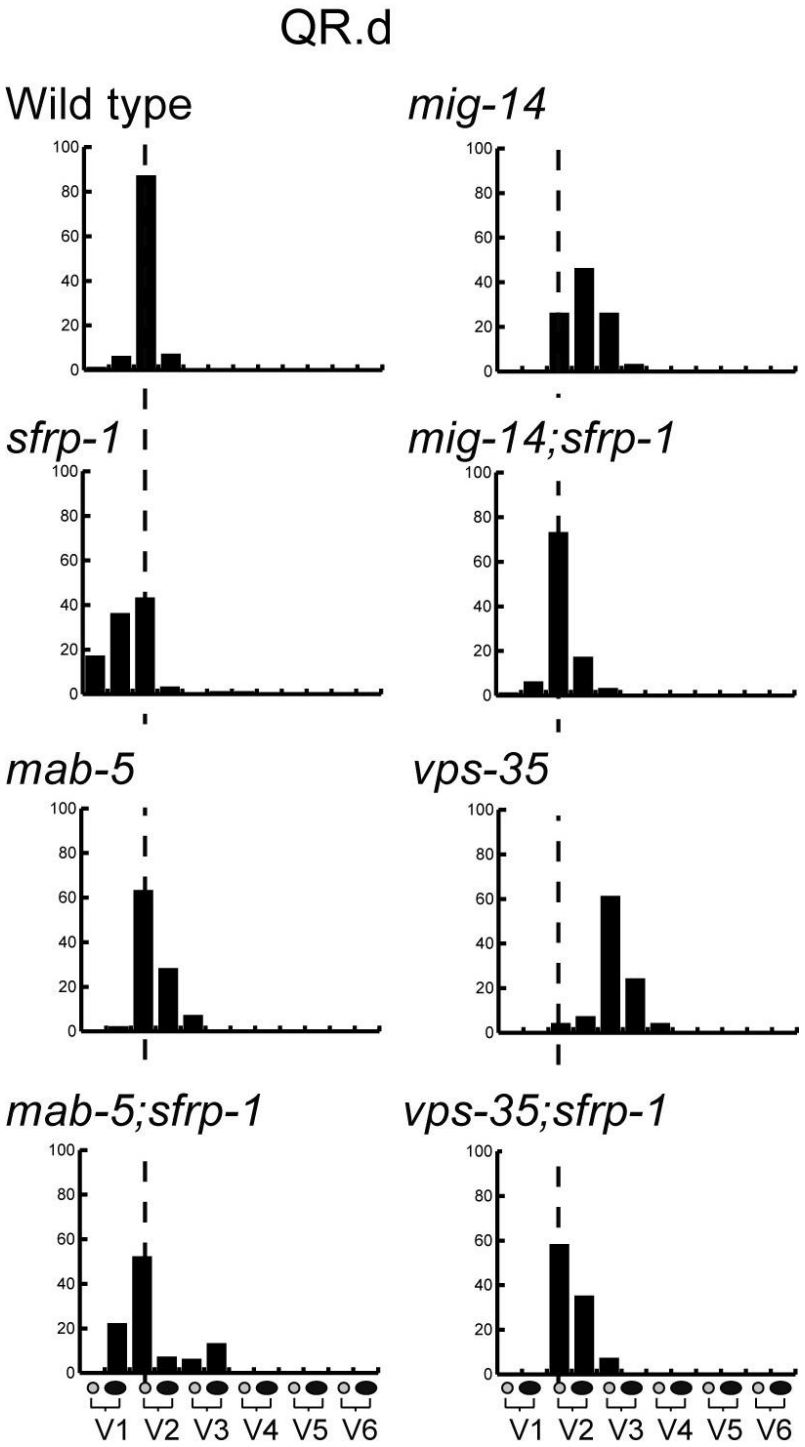

Figure 2.7 *sfrp-1* suppresses the QR.d undermigration induced by hypomorphic Wnt secretion mutants. The final positions of QR.paa and QR.pap cells are indicated relative to the seam cells V1 to V6 (n>50). The dashed line indicates the wild type position.

2.5 The *sfrp-1* induced overmigration of the QR descendants is suppressed by mutation of *cwn-2*

The overmigration of the QR.d in *sfrp-1* mutants is similar to the extended migration induced by ubiquitous EGL-20 expression [74], indicating that the overmigration is a result of a gain in Wnt signaling activity. To investigate which Wnts mediate the *sfrp-1* induced overmigration, we constructed double mutants between *sfrp-1* and null mutants of the different Wnt genes. We found that mutation of *lin-44* or *mom-2* did not suppress the *sfrp-1* induced overmigration (Fig. 2.8). In double mutants between *sfrp-1* and *egl-20*, there was a partial suppression of the overmigration, but also a clear undermigration of the QR.d, an effect that was even more pronounced in double mutants with *cwn-1*. EGL-20 and CWN-1 function partially redundantly in specifying anterior QR.d migration and loss of either *egl-20* or *cwn-1* results in a distinct undermigration of the QR.d [72]. The intermediate phenotype of the *egl-20; sfrp-1* and *cwn-1; sfrp-1* double mutants therefore suggests that *egl-20* and *cwn-1* either function in parallel to *sfrp-1* or only play a minor role in the *sfrp-1* induced overmigration of the QR.d. In contrast, we found that the *sfrp-1* induced overmigration was fully rescued by a null mutation in *cwn-2* (Fig. 2.8). Thus, whereas *cwn-2* has no significant effect on QR.d positioning on its own, the QR.d localized at their wild type position in *sfrp-1; cwn-2* double mutants. Taken together, these results indicate that derepression of CWN-2 signaling is primarily responsible for the QR.d overmigration phenotype of *sfrp-1* mutants.

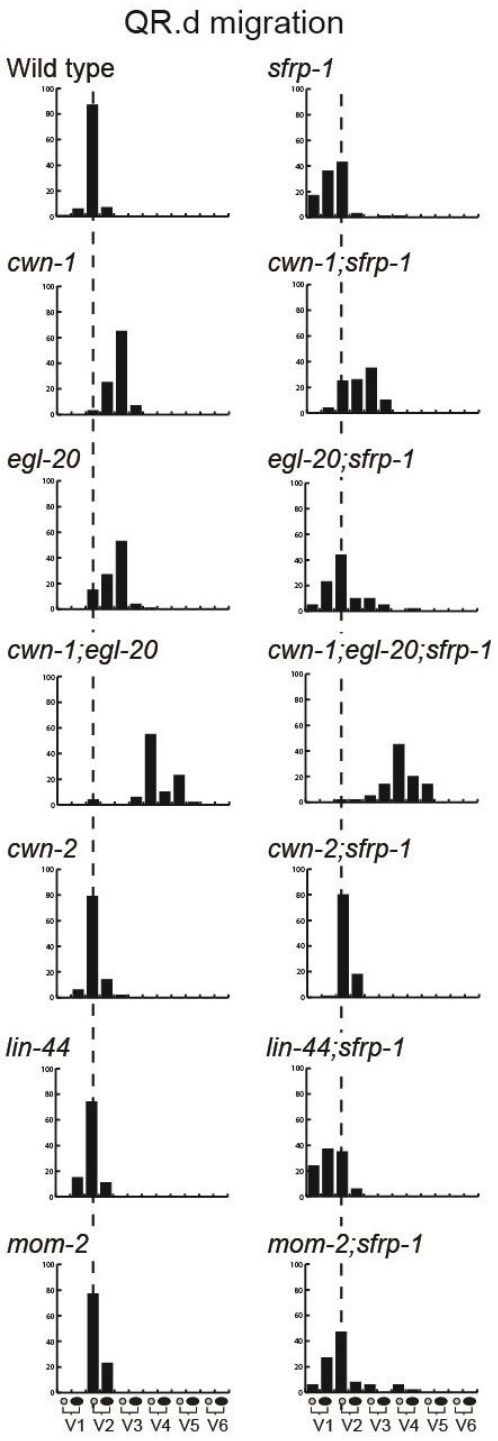

Figure 2.8 The *sfrp-1* induced overmigration of the QR.d is suppressed by mutation of *cwn-2*. The final positions of QR.paa and QR.pap cells are indicated relative to the seam cells V1 to V6 (n>50). The dashed line indicates the wild type position.

2.6 The *sfrp-1* induced undermigration of the ALM and CAN neurons is suppressed by mutation of *cwn-1* or *cwn-2*

The posterior migration of the ALM neurons is dependent on the redundant activity of CWN-1 and CWN-2, with a strong inhibition of migration in *cwn-1; cwn-2* double mutants [72]. A similar undermigration is observed in *sfrp-1* mutants, indicating that Wnt overactivity also interferes with the correct posterior migration of the ALM neurons. This conclusion is supported by the observation that the ALM undermigration phenotype of *sfrp-1* is suppressed by reducing Wnt secretion through mutation of the Wnt sorting receptor *mig-14*/Wls (Fig. 2.9 B). To investigate which Wnts are required for the *sfrp-1* induced undermigration of the ALM neurons, we analyzed double mutants with null alleles of each of the five different Wnt genes and tested which combination could suppress the ALM undermigration phenotype. Whereas *lin-44*, *egl-20* and *mom-2* did not affect the *sfrp-1* induced ALM undermigration, mutation of *cwn-1* or *cwn-2* fully restored the migration of the ALM neurons to their wild type positions (Fig. 2.9 B and Fig. 2.10 B). These results suggest that in the absence of SFRP-1, overactivity of CWN-1 and CWN-2 interferes with the correct positioning of the ALM neurons, and that normal migration can be restored by removing either of the two Wnt genes. Furthermore, the *sfrp-1* induced undermigration of the ALM neurons was fully suppressed in double mutants between *sfrp-1* and the Frizzled *mom-5* (Fig. 2.9 B), indicating that CWN-1 and CWN-2 control ALM positioning through the MOM-5/Frizzled receptor.

Similar results were obtained for the *sfrp-1* induced undermigration of the CAN neurons, which was also dependent on CWN-1 and CWN-2. Thus, CAN undermigration was not suppressed in *lin-44*, *egl-20* or *mom-2* mutants, but was rescued in either *cwn-1* or *cwn-2* mutants (Fig. 2.11 B).

The function of SFRP-1 in suppressing CWN-1 and CWN-2 activity is consistent with the anterior expression of *sfrp-1* and is in agreement with a role for SFRP-1 in modulating Wnt activity in the anterior body region. Our results show that this inhibitory activity is particularly important for controlling the Wnt dependent migration of neuroblasts along the primary body axis of *C. elegans*.

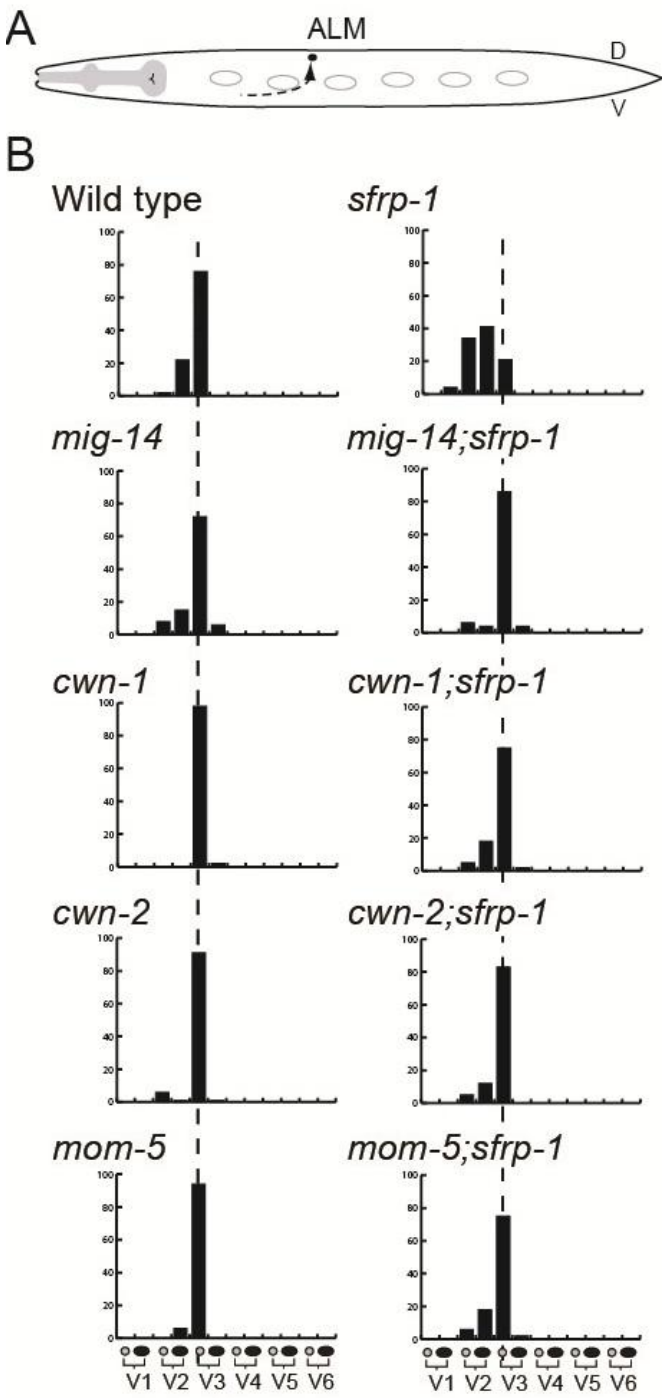

Figure 2.9 The *sfrp-1* induced undermigration of the ALM neurons is suppressed by mutation of *cwn-1* or *cwn-2*. (**A**) Schematic representation of the ALM migration. Note that the migration takes place at the end of embryogenesis. (**B**) The final positions of the ALML and ALMR neurons are indicated relative to the seam cells V1 to V6 (n>50). The dashed line indicates the wild type position.

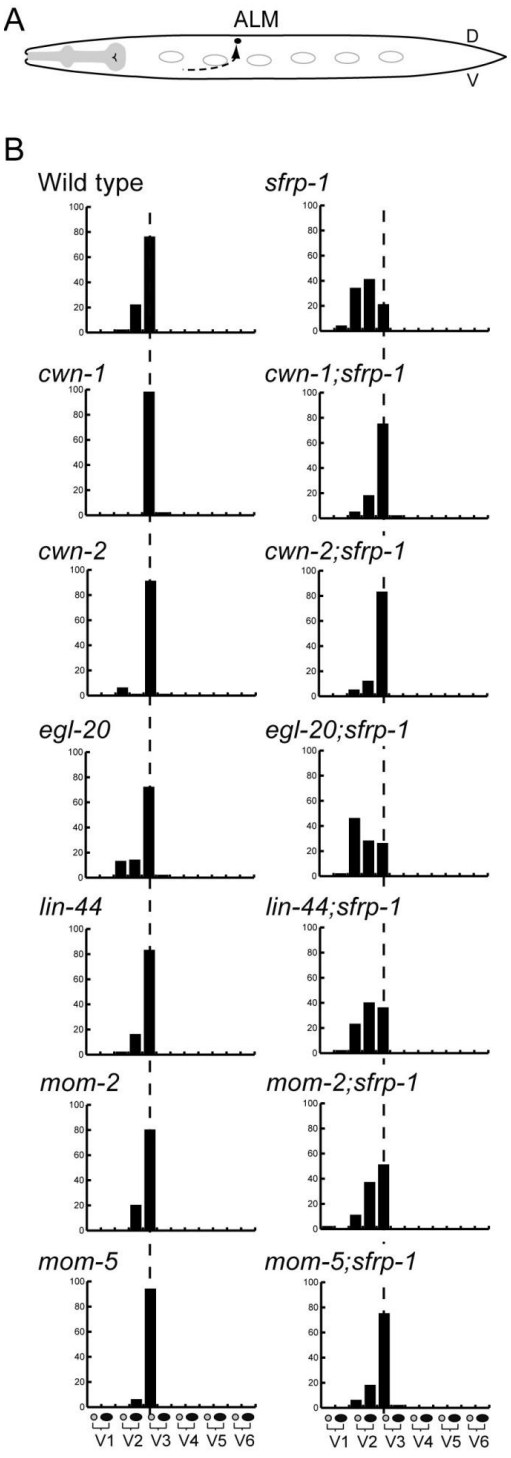

Figure 2.10 The *sfrp-1* induced undermigration of the ALM neurons is not suppressed by mutation of *lin-44*, *egl-20* or *mom-2*. (**A**) Schematic representation of ALM migration. (**B**) The final positions of the ALML and ALMR neurons are indicated relative to the seam cells V1 to V6 (n>50). The dashed line indicates the wild type position.

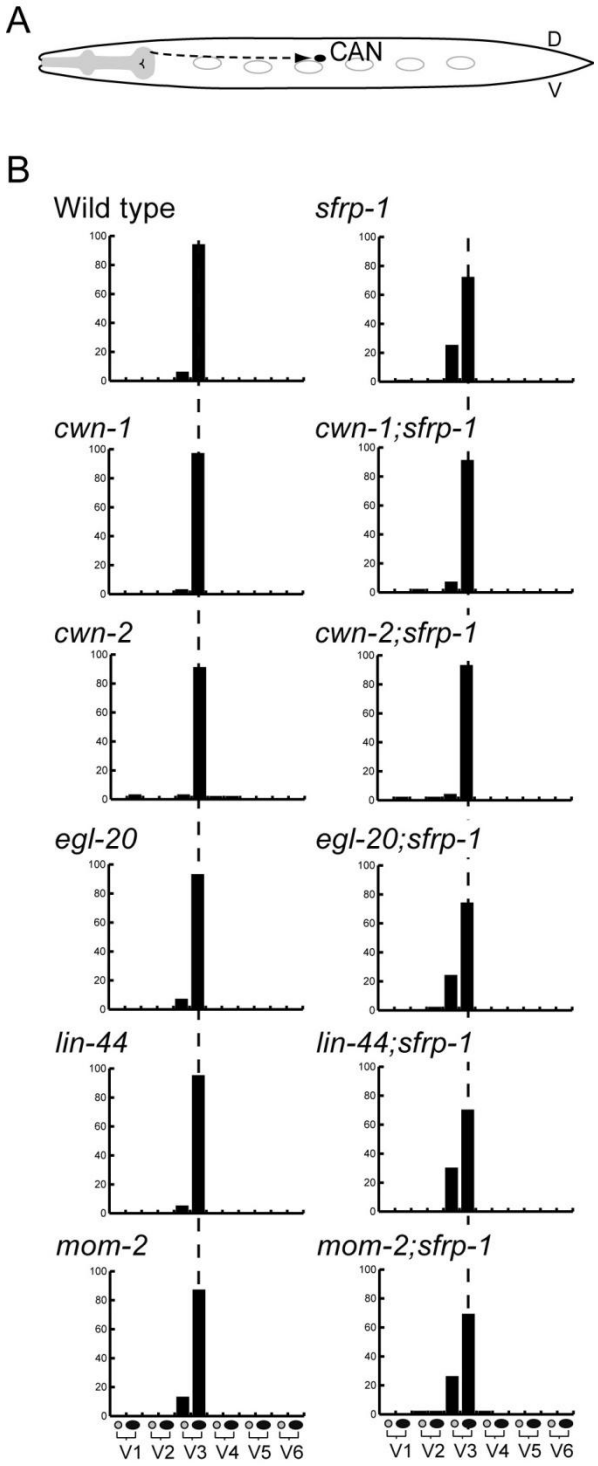

Figure 2.11 The *sfrp-1* induced undermigration of the CAN neurons is suppressed by mutation of *cwn-1* or *cwn-2*. (**A**) Schematic representation of the CAN neuron migration. (**B**) The final positions of the CANL and CANR neurons are indicated relative to the seam cells V1 to V6 (n>50). The dashed line indicates the wild type position.

2.7 Discussion

During *C. elegans* development, the migration of neuroblasts along the anteroposterior axis is controlled through a complex network of partially redundantly acting Wnt proteins. Here, we used smFISH to quantitatively map the spatio-temporal expression pattern of the *C. elegans* Wnt genes. We show that the five Wnt genes are expressed in partially overlapping expression domains along the anteroposterior axis, with the most prominent Wnt expression in the posterior body region. Furthermore, we demonstrate that Wnt signaling in the anterior body region is repressed by the secreted Frizzled related protein SFRP-1. These results show that the anteroposterior positioning of neuroblasts is controlled by opposing Wnt and Wnt inhibitory activities and provide further evidence for the evolutionary conservation of this system in patterning of the primary body axis.

A quantitative gene expression map of the *C. elegans* Wnt family

Conventional methods for gene expression analysis in *C. elegans* are mostly based on transgenic reporter constructs [92]. In this study we used for the first time smFISH [23] to determine the spatio-temporal expression pattern of a gene family in *C. elegans*. By visualizing single transcripts as bright diffraction-limited spots, we could directly measure endogenous gene expression *in vivo* by counting the number of spots in a three dimensional area of interest, such as a specific cell or tissue. Importantly, this method also allowed us to quantify dynamic changes in gene expression, such as the transient expression of *mom-2* in cells of the tail and the activation of *cwn-1* expression in the CAN neurons during the first stage of larval development. We found that the expression level and spatial distribution of transcripts detected by smFISH was highly reproducible between staged animals, indicating that this methods accurately visualizes endogenous gene expression patterns. We conclude that smFISH can be used to produce quantitative spatio-temporal maps of endogenous gene expression patterns. It should be noted, however, that the expression pattern of the protein product may be influenced by post-transcriptional regulation.

Our smFISH analysis of the Wnt gene family showed similarities, but also important differences with expression patterns based on transgenic reporter constructs. We found that *cwn-2* is mainly expressed in head neurons and anterior body wall muscle cells, resolving a conflict in the previously reported expression patterns for *cwn-2* [75–77]. Furthermore, we observed that *mom-2* is not generally expressed along the anteroposterior body axis [75], but is restricted to the germ line precursor cells and transiently to a group of cells in the tail. Another important difference is the expression of *lin-44* outside of the tail hypodermal cells [73]. The more anterior expression of *lin-44* in the B and Y rectal epithelial cells is particularly interesting for the function of LIN-44 as a directional signal in T cell polarity [93] and for the inhibition of presynaptic assemblies in the DA9 neuron [94].

The smFISH analysis revealed that the five Wnt genes are expressed in a series of partially overlapping expression domains, with expression of three of the five Wnt genes in the posterior and one in the anterior half of the body. The expression of the different Wnt genes in serial domains correlates with their function in controlling the migration of neuroblasts along the anteroposterior axis. Thus, the posteriorly expressed Wnt EGL-20 controls migration in the posterior and mid-body region, while CWN-1 and CWN-2 are particularly important for the migration of the QR descendants and the CAN and ALM neurons in the anterior half of the animal [68,71,72]. We propose that the staggered series of Wnt expression domains provides a system for positional information along the anteroposterior body axis of *C. elegans*.

The secreted Frizzled related protein SFRP-1 is an inhibitor of Wnt signaling

SFRP proteins are characterized by an amino-terminal cysteine-rich domain (CRD) that is similar to the Wnt binding CRD domain of Frizzled [22]. SFRPs are secreted proteins that have been shown to act as inhibitors of Wnt signaling, most likely by competing with Wnt receptors for Wnt binding. However, SFRPs have also been reported to promote Wnt signaling, for example by facilitating the spreading of Wnt in the tissue [89] or by directly interacting with Frizzleds to stimulate signaling in a Wnt independent

manner [88]. Phylogenetic analysis has shown that the SFRP family appeared very early in metazoan evolution, as clear SFRP orthologs are already present in the cnidarians *Hydra* and *Nematostella vectensis* [95]. Their function has, however, not been studied in any of the genetically tractable invertebrate model systems. The *Drosophila* genome does not contain SFRP orthologs, indicating that this gene family may have been lost in insects (but not in all arthropods, as the genome of the tick *Ixodes scapularis* contains an SFRP ortholog). In this study, we show that the *C. elegans* genome contains a single SFRP ortholog, *sfrp-1*, which enabled us to study potential Wnt inhibitory or stimulatory functions of SFRPs in a well defined model system. We found that SFRP-1 functions exclusively as an inhibitor of Wnt signaling: First, overexpression of *sfrp-1* induced a strong defect in Wnt signaling, similar to the phenotype observed in mutants in which all five Wnt genes have been mutated [72]. Second, loss of *sfrp-1* suppressed the Wnt signaling defect of mutants that induce a reduction in Wnt secretion and finally, all the phenotypes observed in *sfrp-1* mutants could be suppressed by removing specific Wnts, indicating that mutation of *sfrp-1* leads to derepression of Wnt signaling. These results suggest that the stimulatory function of SFRPs in Wnt signaling has either been lost in the nematode lineage, or is a more recent invention of organisms of higher complexity. Studies on the cnidarian SFRPs may shed light on this question.

An anterior SFRP-1 inhibitory gradient controls the positioning of neuroblasts in the anterior body region

The predominant anterior expression of *sfrp-1* suggests that it counteracts the more posteriorly expressed Wnts. Loss of this inhibitory activity leads to defects in the migration of neuroblasts in the anterior body region. Thus, the QR.d migrate too far into the anterior, whereas the extent of the posterior migration of the CAN and ALM neurons is reduced. In each of these cases, the final position of the cells is shifted anteriorly, indicating that SFRP-1 counteracts a Wnt activity that promotes anterior localization. We found that the *sfrp-1* induced anterior displacement of the QR.d could be suppressed by mutation of *cwn-2*, whereas ALM and CAN migration could be restored

by deletion of either *cwn-2* or *cwn-1*. These results are consistent with a local inhibitory function of SFRP-1 in controlling the activity of the two most anteriorly expressed Wnts.

In addition to this short range function in the anterior body region, our experiments in Wnt secretion mutants showed that SFRP-1 also has a long-range inhibitory activity. Thus, mutation of *sfrp-1* rescued the posterior migration of the QL.d and the polarity of the V5 and T cell divisions in hypomorphic Wnt secretion mutants, consistent with a function of SFRP-1 in modulating Wnt activity in the mid to posterior body region. This long-range inhibition may fine tune the activity gradients of the posteriorly expressed Wnt genes.

An evolutionarily conserved function of Wnts and Wnt inhibitors in patterning the primary body axis

We found that four of the five *C. elegans* Wnt genes are expressed in a series of partially overlapping domains along the anteroposterior axis. This staggered expression is remarkably similar to the expression of Wnt genes in the cnidarian *Nematostella vectensis* [59] and in the planarian *Schmidtea mediterranea* [62]. It has been proposed that the staggered expression of Wnt genes provides an ancestral mechanism for positional information along the primary body axis [95] and our results suggest that *C. elegans* has retained such a system.

Another important similarity is the anterior specific expression of *sfrp-1* and the mostly posterior expression of the Wnt genes. This opposite expression of Wnts and Wnt inhibitors is already present in cnidarians, where Wnt inhibitors are expressed at the aboral side and Wnts at the oral side of the primary body axis [58,59,61,95]. Posterior Wnt signaling and anterior Wnt inhibition is also a central feature of vertebrate neurectodermal patterning, with the formation of the eyes and anterior brain structures depending on the anterior activity of both intracellular and secreted Wnt inhibitory factors [54–56]. In protostomes, anterior specific expression of an SFRP has been observed in *Schmidtea mediterranea* [62], but Wnt inhibitors have not been studied in any of the other protostome model organisms. Our studies in *C. elegans* show that the

opposite expression of Wnts and Wnt inhibitors is also an important feature of nematode development, supporting the notion that a system of posterior Wnt activity and anterior Wnt inhibition is a unifying principle of primary body axis specification in animals [63].

Chapter 3. Resource: Expression dynamics of *C. elegans* Wnt pathway genes at single molecule resolution

This chapter describes additional mRNA expression data for Wnt pathway genes during *C. elegans* post-embryonic development we obtained that were not included in Chapter 2. While previous expression studies in *C. elegans* using transgenes were often misleading due to its lack of key regulatory elements and/or silencing in the germline, we have avoided such problems by using a novel single molecule resolution *in situ* hybridization technique [23]. As a result, we found a number of novel Wnt expression dynamics in the developing germ line and vulva. We hope this chapter to become a useful resource to the *C. elegans* Wnt community.

Wnt signaling pathway controls myriads of developmental events including cell proliferation, migration, polarity, and differentiation during all developmental stages of *C. elegans*. In chapter 2, we have demonstrated that migrations of certain neuronal cells are controlled by multiple Wnt ligands that are secreted and diffused from a limited number of spatially localized cells to form morphogenetic fields along the body. Given the multiple types of Wnt ligand (*egl-20*, *cwn-1*, *cwn-2*, *lin-44* and *mom-2*) and receptors (*lin-17/Fz*, *lin-18/Ryk*, *mom-5/Fz*, *mig-1/Fz* and *cfz-2/Fz*), each developing cell within this field can potentially respond selectively to one or more of such extracellular Wnt ligand fields by expressing the corresponding membrane bound Wnt receptors. Whether a receptor can interact with one or multiple ligands at the molecular level is currently not well understood. The overall strength of such response will be a function of numerous factors, but mostly dominated by the expression levels of extracellular ligands and membrane bound receptors, in either dosage or gradient dependent manner. For instance, as discussed in chapter 2, *mab-5* Hox gene in bilateral pair of neuroblasts, Q.L and Q.R in hatchlings, is expressed at distinct levels because the two cells have different EGL-20 dosage response thresholds resulting in migration of these cells in opposite directions [74]. On the other hand, cells can establish proper polarity by

sensing extracellular Wnt protein gradient. During early larval period, the posterior gradient of LIN-44 from the tail tip provides a directional cue to the two lateral T cells in the tail to control asymmetric intracellular localization of LIN-17 Wnt receptors. This results in asymmetric T cell division: an anterior hypodermal daughter cell and a posterior neuronal daughter cell [73]. This polarity is reversed when LIN-44 is ectopically expressed by an anteriorly expressed promoter [93]. A similar mechanism was recently studied in the developing vulva during late larval stages, where MOM-2 and LIN-44 Wnt gradients generated from the anchor cell (AC) and presumably CWN-2 from nearby sources act as instructive sources of AP orientation of the vulval precursor cells (VPCs), P5pa to P.7pp, during vulval development through receptors LIN-17 and LIN-18 [96] (Fig. 3.1).

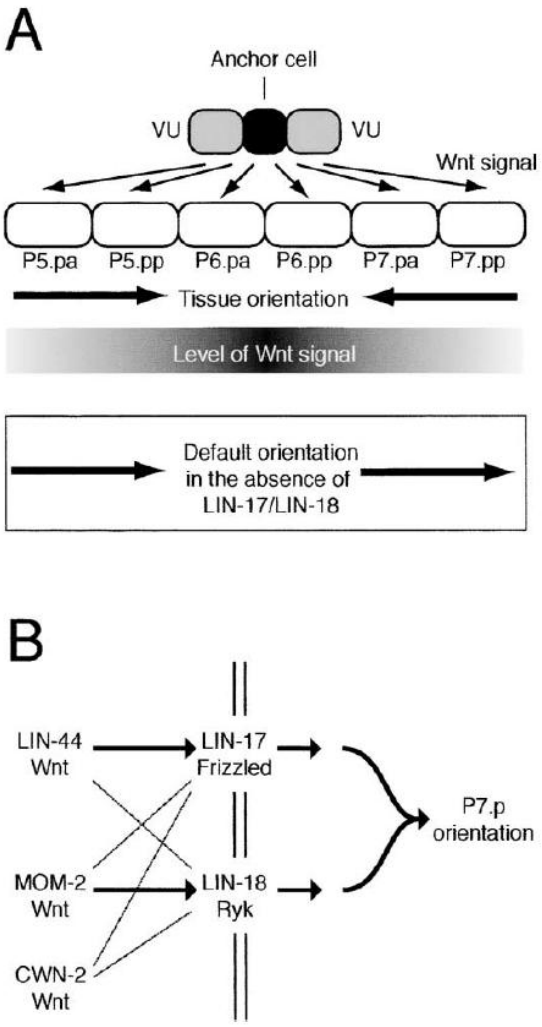

Figure 3.1 (A) A model for Wnt-dependent polarity control of P7.px (daughter cells of P7.p) orientation. (B) A model for the Wnt pathway-dependent regulation of the P7.p lineage. LIN-44 and MOM-2 interact preferentially with LIN-17 and LIN-18, respectively (bold lines). Figure adopted from Inoue *et al*. *C. elegans* LIN-18 is a Ryk ortholog and functions in parallel to LIN-17/Frizzled in Wnt signaling. *Cell* **118**, 795-806 (2004) [96].

Multiple Wnt ligand / receptors often act redundantly to their common downstream effectors and their activities are typically not simply additive [72] (Fig. 3.2). One possible explanation could be that the ligand / receptor activities are in their saturating regime. In such case, removing one will have negligible effect on its downstream factors. Another possibility is the existence of a reciprocal regulation between multiple ligand / receptor genes. For instance, the expression level of one ligand / receptor gene might increase as the expression level of the other (or others) decreases, thereby compensating for the loss-of-activity of its “partner”. However, it is still an open question how such redundancies are achieved in Wnt signaling pathways.

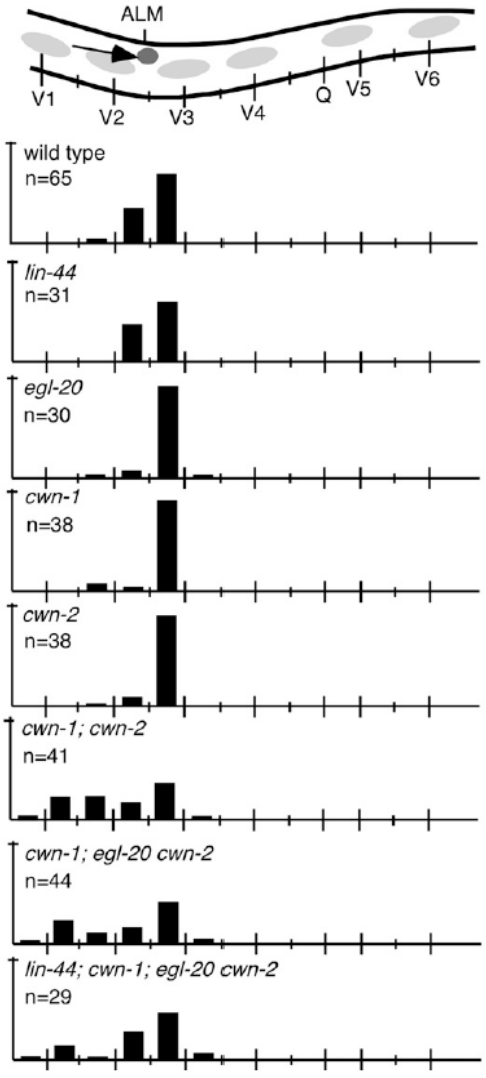

Figure 3.2 Wnt signaling controls the migration of anterior lateral microtubule neuron (ALM). Bars represent the percentage of ALM cells located at that position along the AP axis of L1 larvae. Mutations in single Wnt ligand mutants do not cause significant ALM migration defects. In contrast, mutations in multiple Wnt ligands cause significant defects. Figure adopted from Zinovyeva, A. Y., Yamamoto, Y., Sawa, H. and Forrester W. C. Complex network of Wnt signaling regulates neuronal migrations during *C. elegans* development. *Genetics* **179**, 1357-1371 (2004) [72].

Given the complexity of Wnt pathway components and their interactions, it is crucial to know when, where and how much each Wnt component is expressed additional to rigorous genetic analyses in order to investigate how individual developmental processes in different parts of the body at different times are controlled by Wnt pathway during *C. elegans* development. In this chapter, we provide an unprecedented high resolution Wnt mRNA expression map using single molecule mRNA FISH [23]. We avoided artifacts of genetic constructs which often lack unidentified key regulatory regions such as UTRs, intronic sequences, etc. This highly sensitive measurement technique also allowed us to detect novel Wnt expression patterns that were not reported previously, and we hope these findings would inspire future experiments which might unravel previously unidentified Wnt signaling activities in *C. elegans*.

Spatial correlations between the transcripts of Wnt ligand and secretory pathway components.

Wnt ligand proteins create a morphogenetic gradient along the antero-posterior body axis for their long-range signaling activity. Wnt ligand diffusivity and its secretion depend on multiple post-translational modifiers and trafficking proteins in the source cell [16,97]. *mig-14(wntless)* encodes a transmembrane Wnt cargo receptor protein that facilitates long-range Wnt signaling in *C. elegans* [91,97]. We questioned whether MIG-14 activity was preferential to specific Wnt ligands, and tried to answer this question by measuring spatial correlations in the expression of *mig-14* and five Wnt ligand genes in early L1 animals. The antero-posterior distribution of *mig-14* mRNA looked similar to that of Wnt ligand genes, but the levels were much low (Figure 3.3 A). In order to compare *mig-14* and/or Wnt expression patterns of multiple worms in the same developmental stage, we normalized the size of each animal by their body lengths and spatially overlayed them. Using the number densities transcripts, we were able to calculate a three dimensional correlation density plot of *mig-14* and Wnt ligand transcripts. As shown in the lateral view (Figure 3.3 B upper panel), the strongest correlation was present in the tail. We computed the number of *mig-14* transcripts that are present in the vicinity of each Wnt

ligand transcript within a spherical volume with a size of an average cell in worms. By plotting its distribution, we found that there were roughly two *mig-14* mRNA molecules present near each of *egl-20* and *lin-44* mRNA molecules while there was less than one near *cwn-1, cwn-2* and *mom-2* mRNA molecules (Figure 3.3 C). This spatial correlation between *mig-14* and *lin-44, egl-20* transcripts suggests that LIN-44 and EGL-20 are more likely to create long-range morphogenetic gradients from the posterior, whereas CWN-1, CWN-2, and MOM-2 are likely to signal at a relatively shorter range. We performed the same analysis for *mom-1(porcupine)*, which is another putative facilitator of Wnt ligand secretion thought to be involved in post-translational lipid modification although its precise role in Wnt secretion pathway is not clearly understood [97] (Figure 3.3 B bottom). Interestingly, *mom-1* expression level was much lower than that of *mig-14* (Figure 3.3 A). Only *egl-20* transcripts seemed to have a detectable spatial correlation with *mom-1* transcripts (Figure 3.3 D).

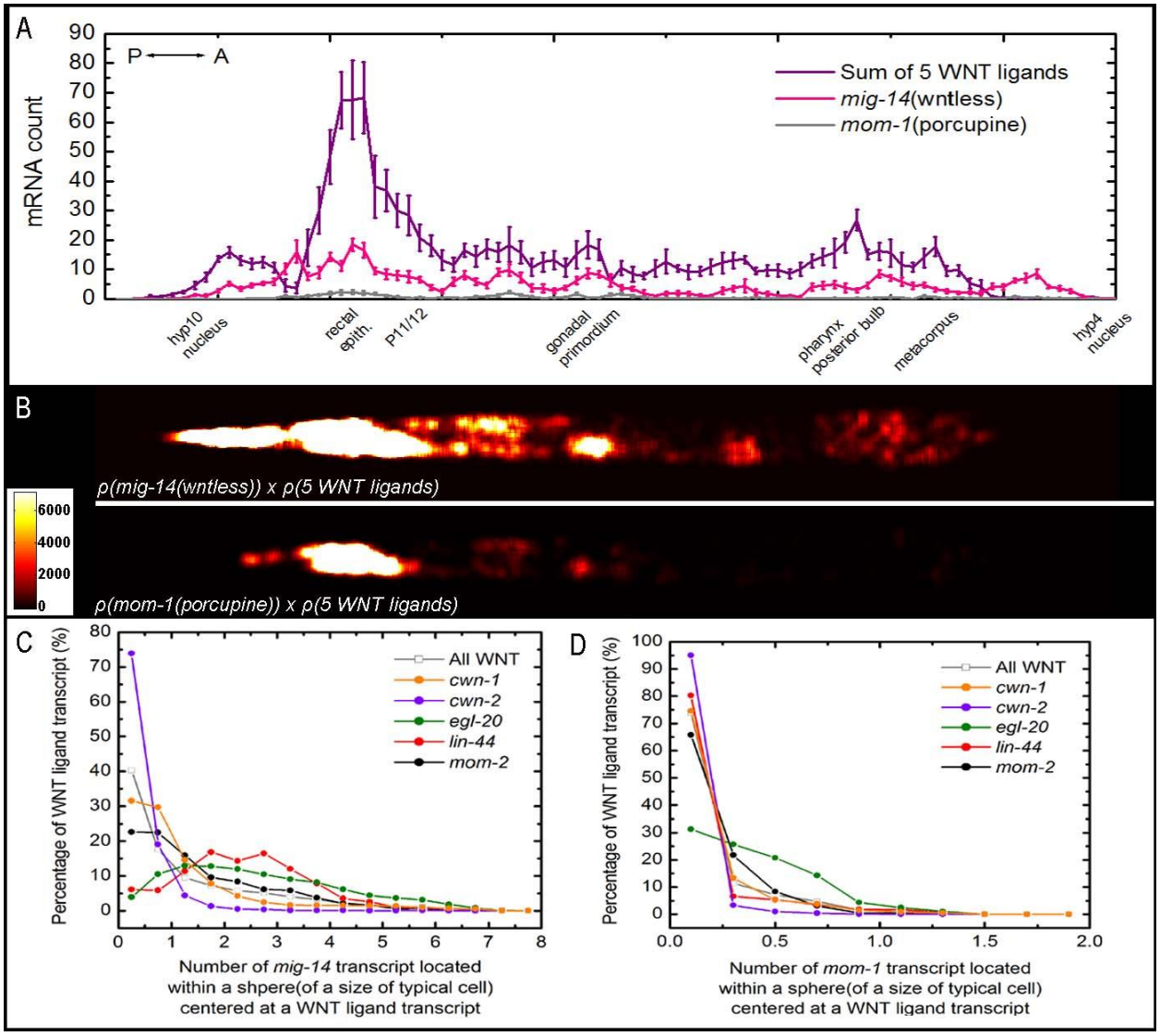

Figure 3.3 Transcript distribution of *mig-14(wntless)* and *mom-1(porcupine)* and their spatial correlation with Wnt ligand transcripts. (A) Antero-posterior expression profile of *mig-14(wntless)* and *mom-1(porcupine)* transcripts in wild types. Left is posterior and right is anterior. Error bars indicate standard error of the mean. (B) *mig-14(wntless)*-five Wnt mRNA spatial correlation heatmap (top) and *mom-1(porcupine)*-five Wnt mRNA spatial correlation heatmap (bottom). For both cases, three dimensional correlation density maps are sum-projected in the lateral direction. Left is posterior and right is anterior. Colorbar indicates the degree of correlation in arbitrary units. (C) Distribution of the number of *mig-14(wntless)* transcripts in vicinity of individual Wnt ligand transcript. *egl-20* and *lin-44* transcripts have higher spatial correlation with *mig-14(wntless)*

transcripts. There are on average roughly two *mig-14(wntless)* transcripts adjacent to a *egl-20* and a *lin-44* transcript. (D) Distribution of the number of *mom-1(porcupine)* transcripts in vicinity of individual Wnt ligand transcript. Only *egl-20* transcripts have detectable spatial correlation with *mom-1(porcupine)* transcripts.

The five *C. elegans* Wnt receptor genes are expressed in a series of partially overlapping domains along the antero-posterior axis

Consistent with the fact that numerous developmental processes of *C. elegans* are controlled via Wnt pathway, we observed five Wnt receptor encoding gene (*lin-17/Fz, lin-18/Ryk, mom-5/Fz, mig-1/Fz and cfz-2/Fz*) transcripts spanning the entire body, each possessing unique antero-posterior subdomains (Figure 3.4 A). *cfz-2* expression was restricted to neuronal, pharyngeal cells in head and tail region and no transcripts were observed in the middle region of the body until L4 stage when lateral seam cells started to express one or two transcripts (data not shown). Both *mom-5* and *mig-1* expression mostly spanned the middle region of the body including ventral cord neurons (VCNs) and intestinal cells. *lin-17* was mainly expressed in the posterior cells including rectal epithelial cells, posterior Pn.ps, VCNs, tail neurons and seam cells forming an overall posterior gradient of transcripts. *lin-18* spanned the body although majority of the transcripts were found in the head.

We were able to confirm predicted Wnt receptor expressions based on genetics studies and putative downstream target measurements that had been previously undetectable using existing standard reporters such as fluorescent proteins or lacZ reporters. For example, *lin-17* and *mom-5* were suggested to cause reciprocal asymmetric localization of SYS-1/beta-catenin and POP-1/TCF proteins in the germ line cells [98]. Indeed, *lin-17* transcripts were also visible in Z1 and Z4 descendants including the two distal tip cells(DTCs) and *mom-5* transcripts were expressed in all Z2 and Z3 descendants (germ line cells) throughout all larval stages, which was again genetically expected but

never observed before (Figure 3.4 B-D). Here we would like to point out that Z2 and Z3 lineage express both *mom-2/Wnt* and *mom-5* at all times, although later during vulva development somatic gonad cells such as AC and VU also express *mom-2/Wnt* (Figure 3.4 D and Figure 3.5 C). We also observed *lin-17* transcripts in P11/12LR cells in hatchlings which support the model that P12 fate is determined by *lin-44*/*Wnt* signaling via *lin-17* receptor during the first larval stage (Figure 3.4 E) [84]. The migration of Q neuroblast progeny is a well studied model system controlled by canonical Wnt pathway and *egl-20/Wnt* ligand, *lin-17* and *mig-1* receptors were the genetically known key genes of this pathway [71]. We detected mRNA molecules of the two receptors in QL and QL.d located anterior to *egl-20/Wnt* ligand source cells in L1 animals (Figure 3.4 F – only *lin-17* is shown).

Our data suggest an in-depth study of *mom-2* expression in Z2 and Z3 descendants and its effect on gonad arm elongation. The somatic gonadal precursor cells (SGPs), or Z1 and Z4, continue to divide asymmetrically to generate a “distal tip cell” (DTC) which controls the elongation of two gonad arms and a “proximal cell” with potential to become an anchor cell (AC). This asymmetry is shown to be specified by SYS-1/beta-catenin and POP-1/TCF reciprocal asymmetry established via *lin-17* and *mom-5* receptors [98]. However, no Wnt ligand gene has been identified as the upstream signaling component of this pathway so far. Our data suggests *mom-2* to be a highly probable candidate since it is expressed at the symmetry axis of the two gonad arms which has the potential to have symmetric and identical effect on the two SGPs migrating away as a mirror image.

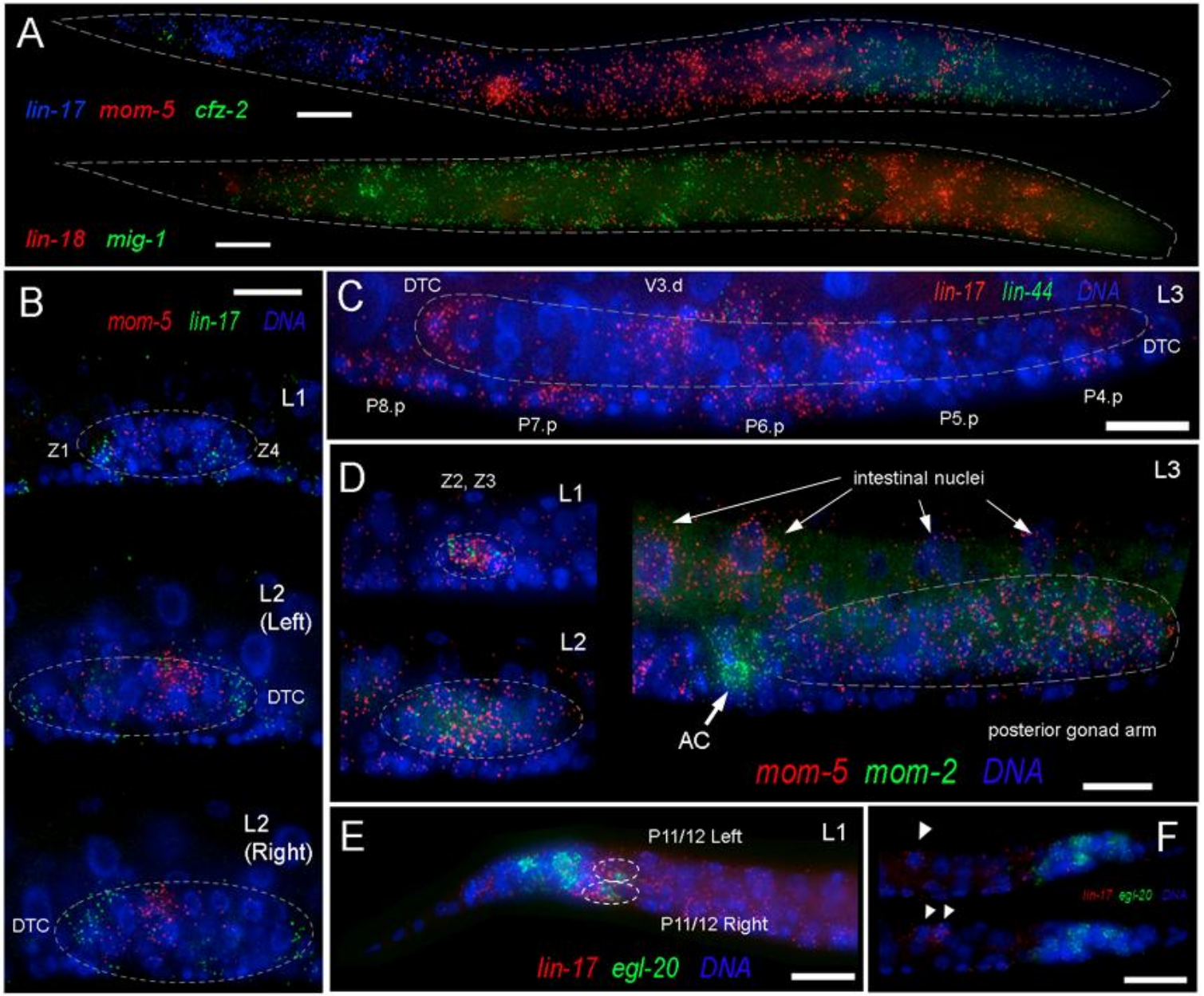
A
lin-17 mom-5 cfz-2
lin-18 mig-1
B
mom-5 lin-17 DNA
L1
Z1
Z4
L2
(Left)
DTC
L2
(Right)
DTC
C
DTC
V3.d
lin-17 lin-44 DNA
L3
DTC
P8.p
P7.p
P6.p
P5.p
P4.p
D
Z2, Z3
L1
L2
intestinal nuclei
L3
AC
posterior gonad arm
mom-5 mom-2 DNA
E
P11/12 Left
L1
P11/12 Right
lin-17 egl-20 DNA
F
lin-17 egl-20 DNA

Figure 3.4 Wnt receptor mRNA expression in *C. elegans* larvae. (A) Each Wnt receptor gene is expressed within its own anteroposterior domain. *lin-17* is expressed mainly in the posterior body. *mom-5* has a broad expression domain in the mid-body. Note *mom-5* expression in the germ line cells. *cfz-2* expression is found in the head and tail regions. *lin-18* is expressed broadly along the body but most highly in the head. *mig-1* was expressed mainly in the mid-body region. (B) Wnt receptor expression in the germ line and somatic gonad. *lin-17* expression in somatic gonad cells including distal tip cells (DTCs) and *mom-5* expression in germ line cells are shown. Dashed curve outlines the gonad. (C) *lin-17* expression in the somatic gonad at L3. *lin-44/Wnt* ligand expression in V3.d and P6.p can be found at this stage. Dashed curve outlines the gonad. (D) *mom-2/Wnt* and *mom-5* expression persists throughout larval period in the germ line cells. One exception is the high *mom-2/Wnt* expression in the anchor cell (AC) at L3 stage. Dashed curve outlines the gonad. (E) *egl-20/Wnt* and *lin-17* are co-expressed in P11/12 LR cells in L1 animal. (F) Q neuroblast cells express *mig-1*. Arrowheads indicate Q (top) and its daughter cells (bottom). All scale bars indicate 10μm.

Novel Wnt ligand expression in developing vulva and its surrounding cells.

C. elegans vulva is an egg-laying apparatus formed during postembryonic development by a series of divisions and fusions of ventral epidermal vulval precursor cells (VPCs) induced by multiple intercellular signaling pathways [99]. During L1 and L2, six ventral hypodermal Pn.p cells, from P3.p to P8.p, become competent to receive developmental signals and form the vulva later on. During L3 stage, VPCs receive *lin-3/EGF* (epidermal growth factor) signal from the anchor cell (AC) embedded in the gonad dorsal to the VPC array. Since VPCs are positioned linearly along the ventral cord, each VPC receive different amounts of LIN-3 signal depending on the distance from the AC and this differential signaling is reinforced by lateral Notch signaling. In particular, P6.p which is the closest to AC adopts 1° (primary) fate while P5.p and P.7p adopts 2° (secondary) fate and VPCs with different fate give rise to distinct progeny accordingly. P3.p, P4.p

and P8.p fuse to hyp7 epidermis as a result of adopting 3° (tertiary) fate. Wnt signaling is required for maintaining VPC competence in L2 stage and symmetric polarity of P5.p and P7.p descendants in late L3 stage [75,100–102]. Although previous genetic studies have identified specific Wnt genes and their redundant functions that are necessary for vulval development, the location, amount and timing of Wnt expression are still under-explored. Using single molecule FISH, we have found Wnt expression not only in various cells near the developing vulva including AC, uterus, muscles and neurons, but also in the VPC lineage itself.

The most obvious Wnt ligand expressed in the developing vulva is *lin-44*. P6.p, a VPC located at the symmetry axis of the vulva, starts to express *lin-44* at mid-late L2 and this is continued throughout the entire lineage of P6.p descendants (Figure 3.5 A) In the previous study by Inoue et al., LIN-44 protein was observed in AC, and a more recent study suggested that LIN-44 from AC might be necessary for refined P7.p polarity [96,102]. However, here we clearly show that *lin-44* is expressed in P6.p lineage but not in AC. In addition, we observed transient *lin-44* expression in lateral seam cells derived from V3 by the time Pn.p cells divided (Figure 3.5 A-C, E, F and Figure 3.6). It is possible that these expressions might altogether instruct P7.p daughter cells to orient towards the center along with *mom-2* expressed in AC. We were curious to see whether *lin-44* is a primary VPC fate marker. To test this, we labeled *lin-44* transcripts in *lin-15AB(e1763)* mutant animals where ectopic LIN-3 over-expression in hypodermal cells results in multiple VPCs adopting primary fate to develop multiple ectopic vulva (Synthetic Multi-Vulva (SynMuv) phenotype) [103]. We found *lin-44* transcript expression in multiple primary VPC lineages, indicating that *lin-44* expression is indeed a reliable marker for primary VPCs (Figure 3.7).

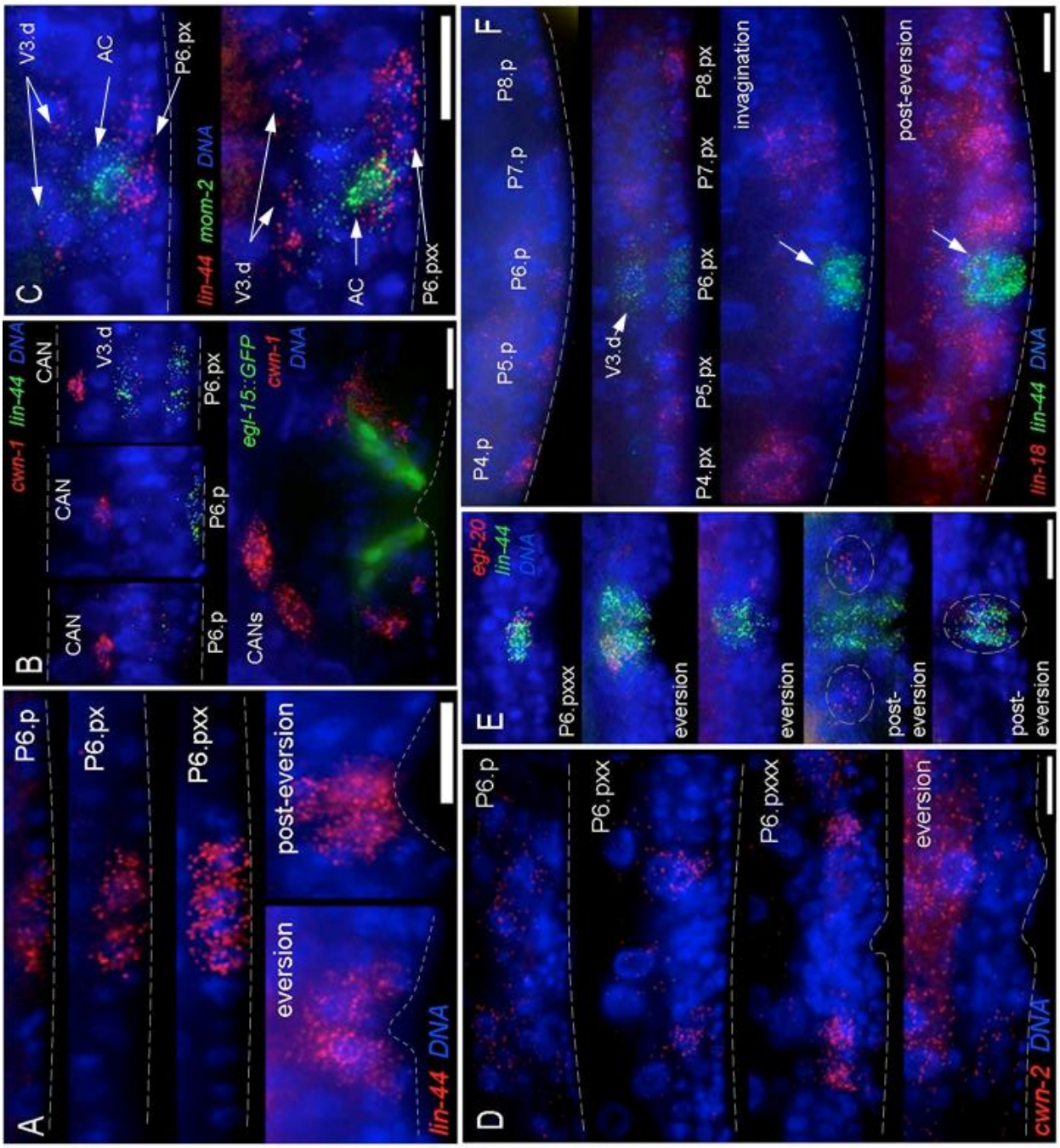

Figure 3.5 Wnt ligand genes are expressed in the developing vulva and its surrounding cells. (A) *lin-44* is expressed in P6.p and its descendants during vulva development. (B) CAN Left and Right cells are dorsally located to the developing vulva and expressed *cwn-1*. During late vulva development, *cwn-1* expression is also found in a subset of sex muscle cells. *egl-15::GFP* is shown to label vm1 cells. (C) High *mom-2* expression in the anchor cell (AC) and to a lesser extent in the surrounding VU cells. (D) *cwn-2* is

expressed in M cell descendants and intestinal cells. (E) *egl-20* is expressed in P6.p and its descendants together with *lin-44*. However, we occasionally found *egl-20* expression in symmetrically located cells neighboring P6.p lineage. (F) *lin-18(Ryk)* is expressed in Pn.p and uterine cells. All scale bars indicate 10μm.

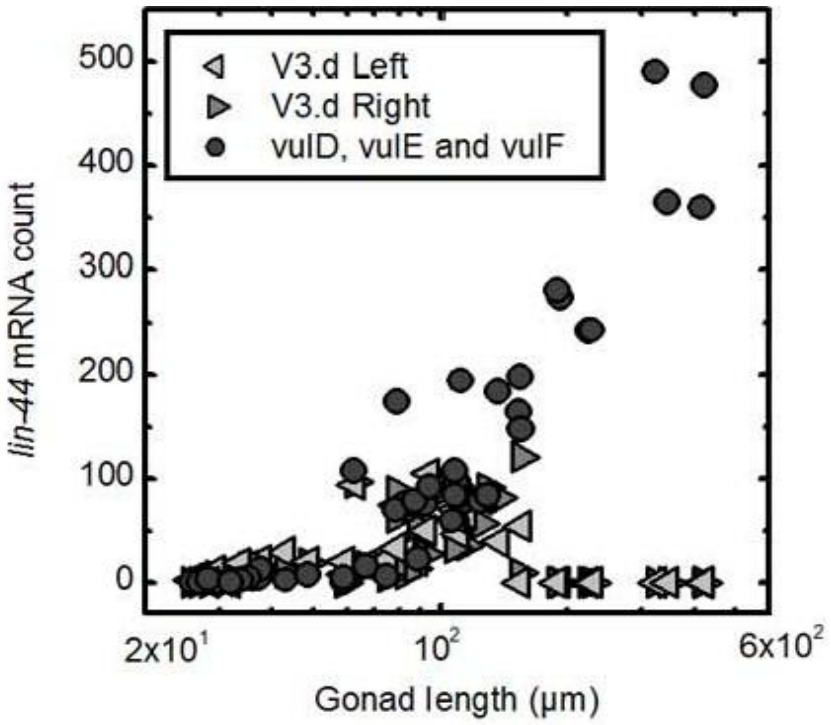

Figure 3.6 *lin-44/Wnt* expression in the primary fate VPC lineage of wild-types.

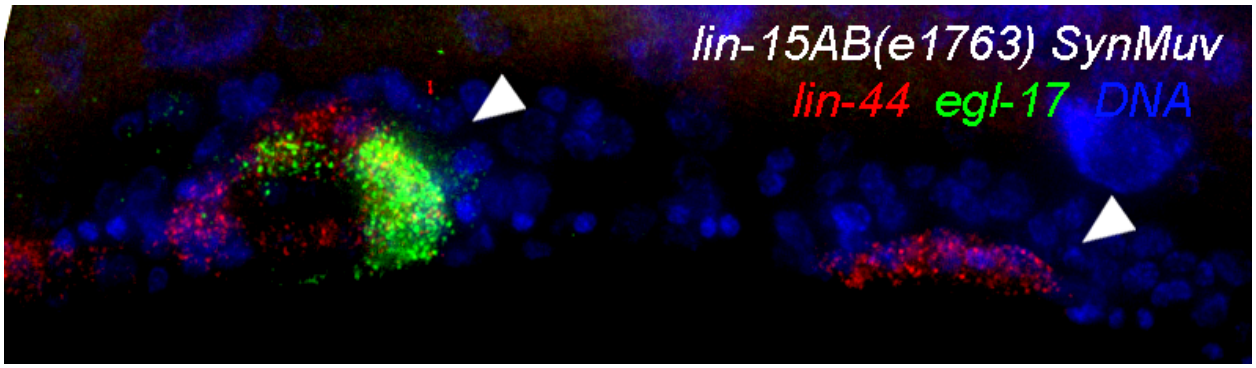

Figure 3.7 *lin-44/Wnt* expression in primary VPCs of *lin-15AB(e1763) SynMuv* animals. Arrowheads indicate vulvae.

Another interesting Wnt ligand expression pattern we observed regarding to developing vulva is the constituitive *cwn-1* expression in two lateral canal associated neurons (CANs) which are dorsal to VPCs (Figure 3.5 B). Again, *cwn-1* is expressed in these cells from mid-late L1 and persists throughout post embryonic development (Figure 2.2 B). Although posterior body wall muscles are the major sources of *cwn-1* throughout development, CANs are the most closely located sources of *cwn-1* with high expression level at least until late L3 stage. Previous work by Myers et al. 2007 [101] showed that *cwn-1* and *egl-20* play a major role to prevent VPCs from adopting tertiary fate and fusing to hypodermal syncytium, hyp7. Since *cwn-1* is a Wnt ligand encoding gene that has an expression pattern with less spatial correlation with *mig-14(wntless)* and *mom-1(porcupine)* (Figure 3.3 C,D), *cwn-1* might act at short distances to promote VPC competence during L2-L3. We also observed *cwn-1* transcripts in sex muscle cells (we did not identify the specific type of these cells) surrounding the vulva at L4 (Figure 3.5 B - *egl-15::GFP* is shown to visualize vm1 cells). *egl-20* has been reported to be secreted from several cells in the tail to form a posterior morphogen gradient and act as one of the most dominant source of antero-posterior polarity of various cells during larval development [16,74]. Interestingly, genetic studies have indicated that fates and polarities of cells not only near the tail but also those distant from the tail such as migratory neurons and even VPCs are affected by *egl-20* signaling [102,104]. However, it is unclear whether EGL-20 protein secreted from the tail can be readily diffused to

reach the middle or anterior part of the body especially during the later larval period when animal's body length increase rapidly. In this study, we found *egl-20* expression in P6.p descendants during VPC invagination, eversion, and later in four cells surrounding the vulva and expression in these two regions seemed to be mutually exclusive (Figure 3.5 E (compare fourth and fifth panels) and Figure 3.8, arrow). In addition, we occasionally found *egl-20* transcripts in the gonad (Figure 3.8, bounded by a dashed outline) and in one cell that is dorsal to the vulva (Figure 3.8, arrowhead). This expression might play important roles for setting P5.p and P7.p lineage orientation towards the center of the developing vulva together with LIN-44 from P6.p descendants and MOM-2 from AC, given the long distance between the developing vulval and EGL-20 expressing cells in the tail. We also probed *cwn-2* expression near the vulva and observed expression in intestinal cells and M cell descendants near the vulva. However, we did not observe any *cwn-2* expression in VPCs (Figure 3.5 D).

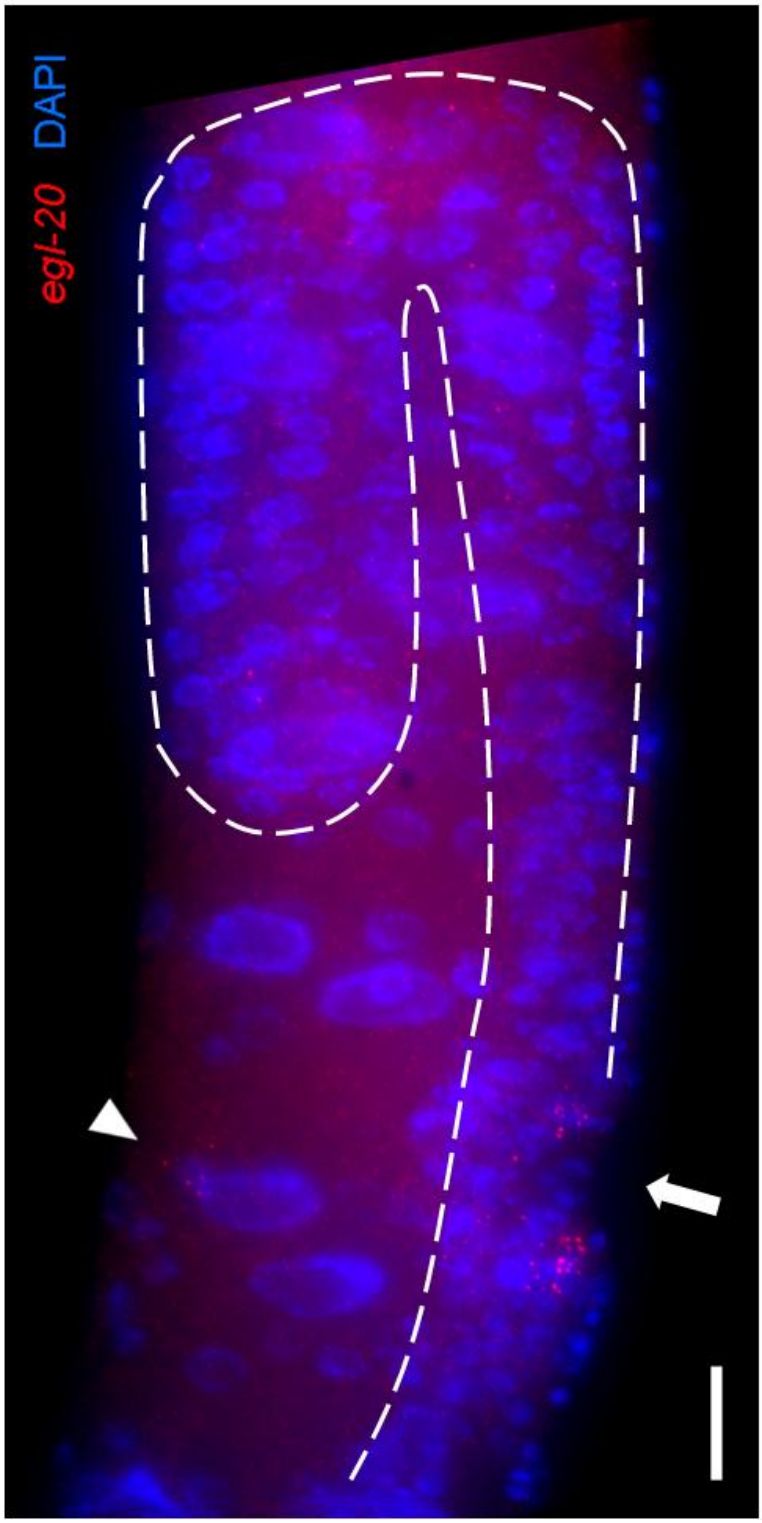

Figure 3.8 egl-20 is expressed in the gonad, vulva and an unidentified cell located dorsal to the vulva. Scale bar represents 10µm.

Chapter 4. Temporal gradients of developmental timing gene expressions are actively screened from global fluctuations

In this chapter, we describe how microRNA-mediated feed-forward loops can screen a temporal gradient from transcriptome-wide fluctuations during *C. elegans* post-embryonic development.

4.1 Summary

Building a multi-cellular organism from a small group of cells involves coordinated execution of developmental processes in a highly dynamic and fluctuating environment. Stochastic molecular events or global intracellular fluctuations in cellular components might affect expression levels of developmental genes and create uncertainties in developmental outcomes [50]. We find that in the nematode *Caenorhabditis elegans* the majority of the transcriptome displays pulsatile dynamics peaking several times during larval development. This raises the question how key regulators of developmental timing, the microRNA (miRNA) *lin-4* and its targets *lin-14* and *lin-28* [43,46,105], are insulated from these dynamical fluctuations. By counting transcripts in individual animals, we show that the miRNA tightly controls the expression levels of its targets effectively screening them from the pulsatile transcriptome. Consistently, in the absence of the miRNA the transcript levels of the miRNA targets display pulsatile dynamics resembling the majority of the transcriptome. Our results demonstrate that these fluctuations are effectively dampened in the wild-type organism by synchronous pulsatile expression of the miRNA and its targets. We propose that such a microRNA-mediated incoherent feed-forward loop [106] is a potent filter that prevents propagation of potentially deleterious gene expression fluctuations during the development of the organism.

4.2 Majority of the *C. elegans* transcriptome displays pulsatile dynamics during larval development

To explore the dynamics of the *C. elegans* transcriptome during larval development, we conducted RNA-Seq experiments using poly(A)$^+$ RNA libraries prepared from synchronized larval populations representing 20 different developmental time points ranging from 0 hr to 38 hr after hatching with 2 hr resolution at 20°C. This range spans the first three larval stages (L1, L2, and L3). We used the Illumina HiSeq 2000 platform to generate single-end 40-bp reads. In our analysis, we discarded RNA species that had an average RPKM (reads per kilobase of exon model per million mapped reads) [107] of less than one and detected 21,129 reliably expressed annotated transcript species. We first examined how the transcriptome-wide gene expression levels varied by computing the pair-wise correlations between transcriptomes at different developmental time points (Fig. 4.1a). Interestingly, we found that the pair-wise correlations did not monotonically decrease when comparing more distant time points. For example the correlation coefficient between time points 10 hr and 16 hr is smaller than between 10 hr and 22 hr (Fig. 4.1a). To test whether this was a developmental effect, we cultured synchronized larval populations at 25°C. At this elevated temperature, animals develop normally but at an accelerated rate. For this reason, we harvested poly(A)$^+$ RNA libraries every 1.5 hr and found a strikingly similar pair-wise correlations to that of results obtained at 20°C (Fig. 4.1b). This suggested that the *C. elegans* transcriptome is developmentally modulated periodically during larval development. To detect periodic signals in expression levels of individual transcript species we computed the autocorrelation function of the RPKM time series and found the periods of 12 hr and 24 hr to be enriched at 20°C, and 9 hr and 16.5 hr at 25°C (Fig. 4.1c-d, 4.7 Supplementary Information). We interpret that the dominant short periods are caused by transcripts that peak three times during the course of the time-series and therefore peak approximately once per larval stage.

To test this more directly, we classified transcripts into four dynamical groups (4.7 Supplementary Information and Supplementary Fig. 4.1). The first three classes contain genes that display pulsatile gene expression dynamics with 1 pulse / stage, 1 pulse/ 2 stages, or 1 pulse / 3 stages. The fourth class contains genes that resemble graded, non-pulsatile, dynamics. Surprisingly, the majority of the transcript species was classified as pulsatile, exhibiting at least one expression pulse during larval growth (Fig. 4.1e). Reassuringly, we correctly classified previously reported genes with oscillatory expression such as nuclear hormone receptor *nhr-25* [108], collagen encoding molting genes *dpy-5* and *dpy-10* [109], and the Period homologue *lin-42* [110]. Furthermore, we found overrepresented enrichment of house-keeping genes in the pusatile groups (Supplementary Fig. 4.2), suggesting that such dynamical expressions may have transcriptome-wide influences.

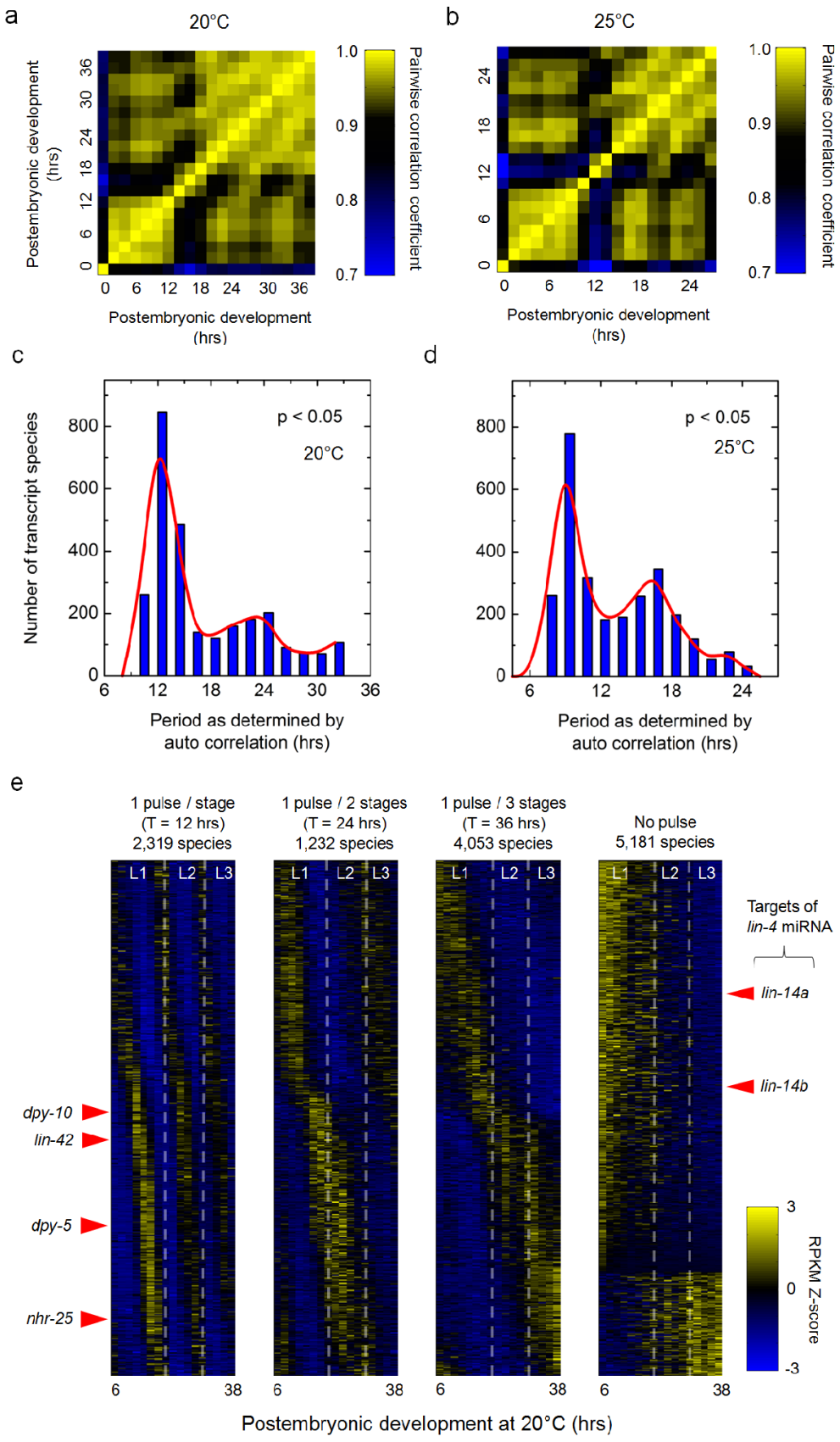
a
20°C
Postembryonic development (hrs)
0 6 12 18 24 30 36
Postembryonic development (hrs)
Pairwise correlation coefficient
1.0 0.9 0.8 0.7
b
25°C
0 6 12 18 24
Postembryonic development (hrs)
Pairwise correlation coefficient
1.0 0.9 0.8 0.7
c
Number of transcript species
0 200 400 600 800
p < 0.05
20°C
6 12 18 24 30 36
Period as determined by auto correlation (hrs)
d
0 200 400 600 800
p < 0.05
25°C
6 12 18 24
Period as determined by auto correlation (hrs)
e
1 pulse / stage (T = 12 hrs) 2,319 species
1 pulse / 2 stages (T = 24 hrs) 1,232 species
1 pulse / 3 stages (T = 36 hrs) 4,053 species
No pulse 5,181 species
L1 L2 L3
Targets of lin-4 miRNA
lin-14a
lin-14b
dpy-10
lin-42
dpy-5
nhr-25
3 0 -3
RPKM Z-score
6 38
Postembryonic development at 20°C (hrs)

Figure 4.1 Majority of the *C. elegans* transcriptome displays pulsatile dynamics during larval development. a-**b**, Pairwise correlation of transcriptomes between different developmental times determined by poly(A)$^+$ RNA-seq. 20°C (**a**) and 25°C (**b**). **c**-**d**, Distribution of periods determined by autocorrelation analysis. 20°C (**c**) and 25°C (**d**). Red curve represents a spline fit of the histogram. Species with $p<0.05$ are shown. **e**, Classification of transcript species into four dynamical groups. Each column is ordered in phase. Scale bar indicates Z-scores of RPKM. Species with significant p-values are shown (false discovery rate 0.1). Red arrowheads indicate locations of the specified transcript species. Dashed lines separate larval stages.

4.3 *lin-4* miRNA expression is pulsatile whereas the mRNA levels of its targets *lin-14* and *lin-28* are graded in wild-types

Given the pulsatile dynamics of the majority of the transcripts, it is intriguing to observe how well the expression levels of the genes in the graded class are insulated from the remaining fluctuating transcriptome. Among the genes in this group is the important developmental timing regulator *lin-14* [43–45] (Fig. 4.1e), gene products of which trigger dosage-dependent larval stage-specific programs. Control of this temporal gradient is mediated by *lin-4* miRNA, a short non-coding RNA that base pairs with its complementary elements in the 3'-untranslated region (3'-UTR) of *lin-14* [105] transcripts thereby reducing protein synthesis either by transcript destabilization [111] or translation inhibition [112,113]. *lin-28* is another developmental time regulator that is also an experimentally validated target of *lin-4* [43,46]. When *lin-4* mediated repression is lost, LIN-14 and LIN-28 protein level remains high [44–46] and animals display a "retarded" phenotype where cells variably reiterate early developmental programs [35,43,114] and fail to form reproductive organs [43,115]. The importance of the gradually decreasing *lin-14* and *lin-28* expression was first inferred from genetic analyses [44,46], which suggested that cells in wild-type animals can distinguish distinct levels of these gene's activities at specific times during the first two larval stages. Taken

together, this suggests that for proper larval development *lin-14* and *lin-28* have to be carefully screened from the highly dynamic and pulsatile transcriptome (Fig. 4.1e).
To study whether *lin-4* plays any role in screening *lin-14* and *lin-28* from transcriptome-wide fluctuations, we first measured mature *lin-4* miRNA levels in total RNA extracts harvested from staged larvae using a quantitative real-time PCR assay for small RNA detection (see section 4.8 Methods). To our surprise, mature *lin-4* expression was pulsatile, peaking approximately once per larval stage (Fig. 4.2a-b). We also investigated the activity of the *lin-4* promoter by measuring the transcript levels of a *lin-4* promoter-*GFP* fusion construct [116] (Fig. 4.2c). The *lin-4* promoter was ubiquitously active in somatic cells but not in the germ line, in agreement with previous reports [116]. Strikingly, we found the promoter activity of *lin-4* to alternate between high and low during post-embryonic development with a period of approximately one larval stage (Fig. 4.2c), suggesting that the pulsatile mature *lin-4* miRNA levels (Fig. 4.2a-b) are transcriptionally regulated.

Intrigued by the this dynamic expression of *lin-4* miRNA, we decided to obtain detailed expression dynamics of the *lin-4* targets, and counted individual *lin-14* and *lin-28* transcripts in intact animals using a single molecule fluorescence *in situ* hybridization method [23] (Fig. 4.2d). We obtained high temporal resolution by estimating the post-embryonic age of individual animals from body length, defined as the distance between the anterior-most nucleus hyp4 and the posterior-most nucleus hyp10 along the antero-posterior (AP) axis (Fig. 4.2e, Supplementary Fig. 4.3, 4.4, 4.5). *lin-14* and *lin-28* transcripts were detected ubiquitously throughout the body in all previously reported expressing cells [45,46] of wild-type animals during all larval stages, from L1 to L4 (Fig. 4.2d). The only exceptions were germ line and somatic gonad cells where *lin-28* but no *lin-14* transcripts were observed. We determined mRNA concentrations at each developmental time point by normalizing the total transcript count to the volume of the worm [117] (Supplementary Fig. 4.6). We found that *lin-14* and *lin-28* mRNA concentrations form smooth temporal gradients during postembryonic development (Fig. 4.1e and Fig. 4.2f-g). To test whether these expression dynamics were observed consistently along the AP axis, we generated AP mRNA density maps (Supplementary

Fig. 4.7). We found that, with the exception of the head, tail and germ line regions where cell densities are higher, *lin-14* and *lin-28* transcripts were equally distributed along the mid-body region and were uniformly down-regulated during larval development, recapitulating the dynamics observed in the whole animal (Fig. 4.2f-g).

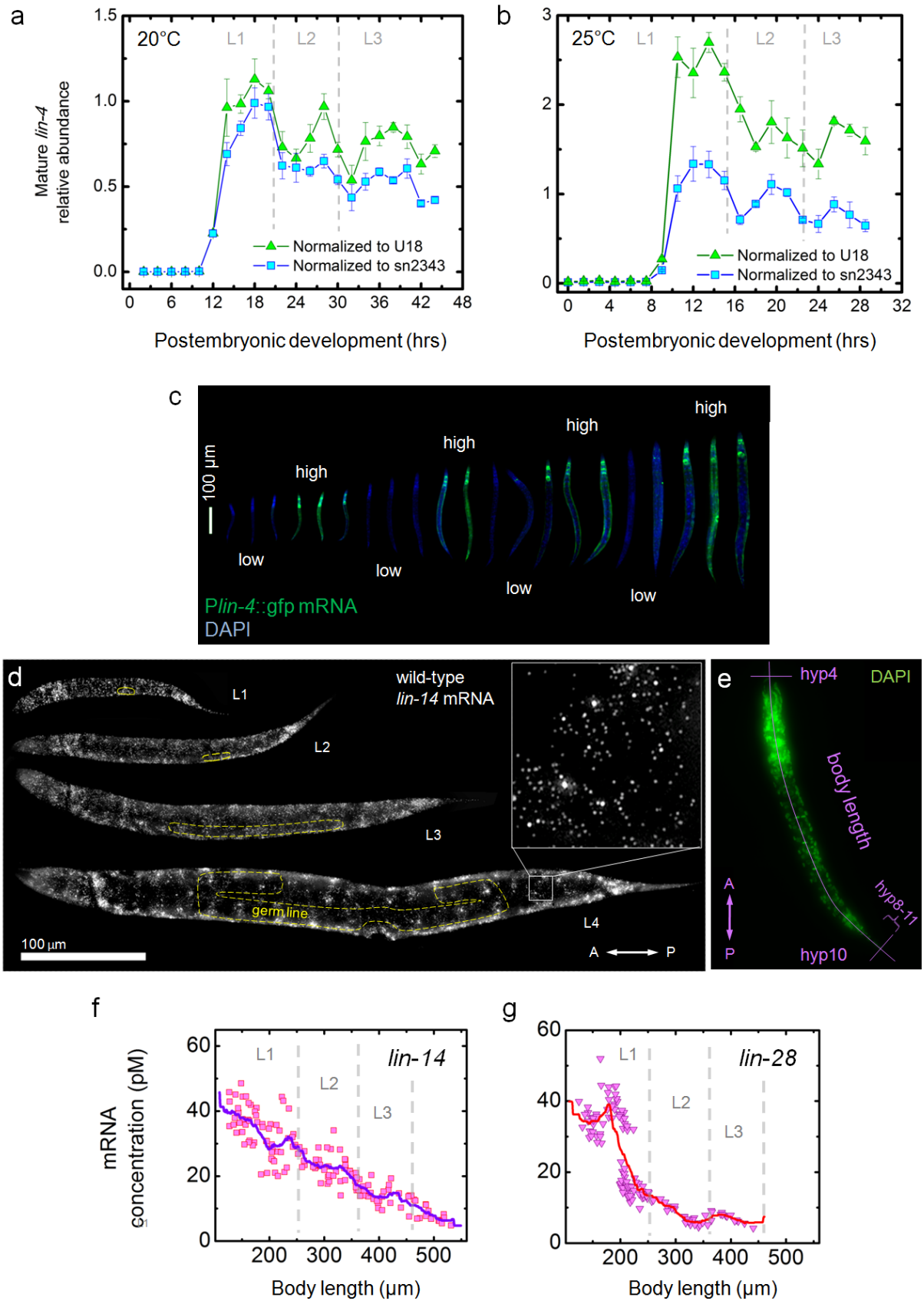
a
20°C
L1
L2
L3
Mature lin-4
relative abundance
Normalized to U18
Normalized to sn2343
Postembryonic development (hrs)
b
25°C
L1
L2
L3
Normalized to U18
Normalized to sn2343
Postembryonic development (hrs)
c
100 µm
high
low
Plin-4::gfp mRNA
DAPI
d
wild-type
lin-14 mRNA
L1
L2
L3
L4
germline
100 µm
A
P
e
hyp4
DAPI
body length
hyp8-11
hyp10
A
P
f
mRNA
concentration (pM)
lin-14
L1
L2
L3
Body length (µm)
g
lin-28
L1
L2
L3
Body length (µm)

Figure 4.2 *lin-4* miRNA expression is pulsatile while the mRNA levels of its targets *lin-14* and *lin-28* are graded in wild-type. a-**b**, Mean mature *lin-4* level of staged larvae determined by Taqman qPCR. 20°C (**a**) and 25°C (**b**). Error bars, s.d.; n>3. Dashed lines in **a**-**b** separate larval stages. **c**, *Plin-4::gfp* smFISH (red) and DAPI(blue) images of staged larvae are merged and ordered by their body lengths. Scale bar indicates 100µm. **d**, Maximum z-projection of *lin-14* smFISH stack images of staged larvae. Transcripts are visualized as countable fluorescent spots (inset). Yellow dashed lines outline the germ line. Scale bar indicates 100 µm. **e**, Body length determined from DAPI staining. **f**, overall *lin-14* mRNA concentration of individual animal as a function of body length. **g**, overall *lin-28* mRNA concentration of individual animal as a function of body length. Curves in **f**-**g** indicate moving averages (bin; 36µm). Dashed lines in **f**-**g** separate larval stages.

4.4 *lin-14* and *lin-28* mRNA levels exhibit pulsatile dynamics in the absence of *lin-4* negative regulation

The pulsatile dynamics of the *lin-4* miRNA is difficult to reconcile with the smooth temporal gradients observed for *lin-14* and *lin-28*, which are direct targets of *lin-4* [46,105]. To explore why the pulsatile dynamics of *lin-4* is not propagated to its targets, we measured *lin-14* mRNA concentration in *lin-4(e912)* knock-out mutant animals (Fig. 4.3a). During early L1, *lin-14* transcript levels in these mutant animals were identical to that of wild-type animals. However, as larvae entered late-L1, the *lin-14* concentration started to exhibit large peaks in the absence of *lin-4*. The peaks occurred approximately once per larval stage. Peaking *lin-14* transcript levels were also observed from our RNA-Seq experiment in these mutants (Supplementary Fig. 4.8). Moreover, the transcript levels of predicted LIN-14 downstream genes [118] were affected at times when *lin-14* transcript levels peaked, suggesting that LIN-14 protein levels are also peaking in these mutants (Supplementary Fig. 4.9, 4.10). We questioned whether this

pulsatile dynamics was also present at the level of individual cells and measured *lin-14* mRNA in a group of hypodermal cells, hyp8-11 (five nuclei), at the tail tip which increase in volume but do not divide [70] (Fig. 4.3b). The *lin-14* mRNA dynamics in these cells were qualitatively similar to those observed in the entire animal. We also generated a *lin-14* transcript fold-change map and found that such de-repression in the absence of *lin-4* activity was present globally along the AP axis (Fig. 4.3c). Each colored bin indicates the fold-change of *lin-14* transcript numbers in *lin-4(912)* animals compared to wild-type animals at a given location along the AP body axis and at a given post-embryonic age. We considered the developmental age of wild-type and mutant animals of identical body length to be approximately the same (Supplementary Fig. 4.3, 4.4, 4.5). Recurring vertical bands in this map reflect the fact that the timings of *lin-14* transcript level pulses are synchronized in every segment of the animal body along the AP axis. We examined the mid-body region of the animals which is uniformly comprised of hypodermal, intestinal and muscle cells, and indeed found a transient ~3-fold repression of *lin-14* transcript level in the wild-type compared to *lin-4(e912)* animals during the L1 stage and another transient ~2-fold repression during the L2 stage (Fig. 4.3d). The strength of the transient repression was further reduced during the L3 stage, reaching a steady ~1.5-fold repression.

To examine whether the pulsatile *lin-14* transcript levels observed in *lin-4(e912)* animals were caused by the absence of the direct interaction between *lin-4* and the *lin-14* 3'-UTR, we counted *lin-14* transcripts in *lin-14(n355gf)* animals (Supplementary Fig. 4.11), which lack all of the seven putative *lin-4* complementary elements (LCE) due to genomic rearrangements [112,119]. We found that *lin-14* mRNA levels also exhibited pulsatile dynamics in *lin-14(n355gf)* animals similar to those observed in *lin-4(e912)* animals (Fig. 4.3a-b). In addition, we measured transcripts in *lin-14(n536gf)* animals which carry only two LCEs due to a deletion in the 3'-UTR [112,119] and observed a similarly spaced train of peaks with reduced amplitudes (Supplementary Fig. 4.12). These data suggest that the pulsatile *lin-14* expression observed in mutant animals are attributed to the loss of a direct interaction between *lin-4* and the *lin-14* 3'-UTR.

We also measured *lin-28* mRNA concentration in *lin-4(e912)* knock-out mutant animals (Fig. 4.3e). Similar to *lin-14*, there were fluctuations in the expression of *lin-28* and pulsatile transcript levels were also present, peaking approximately once per larval stage. The relative heights of these peaks, however, were small compared to that of *lin-14*. A similar oscillatory pulsatile expression was observed in the tail hypodermal cells (Fig. 4.3f).

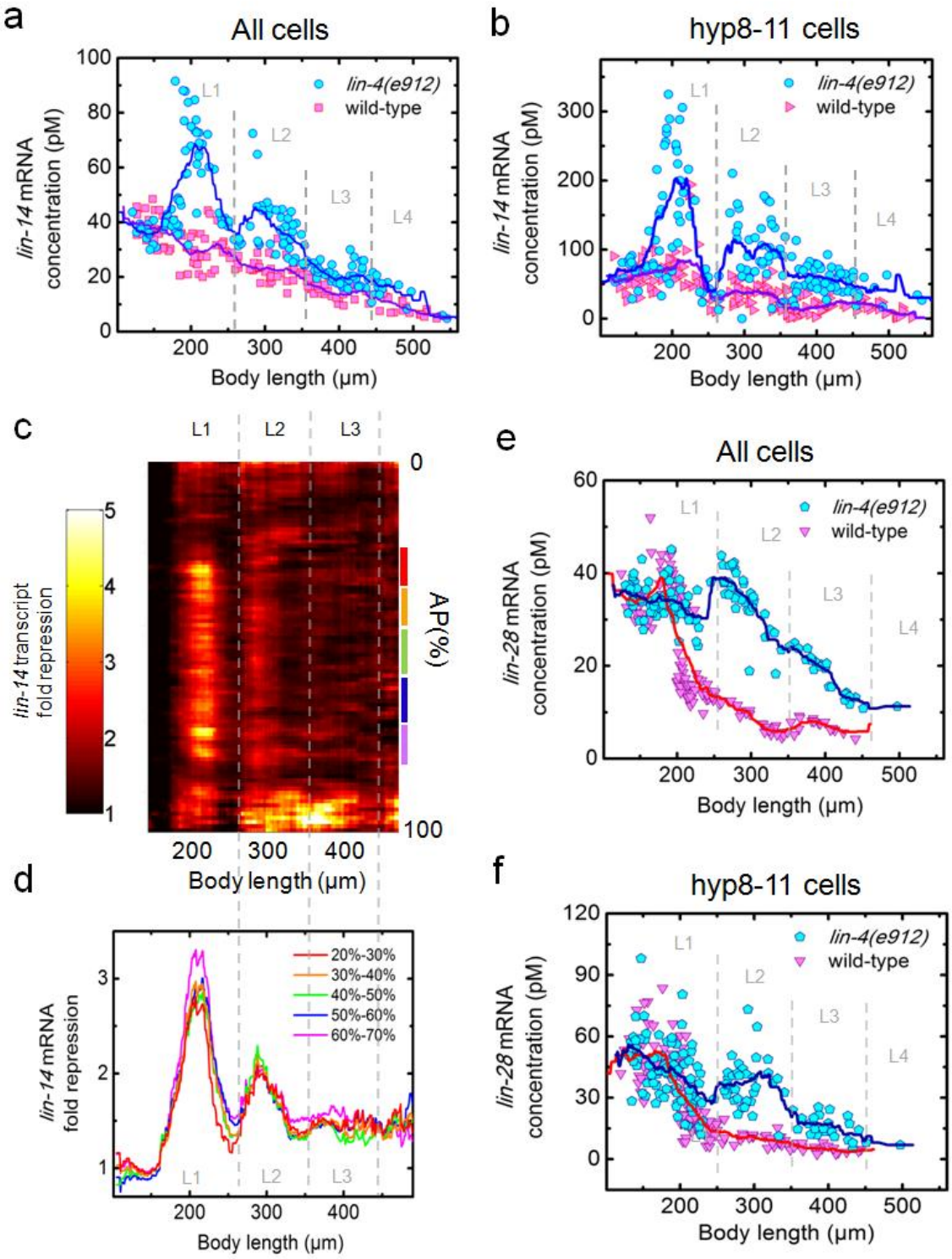
a
All cells
lin-14 mRNA concentration (pM)
lin-4(e912)
wild-type
L1
L2
L3
L4
Body length (μm)
b
hyp8-11 cells
c
lin-14 transcript fold repression
AP(%)
d
lin-14 mRNA fold repression
20%-30%
30%-40%
40%-50%
50%-60%
60%-70%
e
All cells
lin-28 mRNA concentration (pM)
f
hyp8-11 cells

Figure 4.3 *lin-14* and *lin-28* mRNA levels exhibit pulsatile dynamics in the absence of *lin-4* negative regulation. **a**-**b**, *lin-14* mRNA concentration dynamics of individual *lin-4(e912)* mutants as a function of body length. Overall concentration (**a**) and local concentration in hyp8-11 (**b**). **c**, AP map of the *lin-14* mRNA level fold repression in wild-types compared to *lin-4(e912)* mutants. AP(%) indicate relative position along AP axis (0%-head, 100%-tail). The height of each bin is 1% and a moving average (bin; 36μm) is applied in x-direction. **d**, *lin-14* mRNA fold repression in the mid-body. Each curve represents trajectory along x-axis of the heat map in **c** where its corresponding color-bar is located. **e**-**f**, *lin-28* mRNA concentration dynamics of individual *lin-4(e912)* mutants as a function of body length. Overall concentration (**e**) and local concentration in hyp8-11 (**f**). Curves in **a**,**b**,**e** and **f** indicate moving averages (bin; 36μm). Dashed lines in **a**,**b**,**e** and **f** separate larval stages.

4.5 Synchronous expression of microRNA and its target dampens target gene expression fluctuations

To understand how the microRNA *lin-4* can eliminate the pulses of its targets' transcript levels, we compared the timing of the *lin-4* and *lin-14* peak expression. We found that the peaks of *lin-4* promoter activity (as quantified from Fig. 4.2c) coincide with the peaks of *lin-14* transcript levels in *lin-4(e912)* and *lin-14(n355gf)* animals (Fig. 4.4a). Given that the spatial expression patterns of *lin-4* and *lin-14* are similar and that *lin-4* acts cell autonomously [120], these results suggest that *lin-4* and its target *lin-14* are synchronously expressed by a pulsatile cue in individual cells.

Taken together, we suggest that the pulsatile transcript levels of *lin-14* and *lin-28* are effectively dampened by a synchronized pulsatile expression of their negative regulator *lin-4* in wild-type animals. The gene network motif composed of *lin-4* miRNA and its target *lin-14* can be classified as an "incoherent feed-forward loop (IFFL) [106]" (Fig.

4.4b). To quantitatively understand how a miRNA-mediated IFFL (miR-IFFL) motif can efficiently dampen target mRNA oscillations, we built a mathematical model to characterize the dynamics of target gene level in the presence of miRNA activity (Fig. 4.4b). We assumed a synchronous periodic production of the target mRNA and miRNA, with decays described by first-order constant rates γ_R and γ_m respectively. We also assumed irreversible second-order miRNA-mediated target transcript degradation kinetics with a rate constant k_{on}. The rate k_{on} depends on the strength of the miRNA-target interaction which is proportional to the number of miRNA complementary elements *N* of the target transcript (thus $k_{on}(N=0) = 0$ in both *lin-4(e912)* and *lin-14(n355gf)* strains). Target gene products were assumed to have no effect on the levels of itself (Supplementary Fig. 4.13). We assumed steady state dynamics and fitted this model to the experimental data (Supplementary Fig. 4.14). This simple model describes the experimental data well and, reassuringly, we found a linear correlation between k_{on} and the number *N* of *lin-4* complementary elements in the *lin-14* 3'-UTR (Fig. 4.4c).

To test the role of synchronous expression of the miRNA and its target, we explored the parameter space of the miR-IFFL as an insulator of pulsatile input signals using the model described above. We found that the relative fluctuations of *lin-14* mRNA levels are minimized only when the relative fluctuations of miRNA levels are non-zero and optimally balanced with the strength of miRNA-target interaction k_{on} (Fig. 4.4d, dark blue valley, 4.7 Supplementary Information). We find that wild-type animals operate closely to this optimal condition (Fig. 4.4d, Supplementary Fig. 4.15).

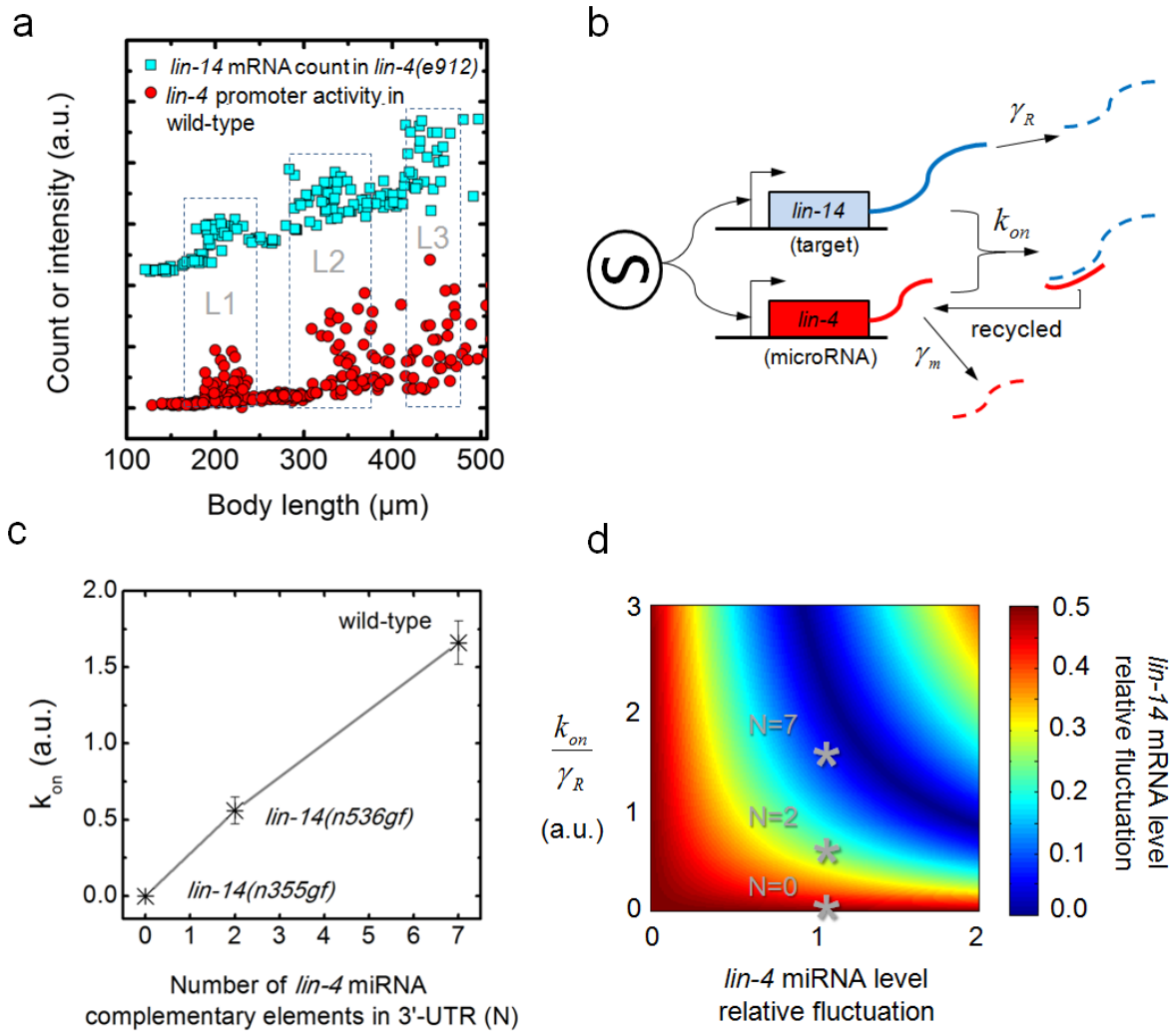

Figure 4.4 Synchronous expression of microRNA and its target dampens target gene expression fluctuations. **a**, Total fluorescence intensities of *Plin-4::gfp* smFISH probes in each animal and total number of *lin-14* mRNA in *lin-4(e912)* mutants oscillate in phase as a function of body length (dashed boxes). **b**, A biochemical model of miR-IFFL to describe target and miRNA level dynamics. The target mRNA and miRNA are coherently produced, and decay at constant rates γ_R and γ_m respectively. miRNA-mediated mRNA degradation occurs with rate $k_{on,}$, which is proportional to the number of LCE (N), and miRNA is recycled. **c**, k_{on} fit values for *lin-14* alleles with different N. Error bars, 95% CI. **d**, miR-IFFL performance landscape. Damping is efficient when

miRNA is expressed synchronously to its target (*lin-4* miRNA relative fluctuation > 0) with an optimal value of k_{on} (dark blue valley). Asterisks indicate strains with different *N*.

4.6 Conclusion

While previously only a handful of genes were shown to peak during each larval stage [34,108–110,121,122] we found that the majority of the *C. elegans* transcriptome is highly dynamic. Using quantitative whole genome dynamic measurements we demonstrated that thousands of genes are periodically expressed during post-embryonic development, suggesting that oscillating transcript levels are the norm rather than the exception. This suggests that the global physiology of the worm is likely to vary periodically, driven by the molting cycles. However if the majority of the transcriptome is oscillating how are transcripts that need to define temporal gradients insulated from these global oscillations? Here we show that microRNA-mediated feed-forward loops actively insulate temporal-gradient genes from these global oscillations even if the promoter activity of the miRNA and its target are driven by a global periodic signal. We suggest that a miRNA-mediated incoherent feed-forward loop [106] could be a simple but powerful design motif that dynamic gene regulatory networks of multi-cellular organisms can adopt to insulate genes from highly dynamic but undesired inputs. Consistent with this speculation, we found an overrepresented enrichment of predicted targets of conserved *C. elegans* miRNAs [123] in the graded class (Supplementary Fig. 4.16). Given its prevalence throughout different species [124] this design motif might serve similar function in other species [125].

4.7 Supplementary Information

Determining periodicities from auto correlation analysis

Among the original RPKM time series $x_0, x_1, x_2, \cdots, x_{N-2}, x_{N-1}$ (total N=20 time points for wild-type animals cultured in 20°C or 25°C, and N=25 for *lin-4(e912)* animals cultured in 20°C) of each transcript species, we excluded the first four time points x_0, x_1, x_2, x_3 to avoid any developmental lag period that might occur due to L1 arrest. We then normalized the scale of RPKM dynamics by transforming the time series into Z-scores, $z_i = (x_i - < x >) / \Delta x$, where $< x >$ and Δx are the mean and standard deviation of RPKM time series respectively. Using these Z-scores, we calculated the auto correlation coefficient *AC(L)* at lag L defined as

$$AC(L) = \frac{\sum_{i=4}^{i=N-1}(z_i - < z >)(z_{i+L} - < z >)}{\sum_{i=4}^{i=N-1}(z_i - < z >)^2}$$

$<z>$ is the mean of the Z-score time series $z_4, z_5, z_6, \cdots, z_{N-2}, z_{N-1}$. Whenever $i+L>N-1$, the series was considered to be zero. The period T for this given species was determined by $T=2L_{max}$, where *AC(L)* forms an upward-convex peak at $L=L_{max}$. The p-values of this peak for each transcript species was obtained by performing 1,000 repeated trials using randomly permuted time series. Only the transcript species exhibiting peaks with $p<0.05$ were considered periodic.

Classification of expression dynamics from cross correlation analysis

For each transcript species, we calculated the cross correlation coefficient CCC_{TP} between the Z-score time series and ideal cosine curves of period T = T_1, T = T_2, and T = T_3 respectively.

$$CCC_{TP} = \frac{\sum_{i=3}^{i=N-1}(z_i - < z >)\left(y_i^{T,P} - < y >\right)}{\sqrt{\sum_{i=3}^{i=N-1}(z_i - < z >)^2}\sqrt{\sum_{i=3}^{i=N-1}\left(y_i^{T,P} - < y >\right)^2}}$$

$y_i^{T,P} = cos\{\frac{2\pi}{T} \cdot (t_i - \frac{T \cdot P}{\beta})\}$ represents an ideal cosine series of period *T* and phase *P* (in units of hrs). t_i is the time data point z_i was collected (in units of hrs). For each *T*, *ß* different *P*s (running from 1hrs to *ß* hrs) were tested and the maximum among the *ß* was assigned as CCC_{TP}. In addition, the Z-score time series was fitted to a line using the sum of least square method. The cross correlation coefficient CCL_s between the Z-score time series and this line of slope s was calculated. Thus for each given transcript species, CCC_{T1P}, CCC_{T2P}, CCC_{T3P} *and* CCL_s were obtained. The p-values of each correlation coefficient were then obtained by performing 1,000 repeated trials of cross correlation coefficient computations using randomly permuted time series. We retained p-values that were deemed significant using a false discovery rate of 0.1 computed for the pooled set of p-values for all four classes. Each transcript species was assigned to one of the four classes which gave the lowest significant p-value. Transcript species with no significant p-value from any of the four classes were not classified into either of them.

	N	T_1	T_2	T_3	*ß*
Wild-type (20°C)	20	12	24	36	36
Wild-type (25°C)	20	9	16.5	24	32

Analytical understanding of the miR-IFFL performance

To test the role of synchronous expression of the miRNA and its target, we investigated the performance of the miR-IFFL as a damper of pulsatile gene expression using the model described in Supplementary Fig. 4.14. The performance of mIFFL is defined as $\delta u/u_{min}$, where δu is the peak height and u_{min} is the basal level of dampened target mRNA. We explore how this performance changes as a function of k_{on} and the relative amplitude of the miRNA fluctuations $\delta m/m_{min}$. We found that the best performance, or $\delta u/u_{min}$=0 (no fluctuations in $u(t)$), is achieved when the height of miRNA peak δm was non-zero and the strength of miRNA-target interaction k_{on} was optimally balanced (Fig. 4.4d, dark blue valley). We find that wild-type animals (N=7) operate closely to this optimal condition (Fig. 4.4d).

What is the advantage of having miRNA synchronously expressed with its target for dampening cyclic target gene expression fluctuations? From Eqn. [2] (Supplementary Fig. 4.14), we calculate the differential of $u_{st}(t)$

$$\Delta u_{st} = u_{st}(t) \cdot \left[\frac{\Delta k_R}{k_R(t)} - \left(\frac{\alpha \cdot m(t)}{1+\alpha \cdot m(t)} \right) \cdot \frac{\Delta m}{m(t)} \right]$$

$$\frac{\Delta u_{st}}{u_{st}(t)} = \left[\frac{\Delta k_R}{k_R(t)} - \left(\frac{\alpha \cdot m(t)}{1+\alpha \cdot m(t)} \right) \cdot \frac{\Delta m}{m(t)} \right]$$

$$G\left(u_{st}(t)\right) = G\left(k_R(t)\right) - \left(\frac{\alpha \cdot m(t)}{1+\alpha \cdot m(t)} \right) \cdot G\left(m(t)\right) \qquad [1]$$

where G denotes the relative rate of change, or logarithmic gain [126]. Note that $G\left(u_{st}(t)\right)$ is equal to the difference between $G\left(k_R(t)\right)$ and $G\left(m(t)\right)$ weighted by a function, which depends on $\alpha \cdot m(t)$. For the sake of simplicity, we will consider small

relative changes so that we can let $\frac{\delta u}{u_{\min}} \approx \frac{\Delta u_{st}}{u_{st}(t)}$, $\frac{\delta k_R}{k_{R\min}} \approx \frac{\Delta k_R}{k_R(t)}$, and $\frac{\delta m}{m_{\min}} \approx \frac{\Delta m}{m(t)}$. As we see from Eqn. [1], in the case of a miR-IFFL where the miRNA is synchronously expressed with its target, $\frac{\delta k_R}{k_{R\min}}$ and $\frac{\delta m}{m_{\min}}$ carry the same signs and thus $\frac{\delta m}{m_{\min}}$ acts to cancel out the change that occurs to $\frac{\delta k_R}{k_{R\min}}$. This results in a reduced $\frac{\delta u}{u_{\min}}$ at all times. This becomes optimal when $\alpha \equiv \frac{k_{on}}{\gamma_R}$ carries a particular value. When this value is below the optimum, the performance falls in sub-optimal space which is lower left of the parameter space in Fig. 4.4d, because the miRNA efficacy is not strong enough to completely eliminate the target level peaks. On the other hand, when this value is above the optimum, the performance falls in upper right part of the parameter space in Fig. 4.4d. This seemingly counterintuitive case occurs when there is an “excess” damping where a miRNA pulse not only eliminates the target level peak but also creates a trough due to a strong repression, effectively generating a cyclic target expression level fluctuation with a 180^o phase shift (Supplementary Fig. 4.15). Interestingly, regardless of what $\alpha \equiv \frac{k_{on}}{\gamma_R}$ is, when miRNA expression is constitutive ($\Delta m = 0$), $\frac{\delta u}{u_{\min}}$ is not reduced (no damping).

a

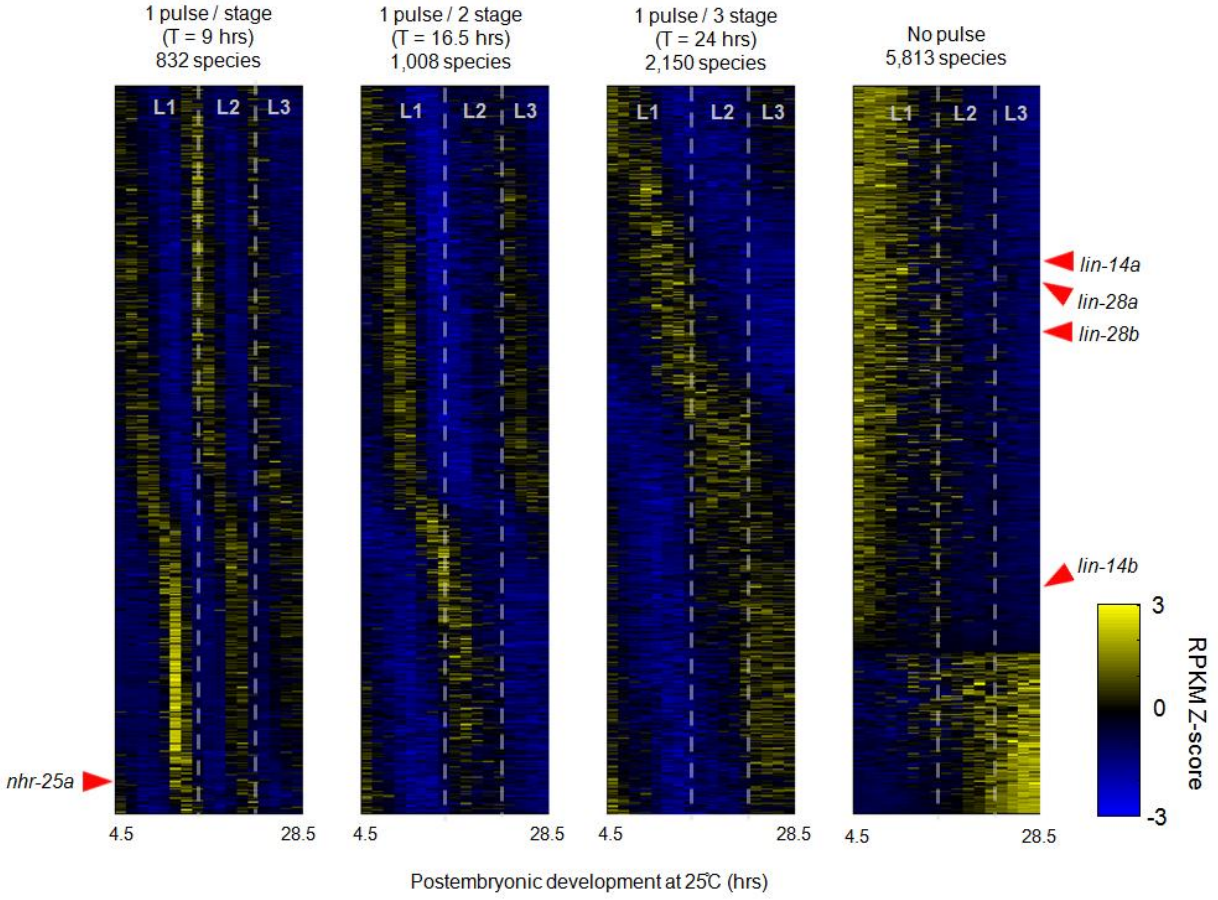
1 pulse / stage
(T = 9 hrs)
832 species
1 pulse / 2 stage
(T = 16.5 hrs)
1,008 species
1 pulse / 3 stage
(T = 24 hrs)
2,150 species
No pulse
5,813 species
L1
L2
L3
4.5
28.5
nhr-25a
lin-14a
lin-28a
lin-28b
lin-14b
3
0
-3
RPKM Z-score
Postembryonic development at 25℃ (hrs)

b

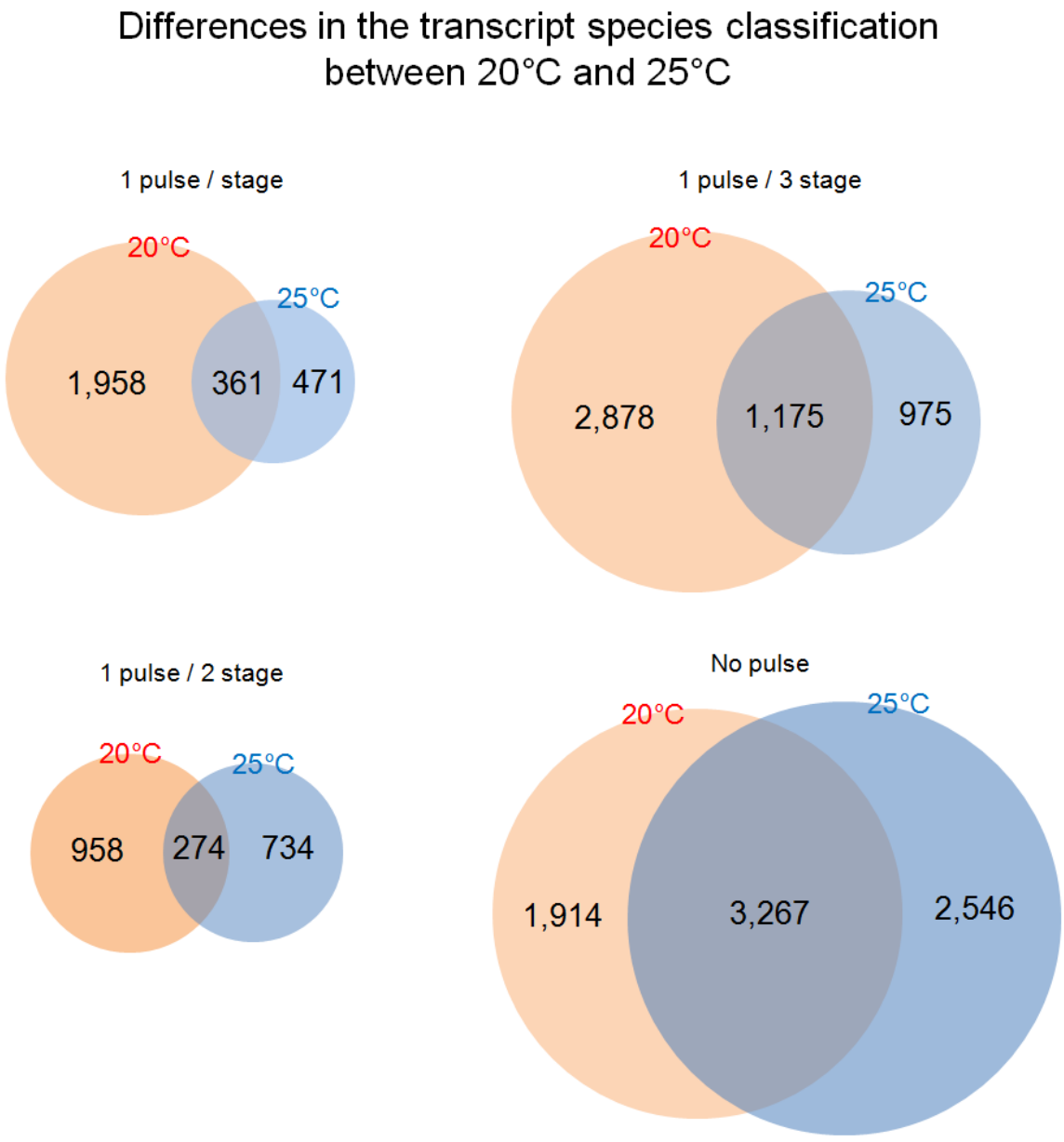
Differences in the transcript species classification between 20°C and 25°C
1 pulse / stage
20°C
25°C
1,958
361
471
1 pulse / 3 stage
20°C
25°C
2,878
1,175
975
1 pulse / 2 stage
20°C
25°C
958
274
734
No pulse
20°C
25°C
1,914
3,267
2,546

Supplementary Figure 4.1: Majority of the *C. elegans* transcriptome displays pulsatile dynamics during larval development at 25°C. a, Classification of transcript species into four dynamical groups at 25°C. Each column is ordered in phase. Scale bar indicates Z-scores of RPKM. Species with significant p-values are shown (false discovery rate 0.1). Red arrowheads indicate locations of the specified transcript species. Dashed lines separate larval stages. When the temperature was shifted to 25°C, we were no longer able to classify *lin-42*, *dpy-5* and *dpy-10* genes in the T = 9 hrs (1 pulse / 1 stage) group. We believe that this is due to our stringent criteria of the cross correlation analyses we used for periodic gene screening (4.7 Supplementary Information). Indeed, we see a number of genes which are definitely oscillatory (*e.g.*, molting genes) not being picked up in our periodic groups – the baseline expression level of these genes often changes significantly over time, and the timing of their transcript level pulses are coordinated with larval stages which make these genes no longer ideally periodic. **b**, Venn diagrams illustrating how the classifications of transcript species at 20°C (Fig. 4.1e) and 25°C overlap. The numbers in the overlapping shaded areas (in gray) indicate the number of transcript species that are classified into the same dynamical group at both temperatures in our analysis described in the 4.7 Supplementary Information.

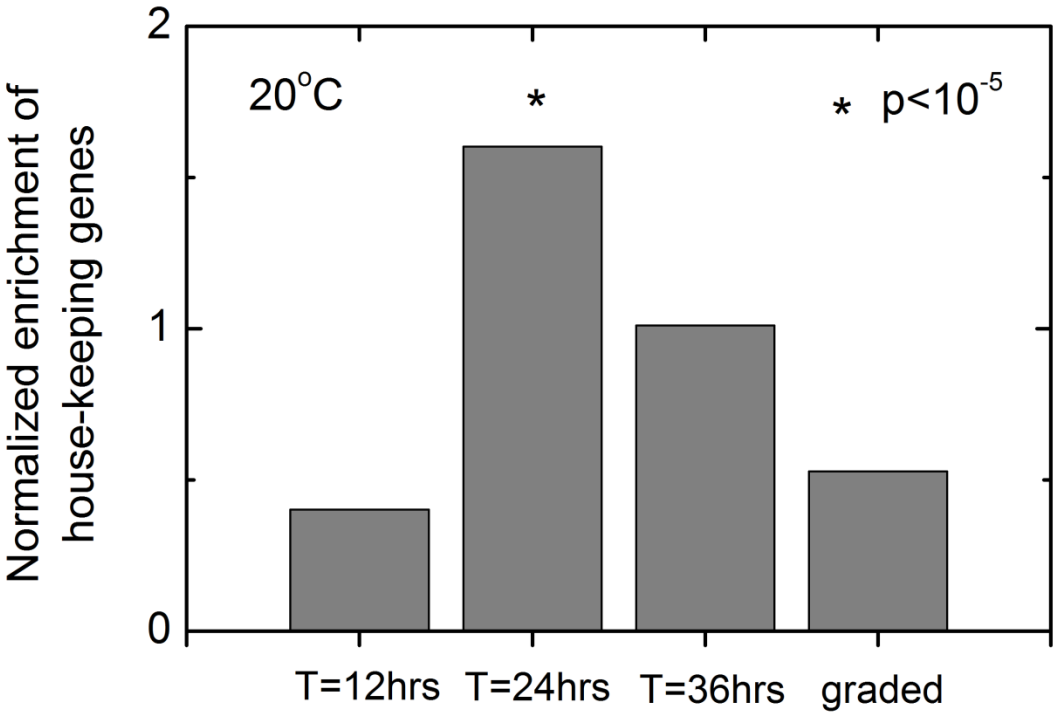
Normalized enrichment of house-keeping genes
20°C
*
* p<10-5
2
1
0
T=12hrs
T=24hrs
T=36hrs
graded

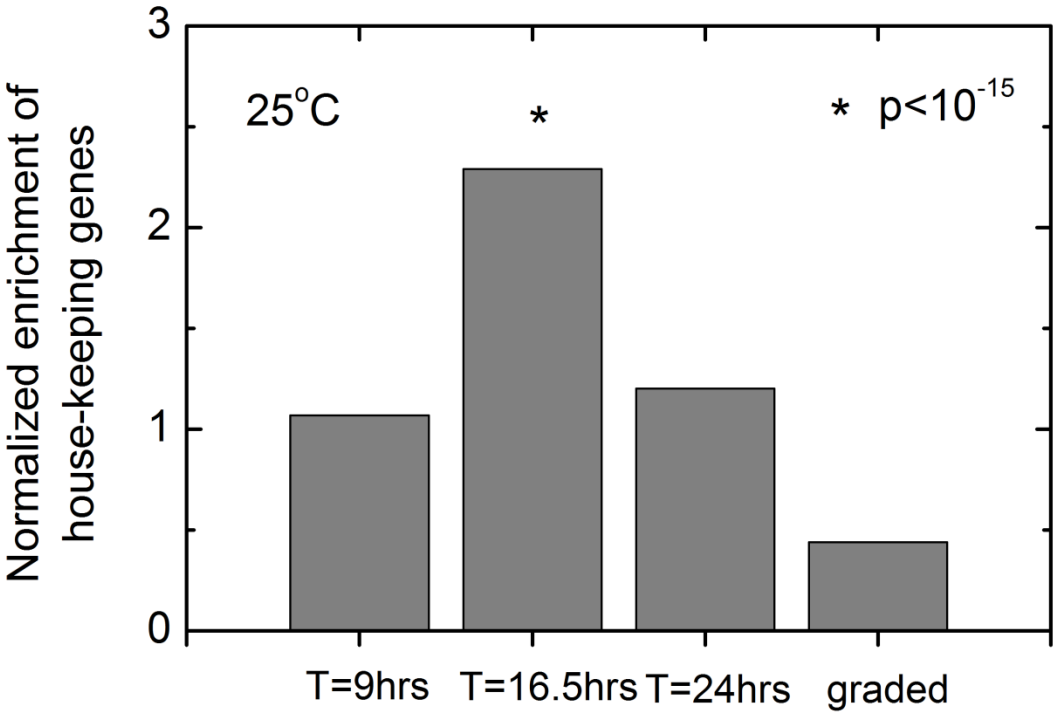
Normalized enrichment of house-keeping genes
25°C
*
* p<10-15
3
2
1
0
T=9hrs
T=16.5hrs
T=24hrs
graded

Supplementary Figure 4.2: House-keeping genes are overrepresented in the pulsatile class. We found that house-keeping genes are significantly enriched in dynamical groups that exhibit temporal fluctuations. We used the list of 554 essential sterile genes [127] screened from Sönnichsen *et al.*, 2005 to find out how the four classes were enriched with these essential genes. “Normalized enrichment” of each class was calculated as the ratio of the fraction of house-keeping genes in a given class to the fraction of house-keeping gene in the entire genome. Thus “Normalized enrichment of 1” indicates the degree of enrichment of a certain dynamical group by any random gene. The p-values were computed from hypergeometric probability distributions. We find that at both 20°C (top panel) and 25°C (bottom panel), house-keeping genes are significantly overrepresented in the “1 pulse / 2 stage” class.

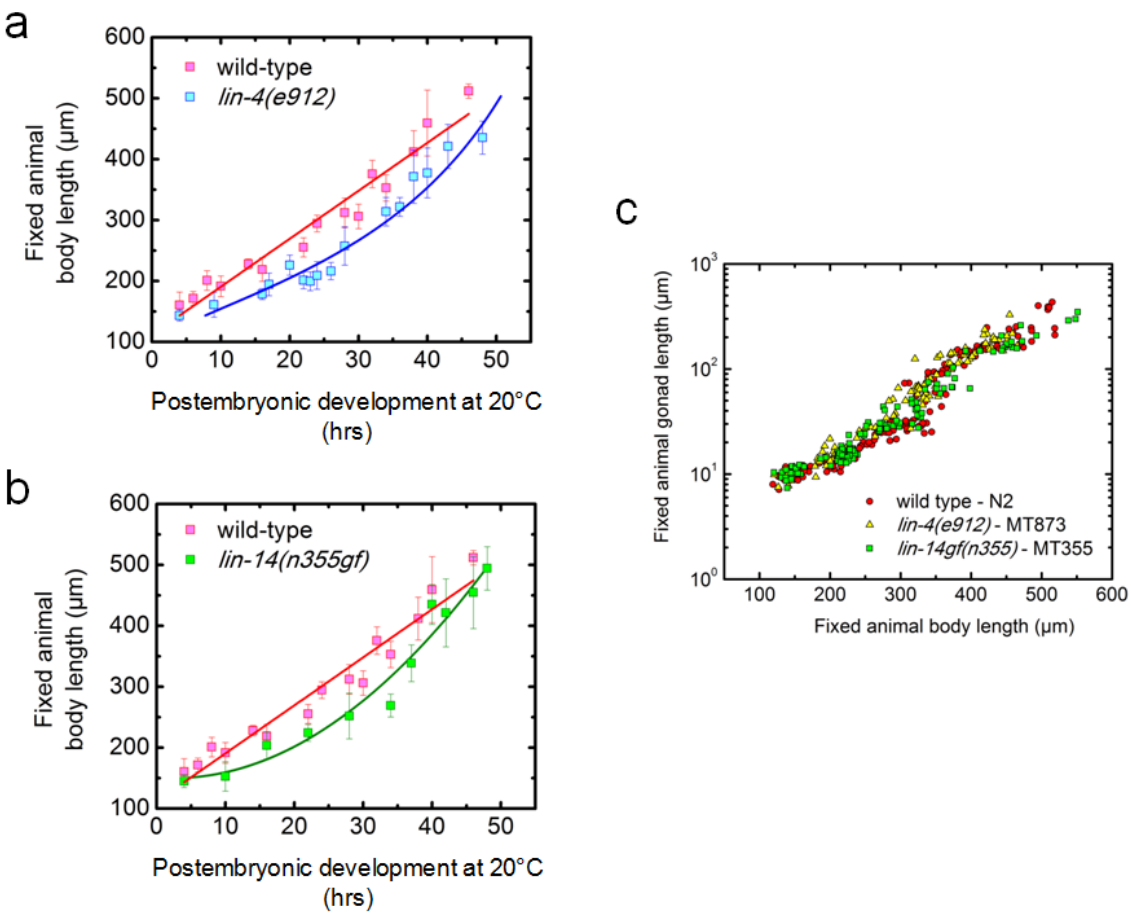

Supplementary Figure 4.3: Body length as a developmental age indicator. We found animal body length to be a robust developmental age indicator. **a**-**b**, We sampled the body lengths of animals grown on OP50 in 20°C from differently synchronized batches. Animals were synchronized by hypochlorite treatment. Body lengths of wild-types were overall longer than *lin-4(e912)* (**a**) and *lin-14(n355gf)* (**b**) mutants of the same developmental time, presumably because wild-types have higher growth rates [43]. We fitted these data to lines or curves to convert body lengths of different strains into developmental times. Note that we have used a linear correlation between body length and developmental time for wild-types to simplify our data analysis throughout this work (Supplementary Fig. 4.6). Error bars, s.d.; n > 10. **c**, Because the germ line and gonad of *lin-4* and/or *lin-14gf* mutant animals maturate at similar rates as wild-types [43] and since (2) we found gonad length (distance between the two distal tip

cells along the gonad arms) and body length of an animal to be identically correlated in wild-types, *lin-4* and *lin-14gf* mutants, we considered animals of the same body length to be at identical developmental age regardless of the mutation.

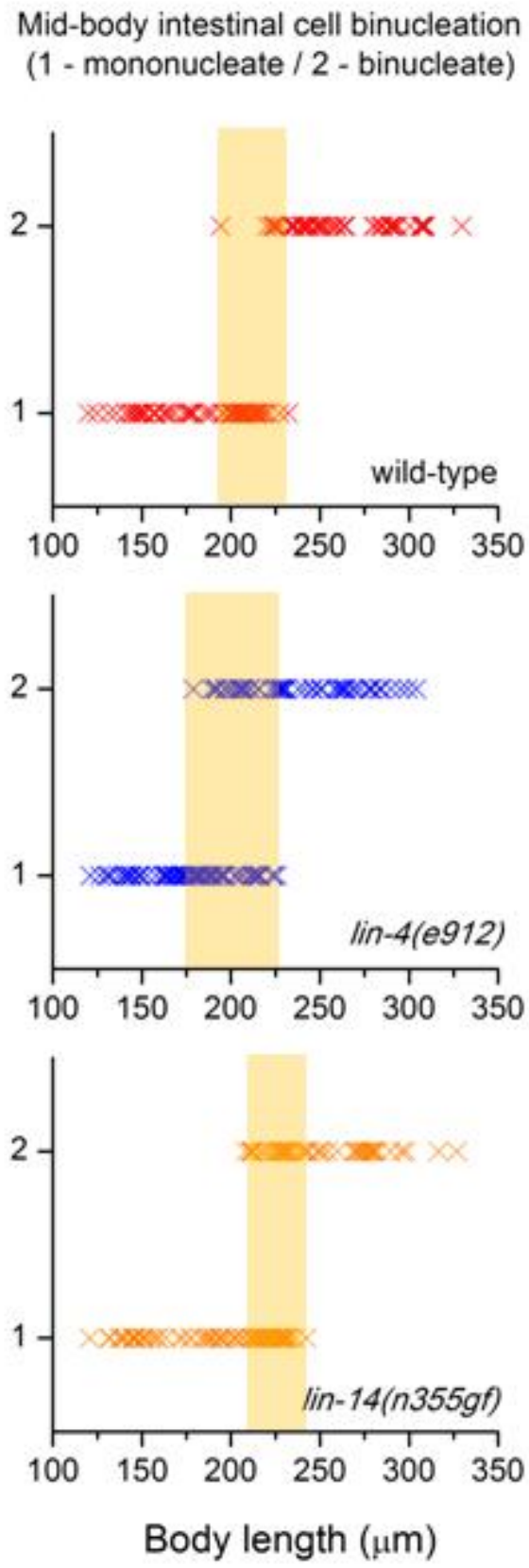
Mid-body intestinal cell binucleation
(1 - mononucleate / 2 - binucleate)
2
1
wild-type
100
150
200
250
300
350
2
1
lin-4(e912)
100
150
200
250
300
350
2
1
lin-14(n355gf)
100
150
200
250
300
350
Body length (μm)

Supplementary Figure 4.4: The timing of binucleation of intestinal cells correlates with a range of animal body lengths. Intestinal nuclei in the mid-body region divide without cell division at the beginning of the lethargus prior to the first molt, which makes this binucleation event a useful developmental landmark for determining the age of an early stage animal [128]. When the nuclei are stained with DAPI, binucleated intestinal cells are clearly distinguishable from mononucleated cells. We fixed and stained wild-type, *lin-4(e912)* and *lin-14(n355gf)* animals with DAPI and simultaneously determined the nuclear state of intestinal cells and body length of individual animals, to test whether animal body length can be used as a proxy for early developmental ages. We found that intestinal binucleation occurs at the body length range (shaded in yellow) of 190µm~225µm in wild-types and 175µm~225µm in *lin-4(e912)* animals. In *lin-14(n355gf)* animals, this was shifted to 200µm~250µm which is consistent with the overall shift of *lin-14* mRNA expression dynamics compared to that of *lin-4(e912)* animals (Fig. 4.3a and Supplementary Fig. 4.11). Therefore, we can distinguish animals of at least three distinct developmental age groups within L1 stage based on body lengths – for instance, “before (<175µm)”, “during (>175µm and <225µm)”, and “after (>225µm)” intestinal binucleation of *lin-4(e912)* mutants in L1 stage. We can use this information to further support our conclusion from Fig. 4.3a that *lin-14* mRNA expression levels are temporally “pulsatile”, because the *lin-14* mRNA levels of animals “before” and “after” intestinal binucleation are clearly distinct from that of animals “during” intestinal binucleation (Fig. 4.3a).

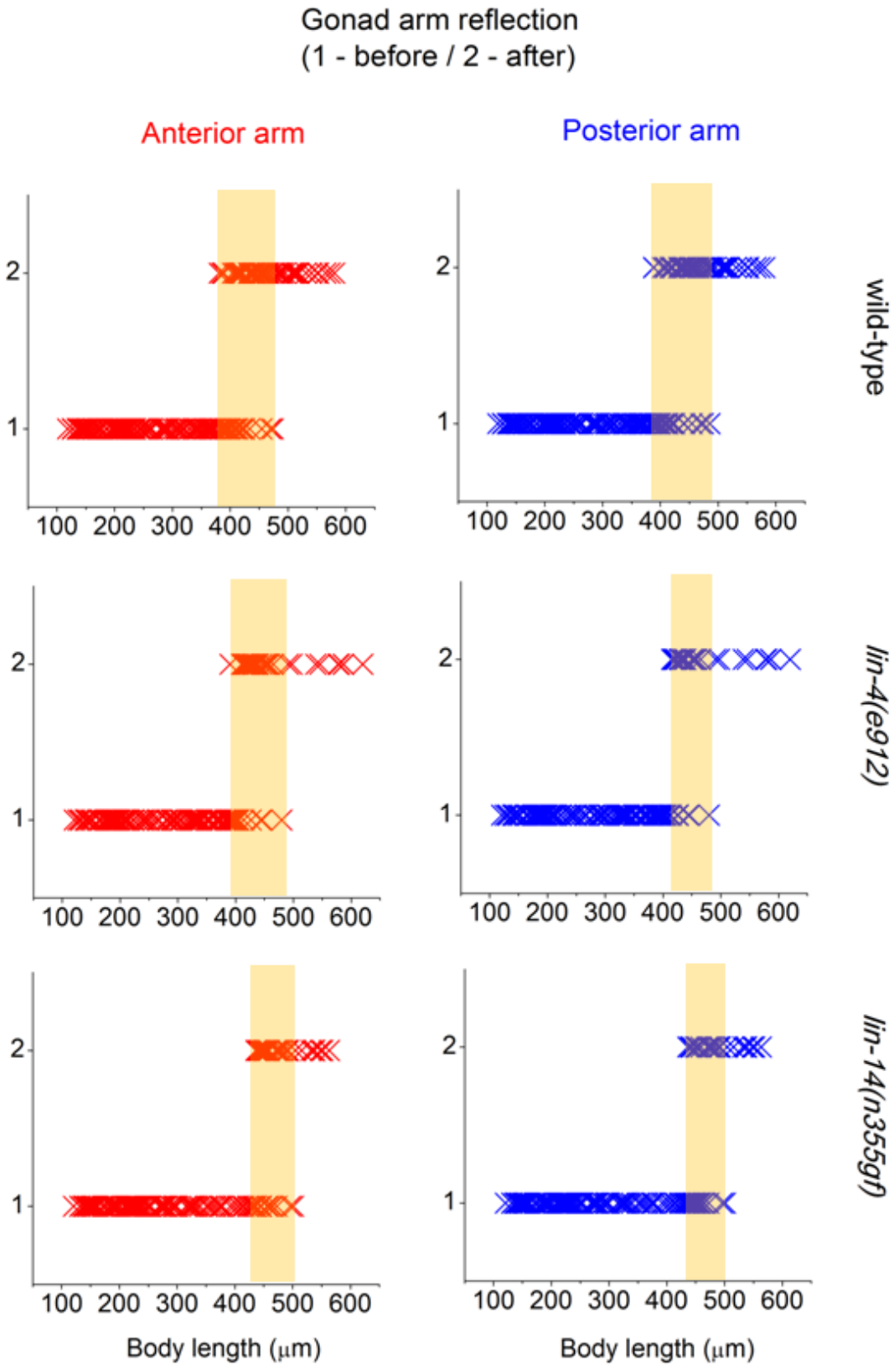
Gonad arm reflection
(1 - before / 2 - after)
Anterior arm
Posterior arm
wild-type
lin-4(e912)
lin-14(n355gf)
2
1
100 200 300 400 500 600
Body length (μm)

Supplementary Figure 4.5: The timing of gonad arm reflection correlates with animal body length. During postembryonic development, the anterior and posterior gonad arms elongate with the two distal tip cells located at the distal ends of the arms migrating away from each other. Around late L3 and L3 molt, both arms make reflecting turns and elongate towards each other [129]. Since *lin-4* and *lin-14* do not have any effect on their development, gonad arm reflection is a useful developmental landmark for determining the age of a later stage animal. We fixed and stained wild-type, *lin-4(e912)* and *lin-14(n355gf)* animals with DAPI and simultaneously determined the gonad arm morphology and body length of individual animals, to again test whether animal body length can be used as a proxy for late developmental ages. We found that gonad arm reflection occurs at the body length range (shaded in yellow) of 390µm~475µm in wild-types and 400µm~475µm in *lin-4(e912)* animals. In *lin-14(n355gf)* animals, this was shifted to 440µm~500µm which is consistent with the overall shift of *lin-14* mRNA expression dynamics compared to that of *lin-4(e912)* animals (Fig. 4.3a and Supplementary Fig. 4.11). Therefore, we can distinguish animals of at early, late L3 and early L4 stages based on body lengths.

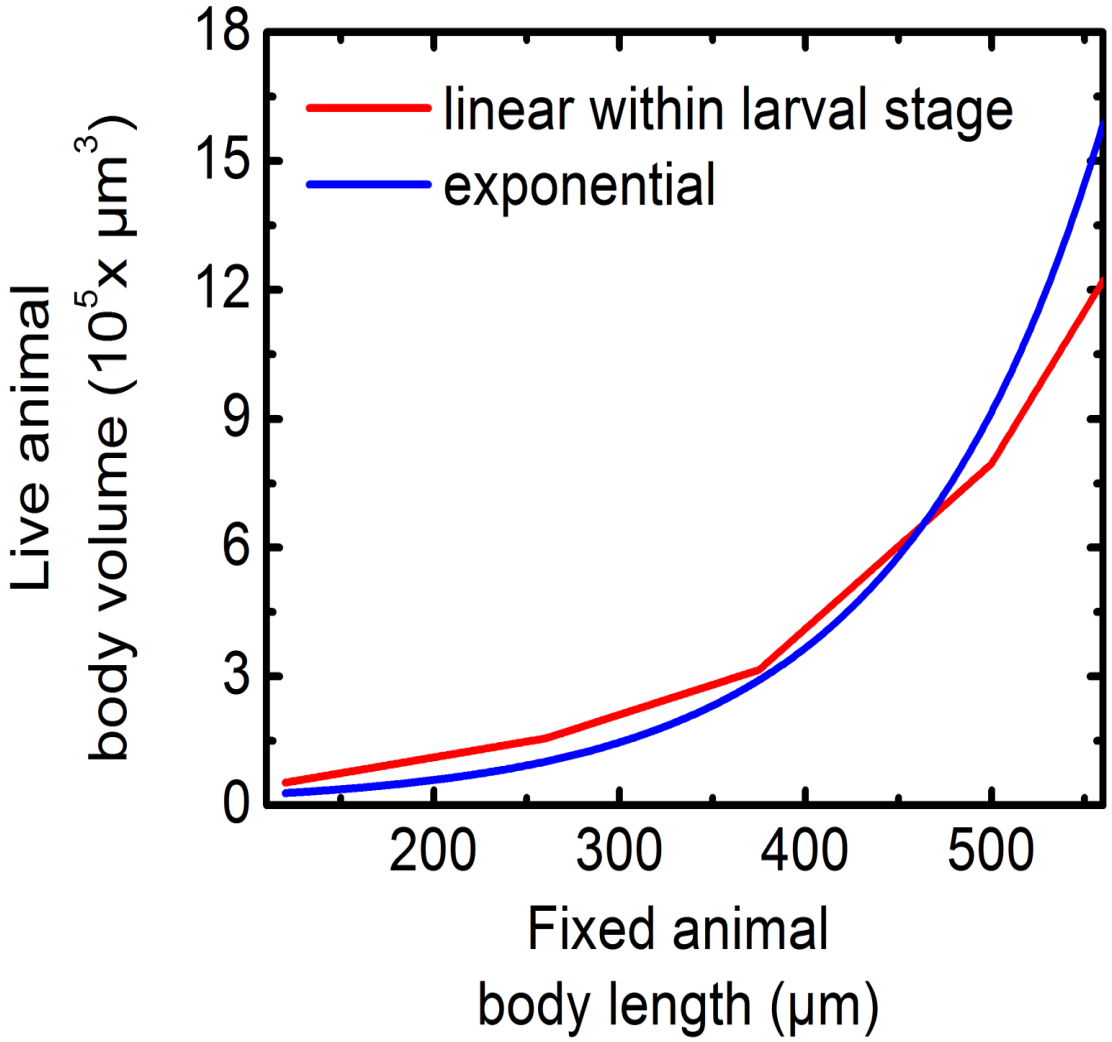

Supplementary Figure 4.6: Live animal body volume as a function of fixed animal body length. We used live wild-type animal volume data from Knight *et al*., 2002 [117] to calculate *lin-14* mRNA concentration during post-embryonic development of *C. elegans*. Because the growth rates of L1-arrested synchronized animals are different from that of freely growing animals, we could not directly adopt the published result V=46.6*exp(0.0722*t) (V, in $\mu m^3 x 10^3$ and t, in hrs). To correct for this, we first constructed a piecewise linear volume growth curve as a function of body length (red) using the larval stage specific constant growth rates described in Knight *et al*.,

2002 [117]. Given the linear correlation between body length and developmental time of wild-types (Supplementary Fig. 4.3), we were able to draw straight lines with constant slopes (growth rates) for each larval stage. Body lengths at which each larval stage transition occurred were estimated from collagen coding gene mRNA expressions. In our study, we used an exponential curve (blue) that fits well to the piecewise linear curve (red) to calculate *lin-14* mRNA concentration of each animal of a particular body length. The equation describing the blue curve is V=46.6 * exp(((8*L-893.2)/873.5)-0.578) (V, in $\mu m^3 x10^3$ and L in µm). We assumed animals with identical body length to have identical body volume regardless of the mutant background used in our study. We found the volume of the group of cells hyp8-11 in hatchlings to be roughly similar to that of a typical seam cell at the same developmental age. Thus, for hyp-8-11 volume as a function of body length, we used V=0.2138*exp(((8*L-893.22531)/873.539889)-0.5776) (V, in $\mu m^3 x10^3$ and L in µm).

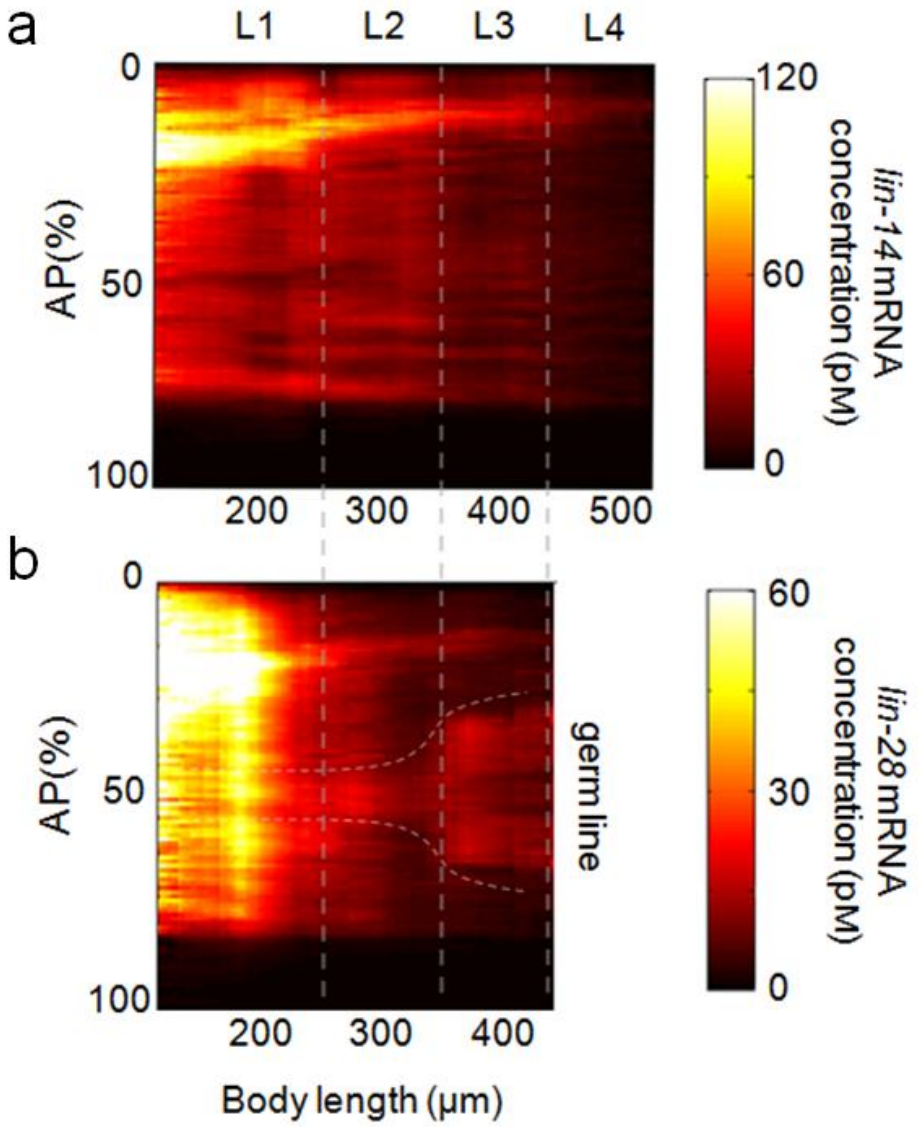

Supplementary Figure 4.7: AP mRNA concentration map for *lin-14* (a) and *lin-28* (b). AP(%) indicate relative position along AP axis (0%-head, 100%-tail). The height of each bin is 1% and a moving average (bin; 36μm) is applied in x-direction.

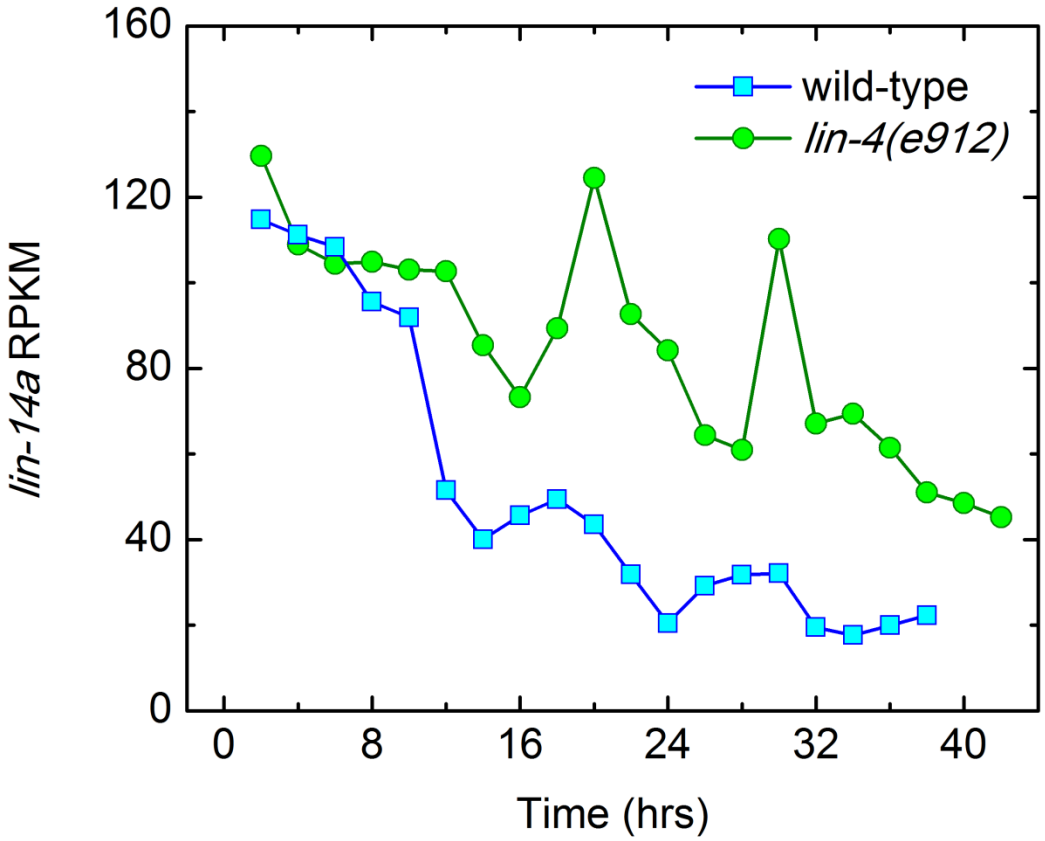

Supplementary Figure 4.8: RPKM dynamics of *lin-14a* in *lin-4(e912)* KO animals is pulsatile. We found *lin-14* transcript levels of *lin-4(e912)* KO animals peaking at t = 20 hrs and t = 30 hrs of postembryonic development from our RNA-Seq experiment.

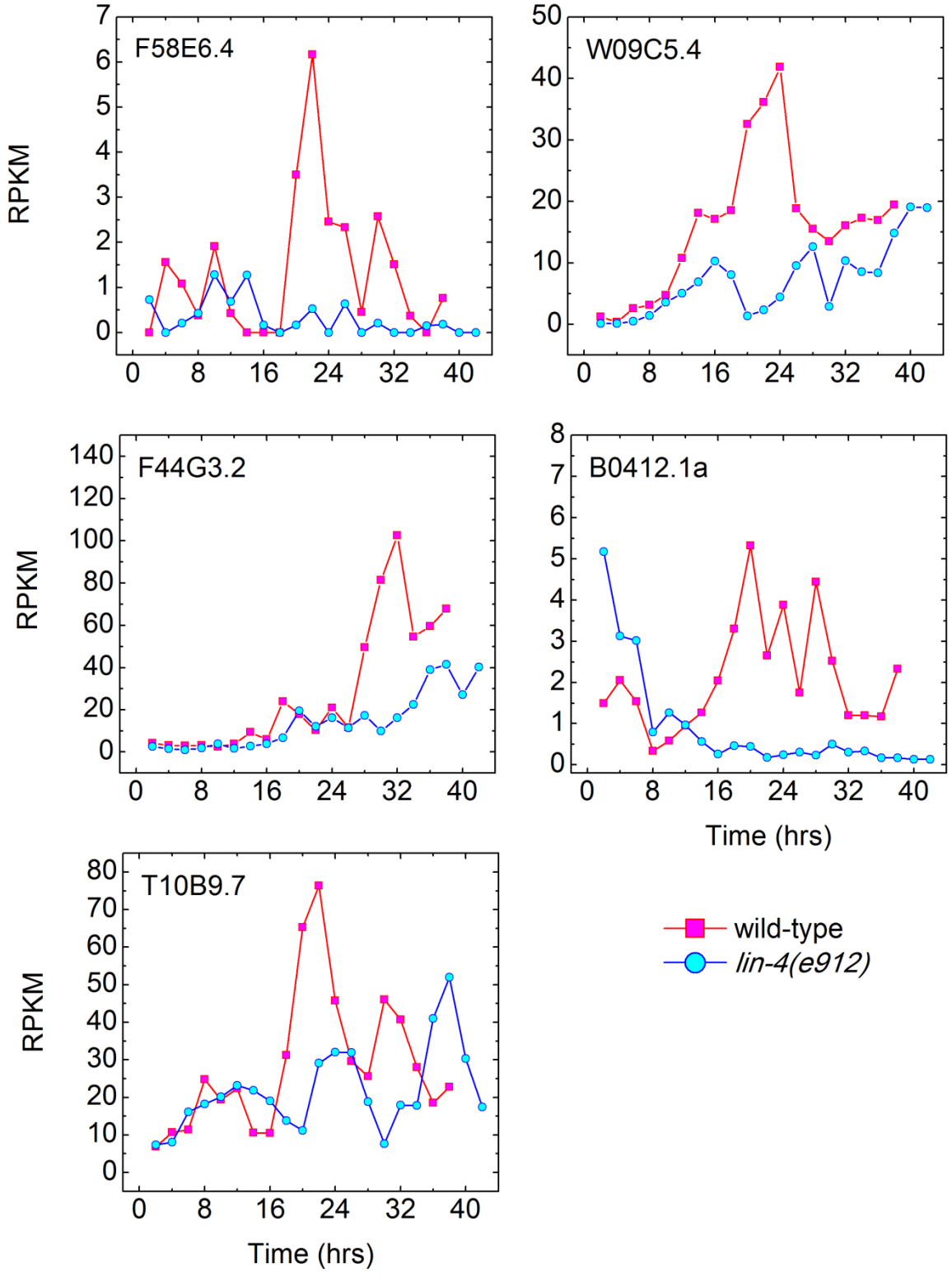
F58E6.4
W09C5.4
F44G3.2
B0412.1a
T10B9.7
RPKM
RPKM
RPKM
Time (hrs)
Time (hrs)
wild-type
lin-4(e912)

Supplementary Figure 4.9: Pulsatile transcript levels of the putative negatively regulated downstream genes of LIN-14 are eliminated in the absence of *lin-4* miRNA activity. A list of candidate LIN-14 target genes [130] was reported in the study by Hristova *et al.*, 2005. Among the best candidates whose mRNA levels changed in a complementary fashion in *lin-14* and *lin-4* mutants, were 5 genes of “class D” which were elevated in the *lin-14(n179ts)* loss-of-function mutant and reduced in the *lin-4(e912)* knock-out mutant. We compared the transcript levels of these genes in wild-types and *lin-4* mutants from our RNA-Seq data. In wild-types, the transcript levels of all 5 “class D” genes exhibited at least one or two pulses and each pulse occurred at times when *lin-4* miRNA levels peaked (Fig. 4.2a). However, the pulses of “class D” genes were mostly eliminated in *lin-4* mutants. Note that a phase shift in time (a ~4hrs delay in *lin-4* mutants) of due to the difference in their growth rates [43] must be taken into account for direct comparison between strains. We interpret such transcriptional repression of LIN-14 target genes to be predominant at times when transcript levels of *lin-14* peak in this mutant. These results suggest that the protein levels of *lin-14* peak as well as its transcript levels during larval development of *lin-4* mutants.

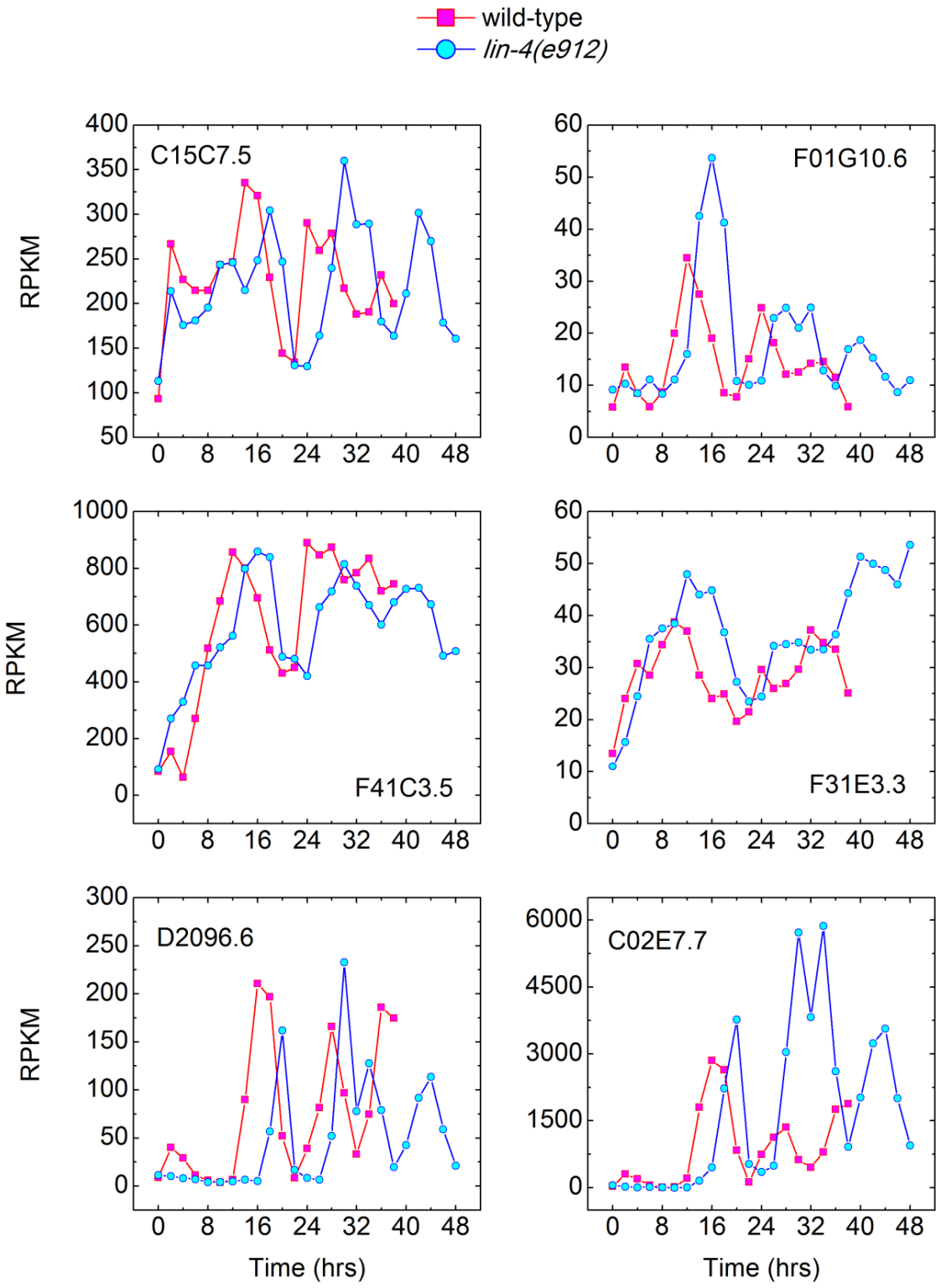
wild-type
lin-4(e912)
C15C7.5
F01G10.6
F41C3.5
F31E3.3
D2096.6
C02E7.7
RPKM
RPKM
RPKM
Time (hrs)
Time (hrs)

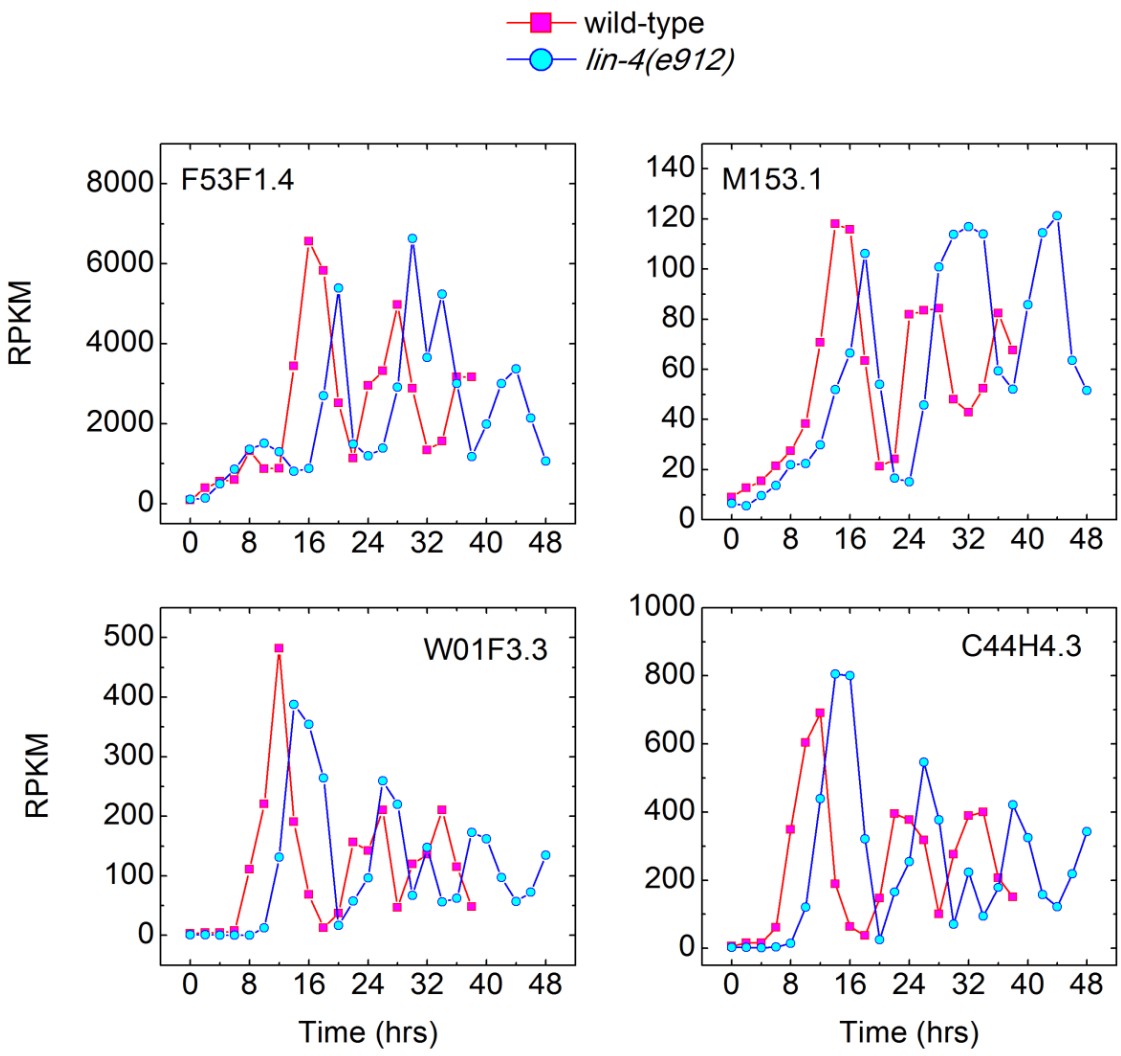

Supplementary Figure 4.10: Pulsatile transcript levels of the putative positively regulated downstream genes of LIN-14 are mostly unaffected in the absence of *lin-4* miRNA activity. mRNA levels of genes of "class C" reported in the study by Hristova *et al.*, 2005 were reduced in the *lin-14(n179ts)* loss-of-function mutant and elevated in the *lin-4(e912)* knock-out mutant. We compared the transcript levels of these genes in wild-types and *lin-4* mutants from our RNA-Seq data. In both strains, the transcript levels of "class C" genes exhibited similar pulsatile expression dynamics with a phase shift in time due to the difference in their growth rates [43]. We found that the mRNA levels of most "class C" genes are not significantly altered the *lin-4* mutants. The

only exception was the second peak of C02E7.7 which was significantly amplified in *lin-4* mutants at t=30~34hrs. We interpret such transcriptional activation of LIN-14 target genes, if any, to be predominant at times when transcript levels of *lin-14* peak in this mutant. These results support our conclusion that the protein levels of *lin-14* peak as well as its transcript levels during larval development of *lin-4* mutants.

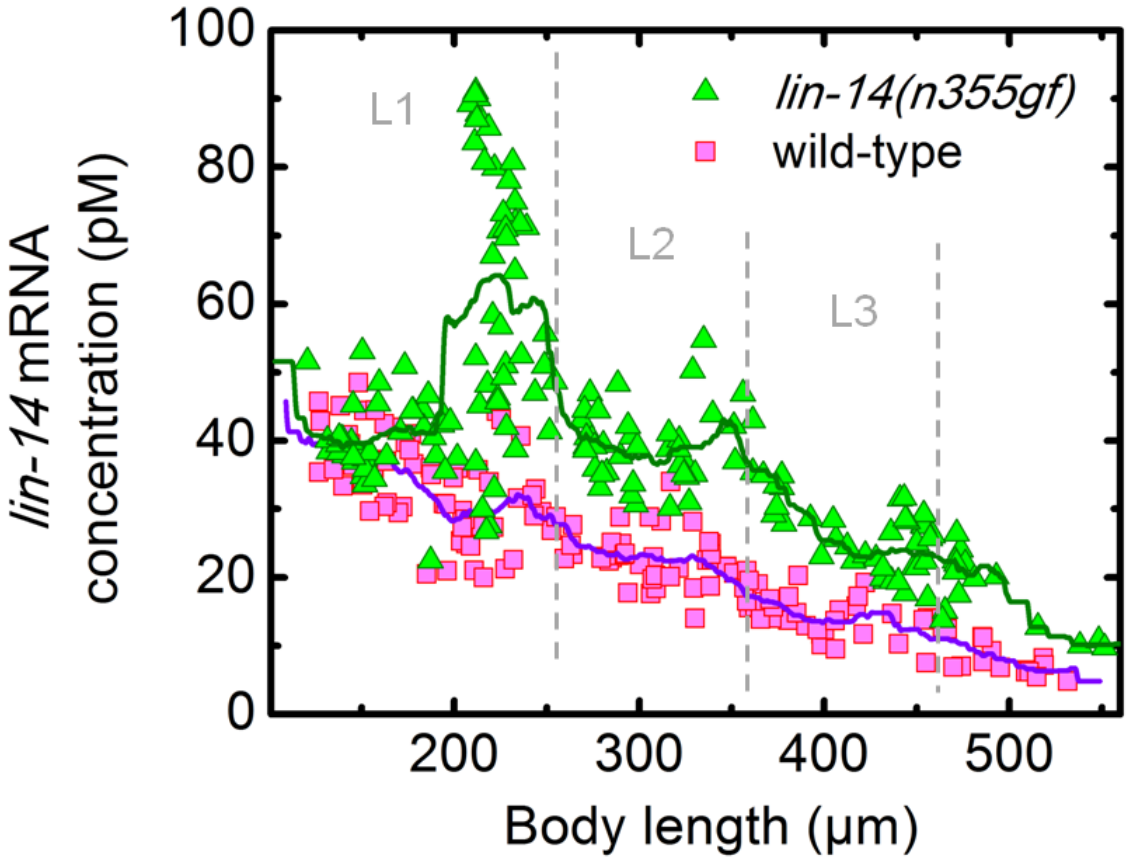

Supplementary Figure 4.11: *lin-14* mRNA expression in *lin-14(n355gf)* mutants. Curves indicate simple moving averages of the corresponding data points within a bin of size 36 μm. Wild-type data were shown for comparison. Dashed lines separate larval stages.

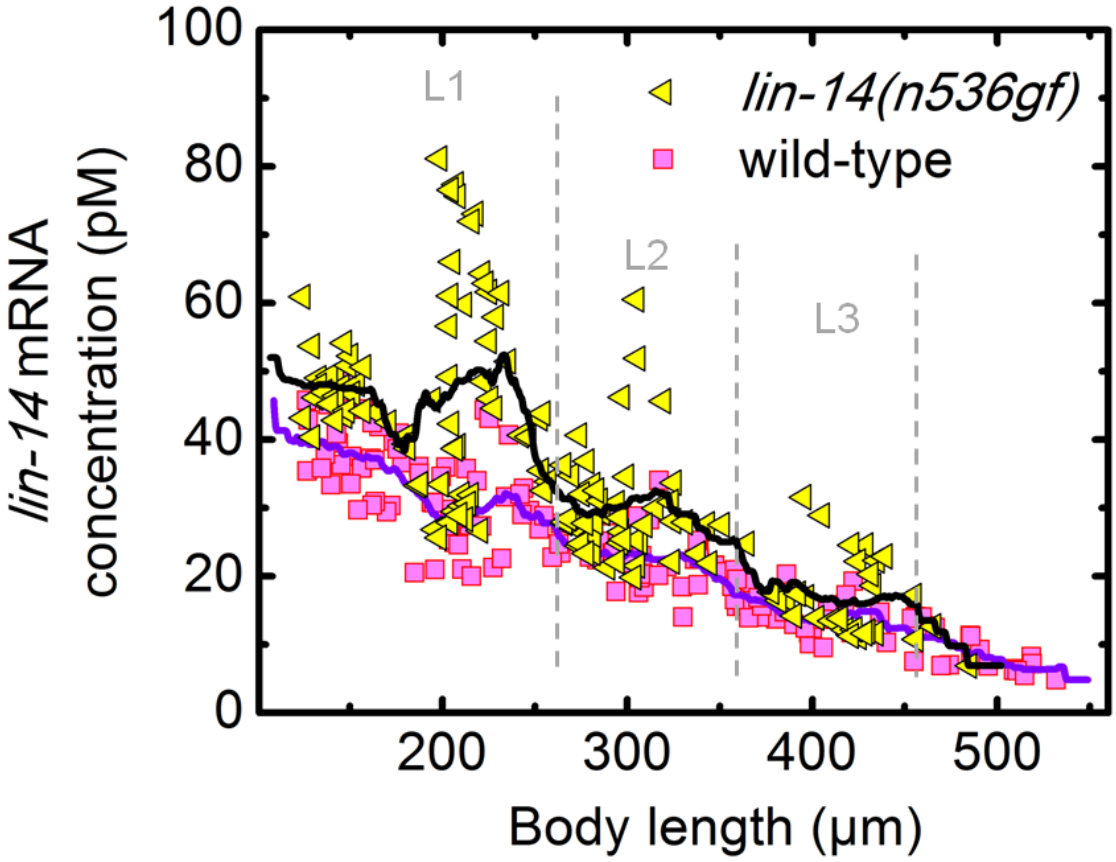

Supplementary Figure 4.12: *lin-14* mRNA expression in *lin-14(n536gf)* mutants. Curves indicate simple moving averages of the corresponding data points within a bin of size 36 μm. Wild-type data were shown for comparison. Dashed lines separate larval stages.

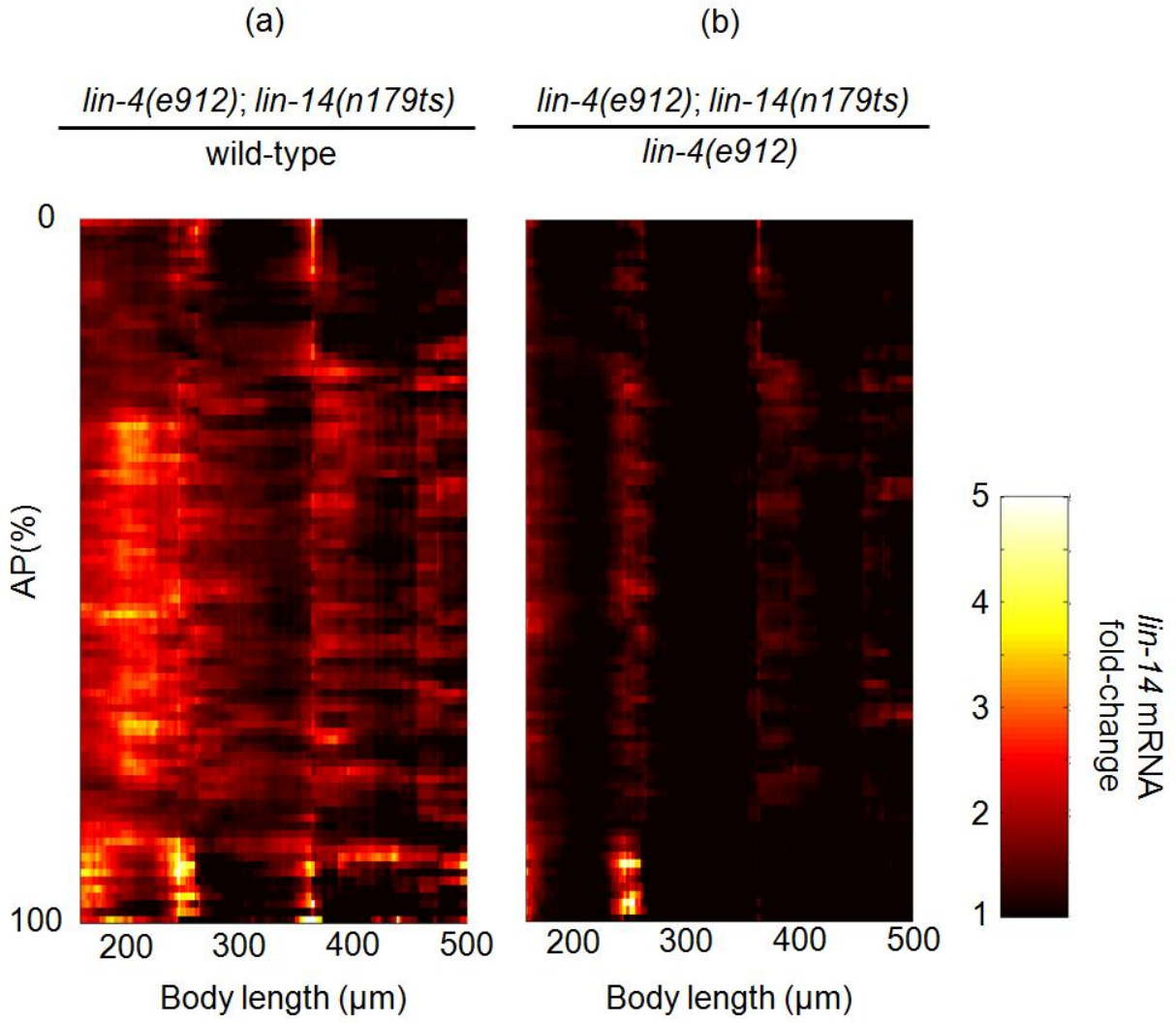

Supplementary Figure 4.13: Functional *lin-14* allele is not required for pulsatile expression of *lin-14*. We asked what the underlying mechanism driving the *lin-14* oscillation in the absence of *lin-4* could be. Since the pulsatile *lin-14* expressions are present in non-dividing cells (Fig. 4.3b), they are unlikely driven by the cell cycle machinery. A phenotypic feature of *lin-4(e912)* and *lin-14(n355gf)* animals is that they exhibit reiterating L1 fates (hatch→L1→L1→L1→) [43,44], thus it is possible that either the oscillatory *lin-14* transcript levels are merely a repetition of pulses implemented by an upstream regulator that is L1 fate specific, or alternatively, LIN-14 protein itself might mediate an auto-regulatory negative feedback loop [131]. To examine these possibilities,

we generated a fold-change map of *lin-14* transcript levels between *lin-4(e912); lin-14(n179ts)* and wild-type animals (**a**), and between *lin-4(e912); lin-14(n179ts)* and *lin-4(e912)* animals (**b**). AP(%) indicate relative position along AP axis (0%-head, 100%-tail). The height of each bin is 1% and a moving average (bin; 36µm) is applied in x-direction. *lin-14(n179ts)* is a temperature-sensitive loss-of-function allele [44]. As a consequence, these animals exhibit a "precocious" phenotype by skipping the L1 specific larval program (hatch→L2→L3→L4→) [44] at a restrictive temperature of 25^{o}C. We can reliably quantify *lin-14* transcription activity because the *lin-14(n179ts)* mutation is not a nonsense mutation [132] and therefore escapes nonsense mediated decay [133]. We found that *lin-14* transcript levels oscillated in *lin-4(e912); lin-14(n179ts)* animals similarly to the observed oscillations in *lin-4(e912)* animals but not to the graded expression in wild-types, suggesting that *lin-14* oscillations are not caused by a L1 specific program. In addition, *lin-14* oscillations are unlikely to be driven by LIN-14 mediated feedback mechanism because a functional *lin-14* allele is not required. These results led us to hypothesize that *lin-14* expression is driven by an external periodic cue.

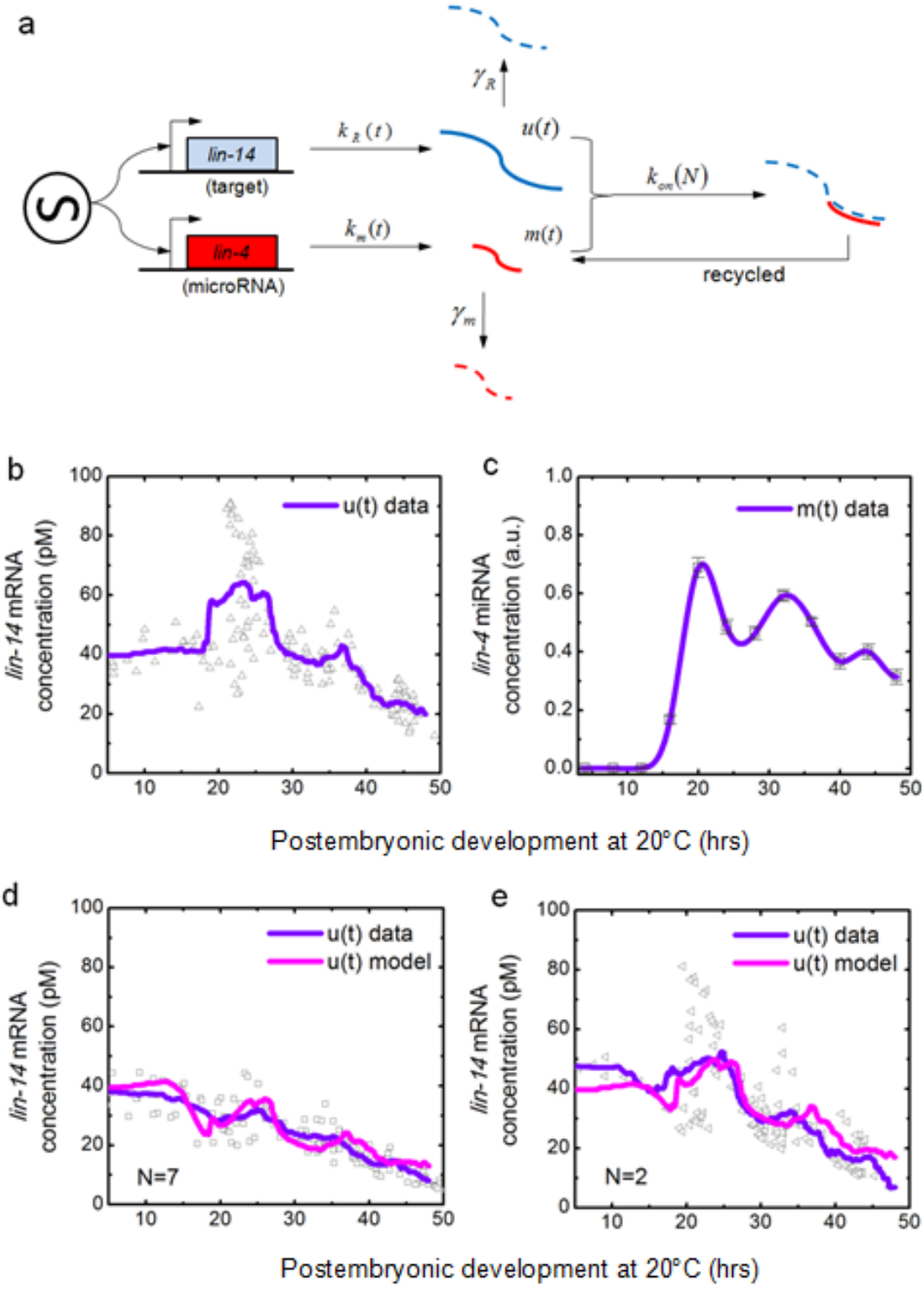
a
lin-14
(target)
lin-4
(microRNA)
u(t)
m(t)
recycled
b
lin-14 mRNA concentration (pM)
u(t) data
c
lin-4 miRNA concentration (a.u.)
m(t) data
Postembryonic development at 20°C (hrs)
d
u(t) data
u(t) model
N=7
e
N=2
Postembryonic development at 20°C (hrs)

Supplementary Figure 4.14: Steady-state miR-IFFL model and data fitting. a, We built a mathematical model to characterize the dynamics of target gene level *u* in the presence of miRNA level *m*. We assumed a time-variant production of the target mRNA $k_R(t)$ and miRNA $k_m(t)$, with decays described by first-order constant rates γ_R and γ_m respectively. We also assumed irreversible second-order miRNA-mediated target transcript degradation kinetics with a rate constant k_{on}. The rate k_{on} depends on the strength of the miRNA-target interaction which is proportional to the number of miRNA complementary elements *N* of the target transcript (thus $k_{on}(N=0) = 0$ in both *lin-4(e912)* and *lin-14(n355gf)* strains). Assuming that the *lin-14* mRNA concentration is in steady-state, we find a simple analytical expression for steady state *lin-14* mRNA concentration $u_{st}(t)$

$$0 = \dot{u}(t) = k_R(t) - k_{on} \cdot u_{st}(t) \cdot m(t) - \gamma_R \cdot u_{st}(t)$$

$$0 = \dot{m}(t) = k_m(t) - \gamma_m \cdot m(t)$$

$$\Rightarrow u_{st}(t) = \frac{k_R(t) / \gamma_R}{1 + \alpha \cdot m(t)} \qquad [2]$$

where $\alpha \equiv \frac{k_{on}}{\gamma_R}$. The term $\alpha \cdot m(t)$ describes the miRNA "efficacy" [134], which is the product of $\frac{k_{on}}{\gamma_R}$ and the miRNA level *m(t)* . In Eqn. [2], "fold-repression" thus appears as $1+\alpha \cdot m(t)$. **b**-**c**, We directly used the moving-averaged *lin-14* mRNA concentration of *lin-14(n355gf)* animals (purple curve in (**b**) and Supplementary Fig. 4.11) to infer $\frac{k_R(t)}{\gamma_R}$, since $\frac{k_R(t)}{\gamma_R} = u_{st}(t)$ given that $k_{on}(N=0) = 0$ for this strain. To find $m(t)$, we used our spline-fitted experimental measurement of mature *lin-4* from *lin-14(n355gf)* animals

(purple curve in (**c**)). **d**-**e**, We then determined the value of $\alpha \equiv \frac{k_{on}}{\gamma_R}$ by fitting our steady-state model $u_{st}(t)$ to our experimental data for *N* = 7 (wild-type, (**d**) and Fig. 4.2e) and *N* = 2 (*lin-14(n536gf)*, (**e**) and Supplementary Fig. 4.12).

The best fit values obtained were: $k_{on}(N = 7)/\gamma_R$ = (1.66 ± 0.14) and $k_{on}(N=2)/\gamma_R$ = (0.56 ± 0.09). Errors indicate 95% confidence intervals, which were obtained by Monte Carlo simulation (1,000 trials). From this result, we speculate that each of the LCE in *lin-14* 3'-UTR equally contributes to the overall strength of miRNA-target interaction, parameterized as k_{on} in our model (Fig. 4.4c).

a

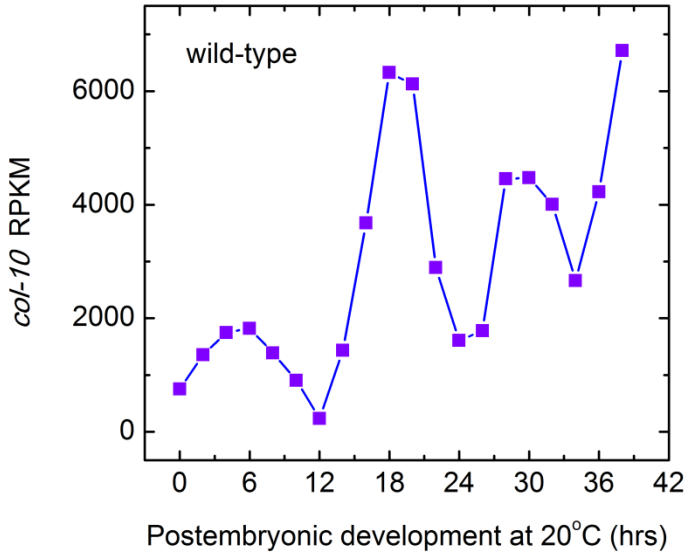
wild-type
col-10 RPKM
6000
4000
2000
0
0
6
12
18
24
30
36
42
Postembryonic development at 20°C (hrs)

b

c

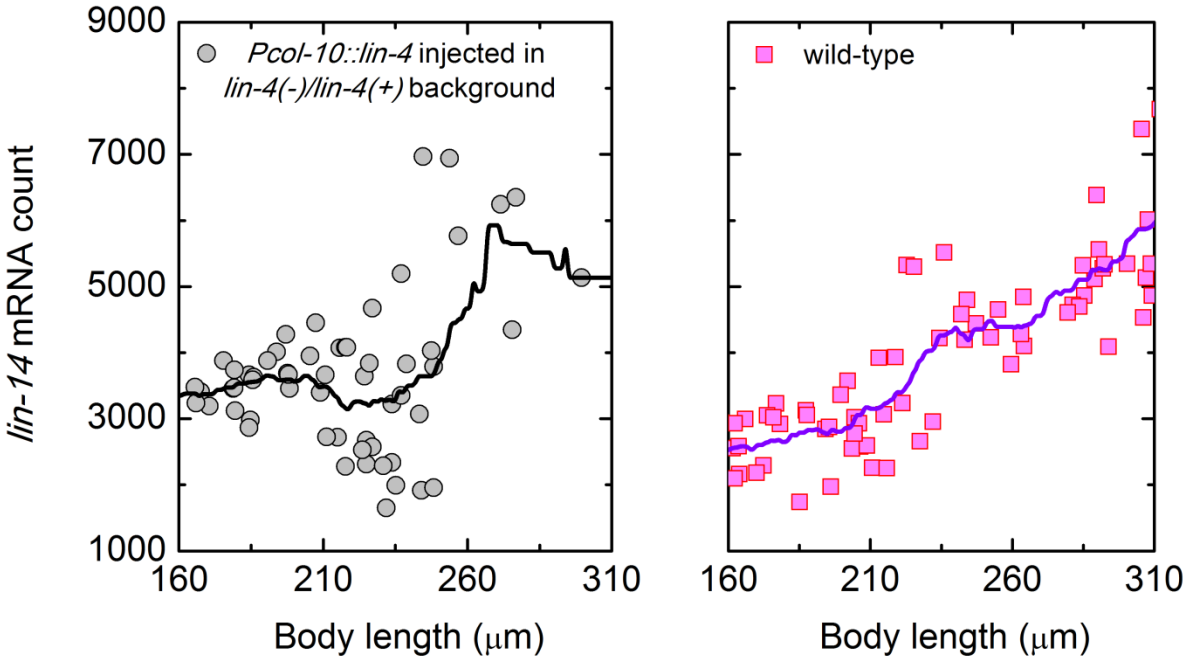
Pcol-10::lin-4 injected in
lin-4(-)/lin-4(+) background
lin-14 mRNA count
9000
7000
5000
3000
1000
160
210
260
310
Body length (μm)
wild-type
160
210
260
310
Body length (μm)

Supplementary Figure 4.15: *lin-14* mRNA expression is over-damped when *lin-4* miRNA is over-expressed. Our model described in 4.7 Supplementary Information and Supplementary Fig. 4.14 predicts that the miRNA "efficacy" $\alpha \cdot m(t)$, where $\alpha \equiv \frac{k_{on}}{\gamma_R}$, is optimally balanced in wild-types. To explore suboptimal conditions, namely the upper right corner of the miR-IFFL performance parameter space in Fig. 4.4d, we asked how *lin-14* mRNA expression dynamics would change when *lin-4* miRNA is over-expressed. *col-10* is a molting gene that is known to be expressed periodically at high levels in the hypodermal tissue and from our RNA-Seq data (**a**) we found its oscillatory phase to be identical to that of *lin-4* miRNA expression (Fig. 4.2a). We measured *lin-14* mRNA levels in animals expressing *Pcol-10::lin-4* (pHZ081) in a balanced *lin-4(e912)/mC6* II background [120]. We excluded animals that lost *mC6* balancer by analyzing only the animals expressing gfp (*mC6* carries gfp) so that the synchronous expression of a single endogenous *lin-4* locus and transgene *Pcol-10::lin-4* will increase peak heights of *lin-4* miRNA level. The result would be increased relative fluctuations in *lin-4* miRNA level, leading to an over-damping of *lin-14* mRNA levels according to our model's prediction. This is equivalent to shifting the N=7 asterisk to the right hand side across the dark blue valley in Fig. 4.4d. Although the *col-10* promoter is active only in the hypodermal tissue, it makes up a large fraction of the total animal volume and we indeed observed a transient decrease in the total number of *lin-14* mRNA in these transgenic animals of body lengths 210µm - 250 µm (**b**) compared to the smooth dynamics seen in wild-types (**c**). Curves in **b**-**c** indicate simple moving averages of the corresponding data points within a bin of size 36 µm.

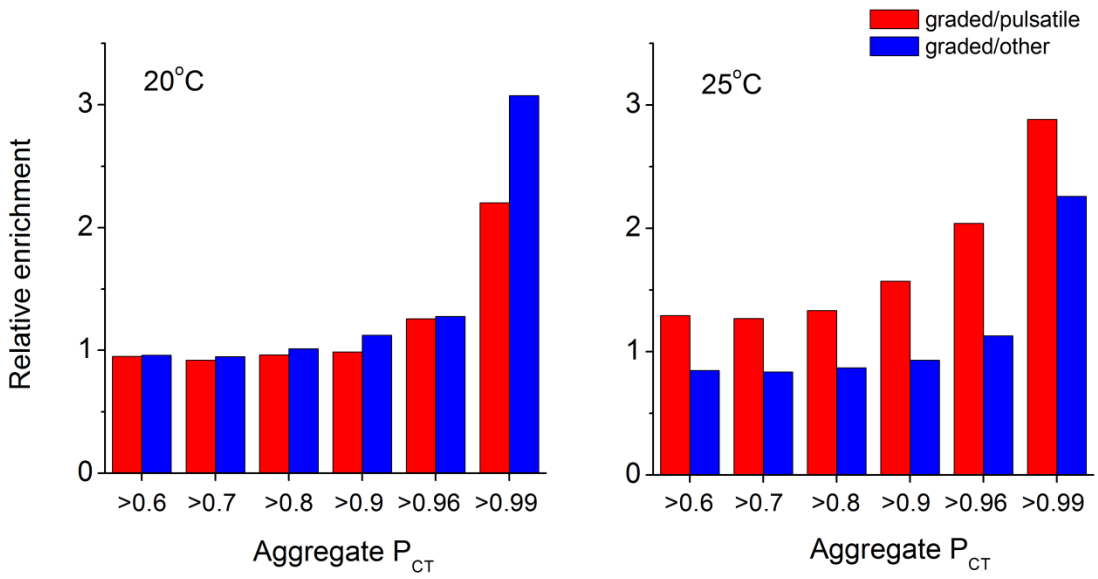

Supplementary Figure 4.16: Predicted conserved miRNA target genes are more enriched in the graded class. To test whether miRNA regulation of target genes is a general mechanism to prevent temporal fluctuations, we asked whether the graded class was enriched with the predicted conserved *C. elegans* miRNA targets listed in WormTargetScan (v6.0) [123] with statistical significance. Predicted targets of miRNAs can be sorted by decreasing "Aggregate Probability of Conserved Targeting (Aggregate P_{CT})" which reflects the likelihood of the targeting interactions to be more effective and consequential to the animal [135]. We calculated "relative enrichment" of the graded class in two ways while varying this P_{CT} threshold: (1) the ratio of the fraction of miRNA target species in graded class to the fraction of miRNA target species in the three pulsatile classes as a whole, shown in red, and (2) the ratio of the fraction of miRNA target species in graded class to the fraction of miRNA target species in the class of genes which were not classified into any of the four dynamical groups ("other"), shown in blue. The fact that both types of "relative enrichment" increase as we limit our analyses to candidate genes that are more likely miRNA targets by increasing P_{CT} threshold suggests that miRNA regulation might in general function to prevent target genes from temporal fluctuations.

4.8 Methods

Strains - C. elegans strains used in this study were N2 (wild-type), MT873 (*lin-4(e912)II*), MT355 (*lin-14(n355gf)X*), MT536 (*lin-14(n536gf)X*), MT1848 (*lin-14(n360)X*), MT723 (*lin-4(e912)II; lin-14(n179ts)X*), VT1072 (*unc-119(ed3)III; maIs134[unc-119(+) + Plin-4::GFP*]) and PD7190 (*lin-4(e912)/mC6 II; pha-1(e2123ts) III; rde-1(ne300) V; pHZ081 [pcol-10::lin-4::let-858_3'UTR]; pC1 [pha-1(+)]*)

Synchronization and RNA extraction - Wild-type (N2) and mutant nematodes were synchronized by hypochlorite treatment. L1-arrested animals in starvation medium were spotted onto NGM plates with food (OP50 *E. coli* strain) and cultured at 20^{o}C unless otherwise stated. MT723 (*lin-4(e912); lin-14(n179ts)*) animals were always grown at restrictive temperature 25^{o}C. Total RNA was isolated from synchronized larval populations using Trizol (Invitrogen). Each sample underwent 3 rounds of freeze-thaw cycles for enhanced efficiency.

Poly(A)$^{+}$ RNA-sequencing experiment – Poly(A)$^{+}$ RNA libraries were prepared from total RNA. Reads were aligned using Tophat with Illumina GA pipeline version 1.3 and segment lengths set to 20. We used Cufflinks to annotate these alignments to the *C. elegans* genome release WS190 and to quantify expression levels using default parameters.

Single mRNA FISH - Probe design and hybridization protocol for single molecule mRNA FISH in *C. elegans* larvae was performed as previously described. We used M9 to wash larvae off from plates. Animals were additionally washed twice to empty the gut filled with bacteria and were fixed in 4% formaldehyde 1X PBS for 45 minutes. Fixed animals were permeabilized in 70% ethanol overnight. All probes were coupled to Cy5 (GE Amersham) which gave us high signal to background ratio in all larval stages. Hybridized animals were imaged using a Nikon Ti-E inverted fluorescence microscope equipped with a 100X oil-immersion objective and a Photometrics Pixis 1024 CCD camera using MetaMorph software (Molecular Devices, Downington, PA) and appropriate optical filters for Cy5 and DAPI. Data analyses and model simulations were

carried out semi-automatically with the aid of custom software written in MATLAB (Mathworks).

miRNA TaqMan PCR assay – miRNA TaqMan PCR assay for *lin-4* miRNA quantification was performed following the instructions from the manufacturer (Applied Biosystems) using Light Cycler 480 II Real-time PCR machine (Roche). We used sn2343 and U18 for normalization controls.

4.9 More on expression fluctuations: rRNA transcription

Since the majority of the transcriptome exhibits pulsatile dynamics during *C. elegans* post-embryonic development, we questioned whether the ribosomal RNA (rRNA) expression dynamics would show similar characteristics. rRNA is the RNA component of the ribosome, the key enzyme that drives protein chain synthesis from mRNA template, a process known as translation [136]. In fact, rRNA is one of the few RNA species that are present in all living cells regardless of species and accounts for >80% of the total RNA within cells. A ribosome is made of two (large and small) subunits. During translation, the template mRNA is sandwiched between these two subunits and protein chain formation is catalyzed. rRNAs are thought to be critical to such catalytic activities while the rest of the ribosomal proteins merely function as a scaffold. Eukaryotic rRNA genes (rDNA) form tandem repeats and are transcribed by either RNA polymerase I (Pol I) or RNA polymerase III (Pol III). Pol I transcribes the tandemly arrayed rRNA genes that encode 18S, 5.8S and 26S, while Pol III transcribes rRNA gene that encodes 5S, respectively. 26S, 5.8S and 5S later become part of the large subunit while 18S becomes part of the small subunit.

rRNA transcription takes place in the nucleolus, a non-membrane bound sub-nuclear structure. In *C. elegans*, Pol I transcribes pre-rRNAs carrying 18S, 5.8S and 26S from ~55 rDNA tandem repeats located at the end of chromosome I which immediately undergo multiple processing steps (Fig. 4.5) [137]. The cleaved “mature” 18S, 5.8S and

26S rRNAs are then exported to the cytoplasm and incorporated to free ribosomal subunits. On the other hand, 5S rRNA is transcribed by Pol III from ~110 rDNA tandem array located at chromosome V and undergoes similar processing steps.

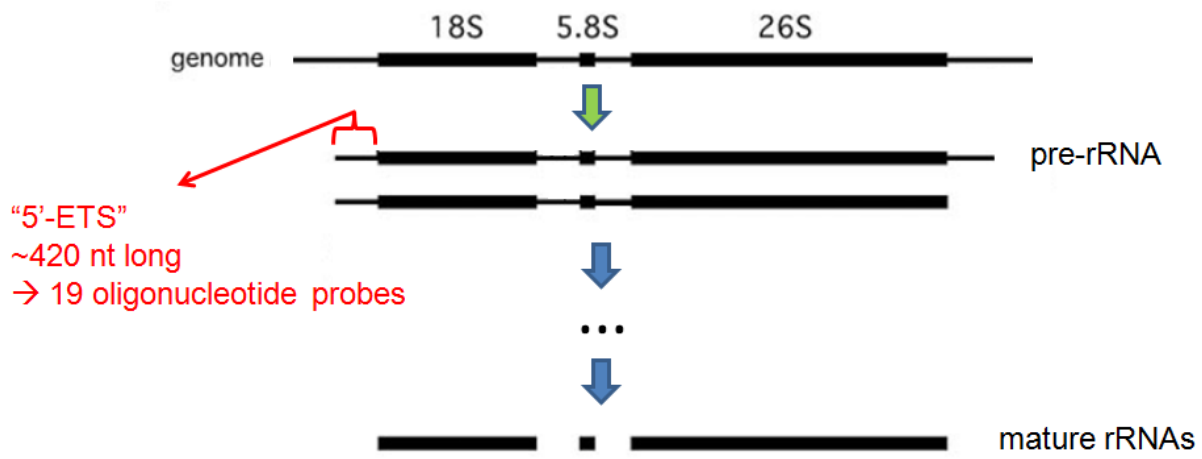

Figure 4.5 Pre-rRNA processing pathway in *C. elegans*. Figure adopted from Saijou, E., Fujiwara, T., Suzaki, T., Inoue, K. and Sakamoto, H. RBD-1, a nucleolar RNA-binding protein, is essential for *Caenorhabditis elegans* early development through 18S ribosomal RNA processing. *Nucleic Acids Research* **32**, 1028-1036 (2004) [137].

Measuring pre-rRNA abundance in single cells of *C. elegans*

To measure the rRNA transcription dynamics in *C. elegans*, we designed single molecule RNA FISH probe library to target the 5' external transcribed spacer (5'-ETS), a non-functional piece of RNA rapidly cleaved during rRNA maturation process, of the pre-rRNA transcribed by Pol I (Fig. 4.5) [137]. The *C. elegans* pre-rRNA 5'-ETS is ~420

nt long which was enough for us to design 19 singly labeled oligonucleotide probes. Since pre-rRNA transcripts are rapidly processed and cleaved in the nucleolus, the fluorescent signal from 5'-ETS probes will be localized in the nucleolus and the net strength of fluorescent signal from these hybridized probes will be an accurate readout of Pol I activity. Indeed this is what we have found (Fig. 4.6). Because of their high abundance, however, the pre-rRNA transcripts appeared as fluorescent blobs rather than distinguishable spots inside each nucleus.

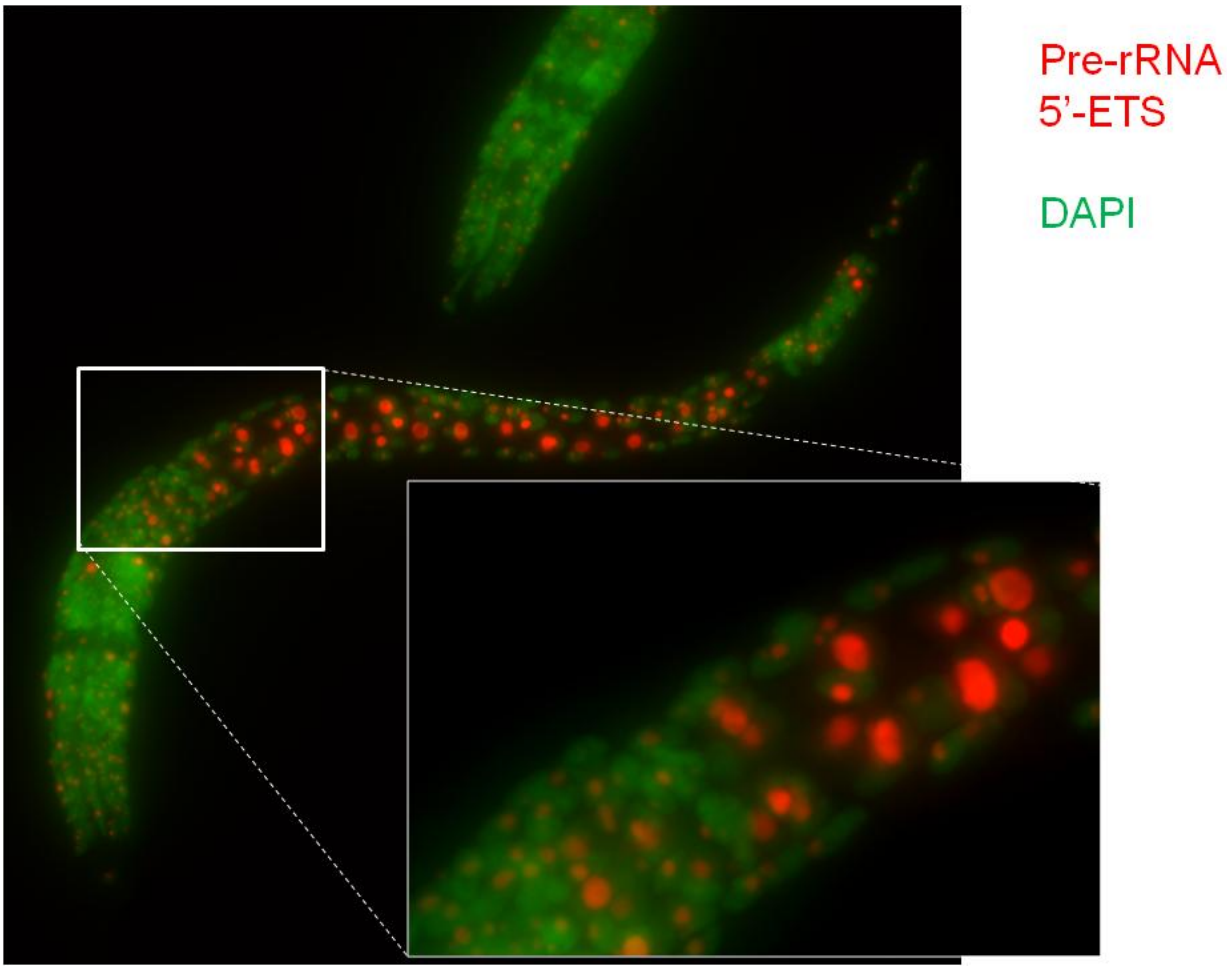

Figure 4.6 Pre-rRNA 5'-ETS of an L1 *C. elegans* larva. Red – Pre-rRNA 5'-ETS and green – DAPI signal, respectively. The fluorescent signal from 5'-ETS is clearly confined within individual nucleus stained with DAPI. The 5'-ETS probe signals in intestinal cells much larger and brighter than those of other cells. Maximum intensity Z-projection of a representative stack image of wild-type L1 animal is shown.

In an attempt to quantify the amount (in arbitrary units) of pre-rRNA 5'-ETS transcripts in each nucleus, we summed up the voxel intensities of fluorescent blobs within the nucleus and subtracted it with the worm background signal. To avoid any signal variability which may result from the day-to-day variance of the microscope setup, we further normalized this value to the background signal to cancel out such extrinsic contributions in our calculations (Fig. 4.7).

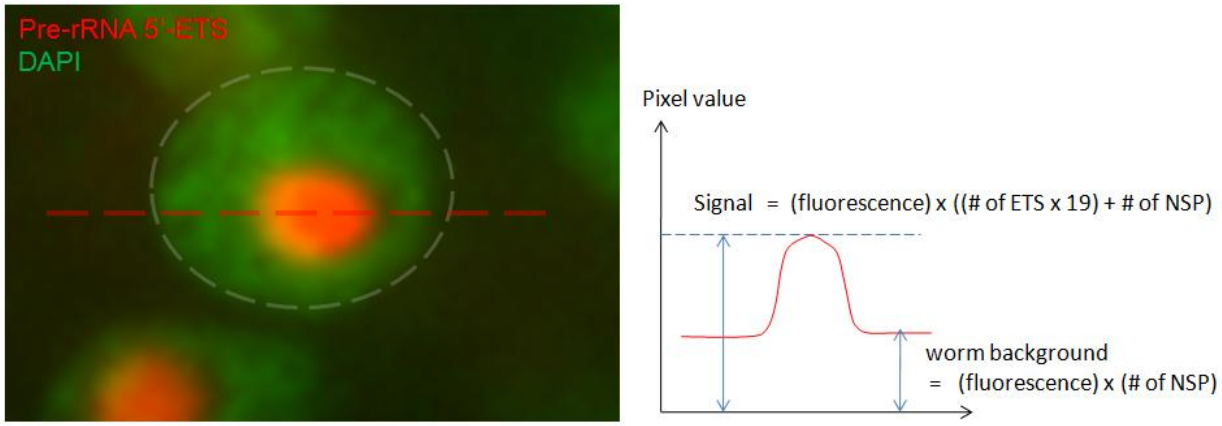

Net signal = (signal – worm background) / (worm background)
= (# of ETS x 19) / # of NSP
$\propto$ # of ETS

Figure 4.7 Quantification of pre-rRNA abundance. Upper left panel shows a nucleus of a hypodermal cell stained with DAPI in green (boundary outlined with grey dashed line) carrying a pre-rRNA 5'-ETS fluorescent blob signal in red. This blob presumably stains the nucleolus. A two-dimensional schematic of the signal intensity profile along the red dashed line is shown in the upper right panel. "Signal" is defined as the sum of the fluorescent signal from hybridized probes (# of ETS x 19) and the non-specifically bound probes (# of NSP) in the background. The "fluorescence" here depends on the quantum efficiency of fluorophore used and the microscope setup. The "net signal" which would be proportional to pre-rRNA abundance is then calculated as shown in the lower panel.

Discretized up-regulation of pre-rRNA expression during larval growth

We first focused on the anterior intestinal cells int2, int3 and int4, dorsal and ventral each. The nuclei of these cells can be easily identified by DAPI staining without any cell specific marker because of their exclusively large size, regularly spaced orientation and unique texture. At late L1, int3 and int4 become binucleate, carrying two nuclei, while int2 remain mononucleate [128] (more explanations follow below), and in such cases, the expression levels of the two were summed up. Surprisingly we have found discrete jumps in the levels of pre-rRNA 5'-ETS exhibiting an overall increase with kinks in all of the three cell types (Fig. 4.8a). During early L1, pre-rRNA 5'-ETS levels remain relatively constant followed by an abrupt 4-fold increase at late L1. The resulting expressions level again remains relatively constant but is soon followed by another 3 to 4-fold jump at late L2 stage.

NCL-1 is a key regulator that represses Pol I and Pol III transcription activity and reduces rRNA synthesis in *C. elegans* [138]. We tested whether *ncl-1* had any role in controlling these expression level jumps by performing the same measurement in *ncl-1(e1942)* loss-of-function mutants (Fig. 4.8b). Although we have found the expression level kinks to be slightly sharpened, the overall pre-rRNA 5'-ETS expression levels were almost identical to that of wild-type animals. In fact, this result was consistent with previous immuno-fluorescence study which has shown that NCL-1 is not detectable in the intestinal cells [138].

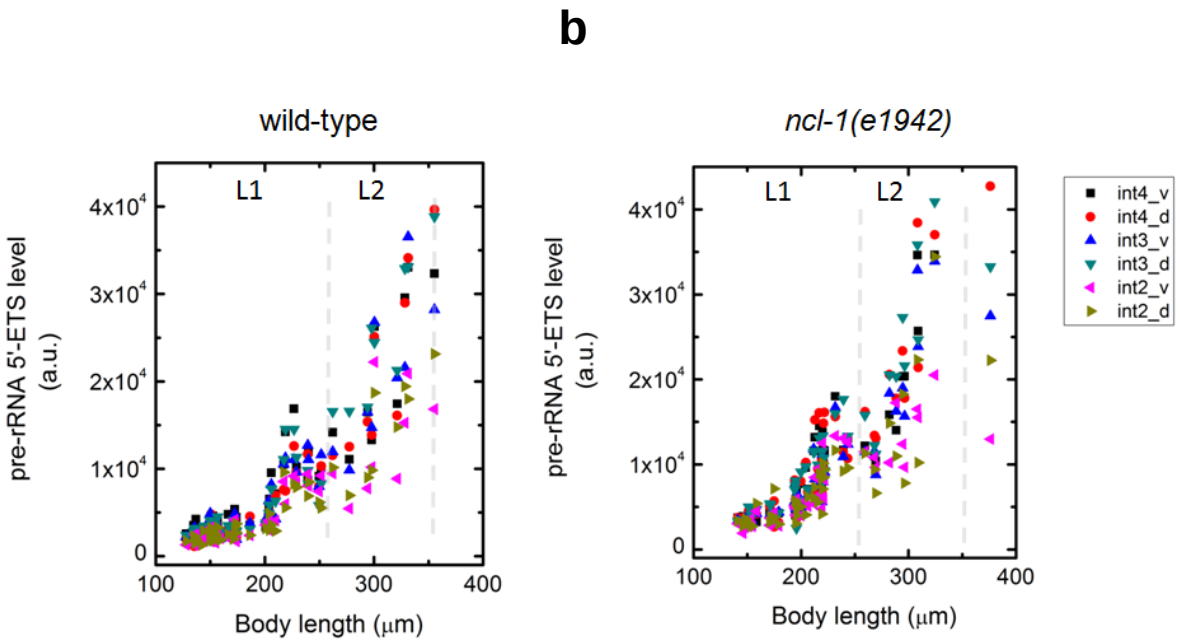

Figure 4.8 Pre-rRNA 5'-ETS expression levels in anterior intestinal cells of (a) wild-type and (b) *ncl-1(e1942)* mutant animals.

As mentioned above, during post-embryonic development, the intestinal cells become binucleate. Prior to the first molt (L1 molt), dorsal and ventral int3, int4, int5, int6 and int7 cells (10 cells) become binucleate. Furthremore, during each molt, individual nuclei of these binucleate cells undergo endoreduplication. Endoreduplication is a process where the genome replicates in the absence of cell division, and it occurs repeatedly at each molt in *C. elegans* intestinal cells until the last molt (L4 molt) resulting in 32C/nucleus ploidy [128].

Therefore, it is possible that the observed jumps in the pre-rRNA 5'-ETS expression levels are caused by either binucleation or endoreduplication, which could potentially lead to a sudden increase in the copy number of genes and thus their transcription. To test this possibility we re-plotted the data from int3 and int4 in Fig. 4.8a, this time labeling mono-nucleated cells separately from bi-nucleated cells and showing pre-rRNA 5'ETS levels of individual nucleus (Fig. 4.9a). We found such jumps to occur in mononucleated nuclei at body lengths of 200 µm-250 µm, indicating that the discrete pre-rRNA 5'-ETS expression level jumps we have observed are not due to binucleation

events. Furthermore, since endoreduplications occur in binucleated cells, we were also able to rule out endoreduplication as a cause of discrete pre-rRNA 5'-ETS expression level jumps .

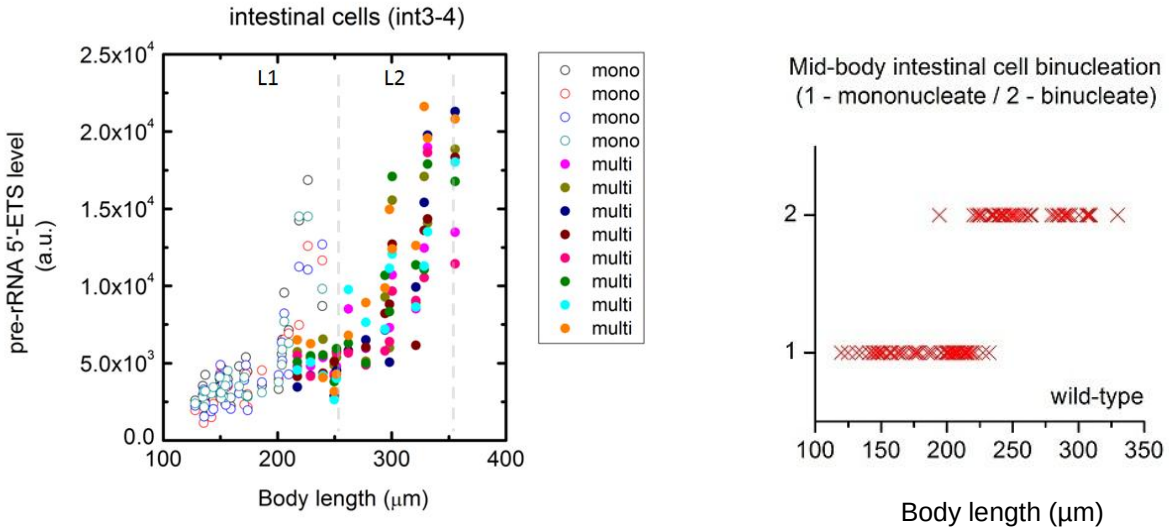

Figure 4.9 *Left* - Expression levels of pre-rRNA 5'-ETS in individual nucleus of int3 and int4, dorsal and ventral. Each nucleus is labeled "mono" if it is from a mononucleate cell, or "multi" if it is from a binucleate cell. *Right* – The binucleation of intestinal cells in the mid-body including int3 and int4 occurs prior to molting (body length ~ 250μm).

We next questioned whether this expression dynamics would be observed in other cell types. We chose two hypodermal cells in the tail tip, hyp9 and hyp10. hyp10 is a mononucleate cell while hyp10 is binucleate, and neither of them divides nor undergoes endoreduplication during postembryonic growth [70] (Fig. 4.10 top). In both hyp9 and hyp10, we did not observe any significant jumps of pre-rRNA 5'-ETS expression levels. However, in the *ncl-1(e1942)* loss-of-function mutant strains, these cells exhibited discretized up-regulation of pre-rRNA 5'-ETS, similar to that of intestinal cells in both wild-type and *ncl-1(e1942)* mutants (Fig. 4.10 bottom).

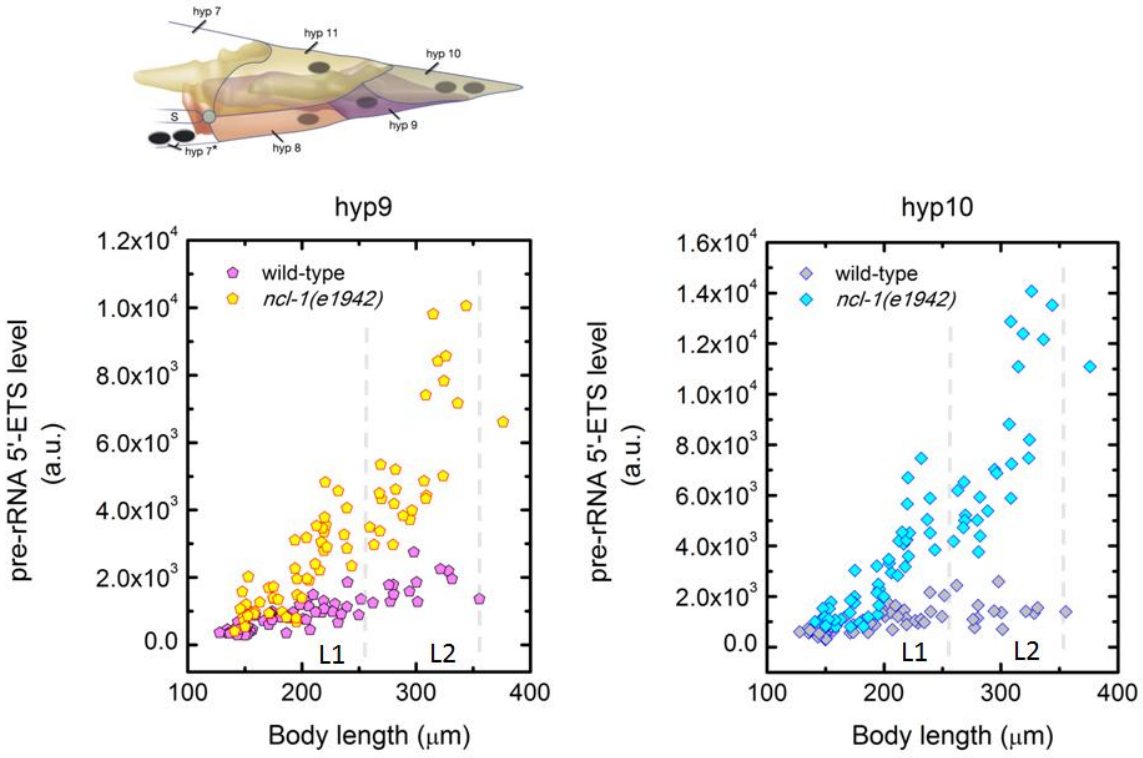

Figure 4.10 *Upper panel* – Anatomy of *C. elegans* tail hypodermis. Dark circles indicate nuclei. Cartoon adopted from Altun, Z.F. and Hall, D.H. 2009. Epithelial system, hypodermis. In *WormAtlas*. doi:10.3908/wormatlas.1.13 [139]. *Lower panels* - Pre-rRNA 5'-ETS expression levels in hyp9 and hyp10 cells of wild-type animals exhibit no obvious jumps. However, in *ncl-1(e1942)* mutants, Pol I transcription activity is derepressed in these cells, causing pre-rRNA 5'-ETS expression levels to jump approximately once per larval stage.

It is intriguing to find pulsatile transcription dynamics present in both rRNA and the majority of transcriptome. These observations suggest that cyclic processes underlie the core of gene expression programs during post-embryonic development of *C. elegans*. We hope the data presented in this section inspire future work to identify what the key drivers of such that pulsatile gene expressions are and its physiological consequences. We also hope future studies would reveal how additional layers of regulation, such as NCL-1 dependent rRNA repression in cell type dependent manner, lead to proper execution of numerous developmental programs in *C. elegans*.

4.10 Acknowledgement

We thank V. Ambros, H. R. Horvitz, G. Ruvkun and J. Gore for helpful discussions and advice. We thank S. Itzkovitz, J. P. Junker, G. Neuert, J. van Zon, A. Sahay and C. Engert for a critical reading of the manuscript. We thank the MIT BioMicro Center for Illumina sample preparation and sequencing experiments. We also thank the Biopolymers & Proteomics Core Facility of the MIT Koch Institute for Integrative Cancer Research for probe purification. This work was supported by a NIH Pioneer award (1DP1OD003936) to A.v.O. and Mogam Science Scholarship to D. K. Several nematode strains used in this work were provided by the Caenorhabditis Genetics Center, which is funded by the NIH National Center for Research Resources (NCRR) and Andrew Fire laboratory.

Bibliography

[1] Chalfie, M., Tu, Y., Euskirchen, G., Ward, W. W. & Prasher, D. C. Green fluorescent protein as a marker for gene expression. *Science* **263**, 802-805 (1994).

[2] Elowitz, M. B., Levine, A. J., Siggia, E. D. & Swain, P. S. Stochastic gene expression in a single cell. *Science* **297**, 1183-1186 (2002).

[3] Deniz, A. A., Mukhopadhyay, S. & Lemke, E. A. Single-molecule biophysics: at the interface of biology, physics and chemistry. *J. R. Soc. Interface* **5**, 15-45 (2008).

[4] Itzkovitz, S., Blat, I. C., Jacks, T., Clevers, H. & van Oudenaarden, A. Optimality in the development of intestinal crypts. *Cell* **148**, 608-619 (2012).

[5] Fuchs, Y. & Steller, H. Programmed cell death in animal development and disease. *Cell* **147**, 742-58 (2011).

[6] Huynh, J.-R & Johnston, D. St. The origin of asymmetry: early polarisation of the *Drosophila* germline cyst and oocyte. *Current Biology* **14**, R438-R449 (2004).

[7] Goldstein, B. & Hird, S. N. Specification of the anteroposterior axis in *Caenorhabditis elegans*. *Development* **122**, 1467-1474 (1996).

[8] Spemann, H. *Embryonic Development and Induction* (Hafner Publishing Company, New York, 1962).

[9] Turing, A. M. The chemical basis of morphogenesis. *Philosophical Transactions of the Royal Society of London, Series B, Biological Sciences* **237**, 37-72 (1952).

[10] Oates, A. C., Gorfinkiel, N., González-Gaitán, M. & Heisenberg, C.-P. Quantitative approaches in developmental biology. *Nature Rev. Genet.* **10**, 517-530 (2009).

[11] Rogers, K. W. & Schier, A. F. Morphogen gradients: from generation to interpretation. *Annu. Rev. Cell Dev. Biol.* **27**, 377-407 (2011).

[12] Gurdon, J. B. & Bourillot, P. –Y. Morphogen gradient interpretation. *Nature* **413**, 797-803 (2001).

[13] Tabata, T. Genetics of morphogen gradients. *Nature Rev. Genet.* **2**, 620-630 (2001).

[14] Reeves, G. T. & Stathopoulos, A. Graded dorsal and differential gene regulation in the Drosophila embryo. *Cold Spring Harb. Perspect. Biol.* **1**:a000836 (2009).

[15] Berleth, T., *et al.* The role of localization of *bicoid* RNA in organizing the anterior pattern of the *Drosophila* embryo. *The EMBO Journal* **7**, 1749-1756 (1988).

[16] Coudreuse, D. Y. M., Roël, G., Betist, M. C., Destrée, O. & Korswagen, H. C. Wnt gradient formation requires retromer function in Wnt-producing cells. *Science* **312**, 921-924 (2006).

[17] Reeves, G. T., *et al*. Dorsal-ventral gene expression in the *Drosophila* embryo reflects the dynamics and precision of the dorsal nuclear gradient. *Dev. Cell.* **22**, 544-557 (2012).

[18] Ben-Zvi, D., Shilo, B.–Z & Barkai, N. Scaling of morphogen gradients. *Curr. Opinion in Genet. Dev.* **21**, 704-710 (2011).

[19] Barkai, N. & Shilo, B.-Z. Robust generation and decoding of morphogen gradients. *Cold Spring Harb. Perspect. Biol.* **1**:a001990 (2009).

[20] Ben-Zvi, D., Shilo, B.-Z, Fainsod, A. & Barkai, N. Scaling of the BMP activation gradient in *Xenopus* embryos. *Nature* **453**, 1205-1211 (2008).

[21] Green, J. L., Inoue, T. & Sternberg, P. W. The *C. elegans* ROR receptor tyrosine kinase, CAM-1, non-autonomously inhibits the Wnt pathway. *Development* **134**, 4053-4062 (2007).

[22] Bovolenta, P., Esteve, P., Ruiz, J. M. Cisneros, E. & Lopez-Rios, J. Beyond Wnt inhibition: new functions of secreted Frizzled-related proteins in development and disease. *Journal of Cell Science* **121**, 737-46 (2008).

[23] Raj, A., van den Bogaard, P., Rifkin, S. A., van Oudenaarden, A. & Tyagi, S. Imaging individual mRNA molecules using multiple singly labeled probes. *Nature Methods* **5**, 877–879 (2008).

[24] Moss, E. G. Heterochronic genes and the nature of developmental time. *Curr. Biol.* **17**, R425-R434 (2007).

[25] Pourquié, O. Clocks regulating developmental processes. *Curr. Opinion in Neurobiol.* **8**, 665-70 (1998).

[26] Tu, B. P. & McKnight, S. L. Metabolic cycles as an underlying basis of biological oscillations. *Nature Rev. Mol. Cell. Biol.* **7**, 696-701 (2006).

[27] Oikonomou, C. & Cross, F. R. Frequency control of cell cycle oscillators. *Curr. Opinion in Genet. Dev.* **20**, 605-612 (2010).

[28] Pando, B. F. & van Oudenaarden, A. Coupling cellular oscillators – circadian and cell division cycles in cyanobacteria. *Curr. Opinion in Genet. Dev.* **20**, 613-618 (2010).

[29] Matsuo, T., *et al*. Control mechanism of the circadian clock for timing of cell division in vivo. *Science* **302**, 255-259 (2003).

[30] Dunlap, J. C. Molecular bases for circadian clocks. *Cell* **96**, 271-290 (1999).

[31] Wang, J. D. & Levin, P. A. Metabolism, cell growth and the bacterial cell cycle. *Nature Rev. Microbiol*. **7**, 822-827 (2009).

[32] Kyriacou, C. P., Oldroyd, M., Wood, J., Sharp, M. & Hill, M. Clock mutations alter developmental timing in *Drosophila. Heredity* **64**, 395-401 (1990).

[33] Temmerman, L., et al. *C. elegans* homologs of insect clock proteins: a tale of many stories. *Ann. N. Y. Acad. Sci.* **1220**, 137-148 (2011).

[34] Kostrouchova, M., Krause, M., Kostrouch, Z. & Rall, J. E. Nuclear hormone receptor CHR3 is a critical regulator of all four larval molts of the nematode *Caenorhabditis elegans*. *PNAS* **98**, 7360-7365 (2001).

[35] Chalfie, M., Horvitz, H. R. & Sulston, J. E. Mutations that lead to reiterations in the cell lineages of *C. elegans. Cell* **24**, 59-69 (1981).

[36] Palmeirim, I., Henrique, D., Ish-Horowicz, D. & Pourquié, O. Avian *hairy* gene expression identifies a molecular clock linked to vertebrate segmentation and somitogenesis. *Cell* **91**, 639-48 (1997).

[37] Moreno-Risueno, M. A., *et al*. Oscillating gene expression determines competence for periodic *Arabidopsis* root branching. *Science* **329**, 1306-1311 (2010).

[38] Rensing, L., Meyer-Grahle, U. & Ruoff, P. Biological timing and the clock metaphor: oscillatory and hourglass mechanisms. *Chronobiol. Intl.* **18**, 329-369 (2001).

[39] Newport, J. & Kirschner, M. A major developmental transition in early *Xenopus* embryos: I. Characterization and timing of cellular changes at the midblastula stage. *Cell* **30**, 675-686 (1982).

[40] Harley, C. B., Futcher, A. B. & Greider, C. W. Telomeres shorten during ageing of human fibroblasts. *Nature* **345**, 458-460 (1990).

[41] Laufer, J. S., Bazzicalupo, P. & Wood, W. B. Segregation of developmental potential in early embryos of *Caenorhabditis elegans*. *Cell* **19**, 569-577 (1980).

[42] Gould, S. J. *Ontogeny and Phylogeny* (Belknap Press of Harvard University Press, 1977).

[43] Ambros, V. & Horvitz, H. R. Heterochronic mutants of the nematode *Caenorhabditis elegans*. *Science* **266**, 409-416 (1984).

[44] Ambros, V. & Horvitz, H. R. The *lin-14* locus of *Caenorhabditis elegans* controls the time of expression of specific postembryonic developmental events. *Genes Dev.* **1**, 398-414 (1987).

[45] Ruvkun, G. & Giusto J. The *Caenorhabditis elegans* heterochronic gene *lin-14* encodes a nuclear protein that forms a temporal developmental switch. *Nature* **338**, 313-319 (1989).

[46] Moss, E. G., Lee, R. C. & Ambros, V. The cold shock domain protein LIN-28 controls developmental timing in *C. elegans* and is regulated by the *lin-4* RNA. *Cell* **88**, 637-646 (1997).

[47] Slack, F. J., *et al*. The *lin-41* RBCC gene acts in the *C. elegans* heterochronic pathway between the *let-7* regulatory RNA and the LIN-29 transcription factor. *Mol. Cell.* **5**, 659-69 (2000).

[48] Shen, X., *et al*. Architecture and inherent robustness of a bacterial cell-cycle control system. *PNAS* **105**, 11340-11345 (2008).

[49] Mangla, K., Dill, D. L. & Horowitz, M. A. Timing robustness in the budding and fission yeast cell cycles. *PLoS One* **5**, e8906 (2010).

[50] Raj, A. & van Oudenaarden, A. *Nature, nurture, or chance: Stochastic gene expression and its consequences. Cell* **135**, 216–226 (2008).

[51] Harbison, C. T., *et al*. Transcriptional regulatory code of a eukaryotic genome. *Nature* **431**, 99-104 (2004).

[52] van Amerongen, R. & Nusse, R. Towards an integrated view of Wnt signaling in development. *Development* **136**, 3205-3214 (2009).

[53] Leyns, L., Bouwmeester, T., Kim, S. H., Piccolo, S. & De Robertis, E. M. Frzb-1 is a secreted antagonist of Wnt signaling expressed in the Spemann organizer. *Cell* **88**, 747-756 (1997).

[54] Niehrs, C. Function and biological roles of the Dickkopf family of Wnt modulators. *Oncogene* **25**, 7469-7481 (2006).

[55] Kim, C. H., *et al.* Repressor activity of Headless/Tcf3 is essential for vertebrate head formation. *Nature* **407**, 913-916 (2000).

[56] Kiecker, C. & Niehrs, C. A morphogen gradient of Wnt/β-catenin signalling regulates anteroposterior neural patterning in *Xenopus*. *Development* **128**, 4189-4201 (2001).

[57] Tendeng, C. & Houart, C. Cloning and embryonic expression of five distinct *sfrp* genes in the zebrafish *Danio rerio*. *Gene Expr Patterns* **6**, 761-771 (2006).

[58] Hobmayer, B., *et al.* WNT signalling molecules act in axis formation in the diploblastic metazoan *Hydra*. *Nature* **407**, 186-189 (2000).

[59] Kusserow, A., *et al*. Unexpected complexity of the Wnt gene family in a sea anemone. *Nature* **433**, 156-160 (2005).

[60] Guder, C., *et al*. An ancient Wnt-Dickkopf antagonism in *Hydra*. *Development* **133**, 901-911 (2006).

[61] Lee, P. N., Pang, K., Matus, D. Q. & Martindale, M. Q. A WNT of things to come: evolution of Wnt signaling and polarity in cnidarians. *Semin Cell Dev Biol* **17**, 157-167 (2006).

[62] Petersen, C. P. & Reddien, P. W. Smed-β-catenin-1 is required for anteroposterior blastema polarity in planarian regeneration. *Science* **319**, 327-330 (2008).

[63] Petersen, C. P. & Reddien, P. W. Wnt signaling and the polarity of the primary body axis. *Cell* **139**, 1056-1068 (2009).

[64] Korswagen, H. C. Canonical and non-canonical Wnt signaling pathways in *Caenorhabditis elegans*: variations on a common signaling theme. *Bioessays* **24**, 801-810 (2002).

[65] Silhankova, M. & Korswagen, H. C. Migration of neuronal cells along the anterior-posterior body axis of *C. elegans*: Wnts are in control. *Curr Opin Genet Dev* **17**, 320-325 (2007).

[66] Sulston, J. E., Schierenberg, E., White, J. G. & Thomson, J. N. The embryonic cell lineage of the nematode *Caenorhabditis elegans. Dev. Biol.* **100**, 64-119 (1983).

[67] Hedgecock, E. M., Culotti, J. G., Hall, D. H. & Stern, B. D. Genetics of cell and axon migrations in *Caenorhabditis elegans*. *Development* **100**, 365-382 (1987).

[68] Pan, C. L., *et al.* Multiple Wnts and frizzled receptors regulate anteriorly directed cell and growth cone migrations in *Caenorhabditis elegans*. *Dev Cell* **10**, 367-377 (2006).

[69] Zinovyeva, A. Y. & Forrester, W. C. The *C. elegans* Frizzled CFZ-2 is required for cell migration and interacts with multiple Wnt signaling pathways. *Dev Biol* **285**, 447-461 (2005).

[70] Sulston, J. E. & Horvitz, H. R. Post-embryonic cell lineages of the nematode *Caenorhabditis elegans*. *Dev Biol* **56**, 110-156 (1977).

[71] Harris, J., Honigberg, L., Robinson, N. & Kenyon, C. Neuronal cell migration in *C. elegans*: regulation of Hox gene expression and cell position. *Development* **122**, 3117-3131 (1996).

[72] Zinovyeva, A. Y., Yamamoto, Y., Sawa, H. & Forrester, W. C. Complex network of Wnt signaling regulates neuronal migrations during *Caenorhabditis elegans* development. *Genetics* **179**, 1357-1371 (2008).

[73] Herman, M. A., Vassilieva, L. L., Horvitz, H. R., Shaw, J. E. & Herman, R. K. The *C. elegans* gene l*in-44*, which controls the polarity of certain asymmetric cell divisions, encodes a Wnt protein and acts cell nonautonomously. *Cell* **83**, 101-110 (1995).

[74] Whangbo, J. & Kenyon, C. A Wnt signaling system that specifies two patterns of cell migration in *C. elegans*. *Mol Cell* **4**, 851-858 (1999).

[75] Gleason, J. E., Szyleyko, E. A. & Eisenmann, D. M. Multiple redundant Wnt signaling components function in two processes during *C. elegans* vulval development. *Dev Biol* **298**, 442-457 (2006).

[76] Kennerdell, J. R., Fetter, R. D. & Bargmann, C. I. Wnt-Ror signaling to SIA and SIB neurons directs anterior axon guidance and nerve ring placement in *C. elegans*. *Development* **136**, 3801-3810 (2009).

[77] Song, S., *et al.* A Wnt-Frz/Ror-Dsh Pathway Regulates Neurite Outgrowth in *Caenorhabditis elegans*. *PLoS Genet*, **6**, e10010056 (2010).

[78] Thorpe, C. J., Schlesinger, A., Carter, J. C. & Bowerman, B. Wnt signaling polarizes an early *C. elegans* blastomere to distinguish endoderm from mesoderm. *Cell* **90**, 695-705 (1997).

[79] Chong, J. M., Uren, A., Rubin, J. S. & Speicher, D. W. Disulfide bond assignments of secreted Frizzled-related protein-1 provide insights about Frizzled homology and netrin modules. *J Biol Chem* **277**, 5134-5144 (2002).

[80] Adamska, M., *et al*. Structure and expression of conserved Wnt pathway components in the demosponge *Amphimedon queenslandica*. Evol. Dev. **12**, 494-518 (2010).

[81] Maloof, J. N., Whangbo, J., Harris, J. M., Jongeward, G. D. & Kenyon, C. A Wnt signaling pathway controls Hox gene expression and neuroblast migration in *C. elegans*. *Development* **126**, 37-49 (1999).

[82] Prasad, B. C. & Clark, S. G. Wnt signaling establishes anteroposterior neuronal polarity and requires retromer in *C. elegans*. *Development* **133**, 1757-1766 (2006).

[83] Whangbo, J., Harris, J. & Kenyon, C. Multiple levels of regulation specify the polarity of an asymmetric cell division in *C. elegans*. *Development* **127**, 4587-4598 (2000).

[84] Jiang, L. I. & Sternberg, P. W. Interactions of EGF, Wnt and HOM-C genes specify the P12 neuroectoblast fate in *C. elegans*. *Development* **125**, 2337-2347 (1998).

[85] Ch'ng, Q., *et al*. Identification of genes that regulate a left-right asymmetric neuronal migration in *Caenorhabditis elegans*. *Genetics* **164**, 1355-1367 (2003).

[86] Herman, M. A. & Horvitz, H. R. The *Caenorhabditis elegans* gene *lin-44* controls the polarity of asymmetric cell divisions. *Development* **120**, 1035-1047 (1994).

[87] Kawano, Y. & Kypta, R. Secreted antagonists of the Wnt signalling pathway. *J Cell Sci* **116**, 2627-2634 (2003).

[88] Rodriguez, J., *et al.* SFRP1 regulates the growth of retinal ganglion cell axons through the Fz2 receptor. *Nat Neurosci* **8**, 1301-1309 (2005).

[89] Mii, Y. & Taira, M. Secreted Frizzled-related proteins enhance the diffusion of Wnt ligands and expand their signalling range. *Development* **136**, 4083-4088 (2009).

[90] Bänziger, C., *et al.* Wntless, a conserved membrane protein dedicated to the secretion of Wnt proteins from signaling cells. *Cell* **125**, 509-522 (2006).

[91] Yang, P. T., *et al.* Wnt signaling requires retromer-dependent recycling of MIG-14/Wntless in Wnt-producing cells. *Dev Cell* **14**, 140-147 (2008).

[92] Mello, C. & Fire, A. DNA transformation. *Methods Cell Biol* **48**, 451-482 (1995).

[93] Goldstein, B., Takeshita, H., Mizumoto, K. & Sawa, H. Wnt signals can function as positional cues in establishing cell polarity. *Dev Cell* **10**, 391-396 (2006).

[94] Klassen, M. P. & Shen, K. Wnt signaling positions neuromuscular connectivity by inhibiting synapse formation in *C. elegans*. *Cell* **130**, 704-716 (2007).

[95] Guder, C., *et al*. The Wnt code: cnidarians signal the way. *Oncogene* **25**, 7450-7460 (2006).

[96] Inoue, T., *et al. C. elegans* LIN-18 is a Ryk ortholog and functions in parallel to LIN-17/Frizzled in Wnt signaling. *Cell* **118**, 795-806 (2004).

[97] Coudreuse, D. & Korswagen, H. C. The making of Wnt: new insights into Wnt maturation, sorting and secretion. *Development* **134**, 3-12 (2007).

[98] Phillips, B. T., Kidd, A. R., King, R., Hardin, J. & Kimble, J. Reciprocal asymmetry of SYS-1/β-catenin and POP-1/TCF controls asymmetric divisions in *Caenorhabditis elegans*. *PNAS* **104**, 3231-3236 (2007).

[99] Sternberg, P. W. Vulval development, *WormBook*, ed. The *C. elegans* Research Community, WormBook, doi/10.1895/wormbook.1.6.1, http://www.wormbook.org (2005).

[100] Pénigault, J.-B. & Félix, M.-A. High sensitivity of *C. elegans* vulval precursor cells to the dose of posterior Wnts. *Dev. Biol*. **357**, 428-438 (2011).

[101] Myers, T. R. & Greenwald, I. Wnt signal from multiple tissues and *lin-3*/EGF signal from the gonad maintain vulval precursor cell competence in *Caenorhabditis elegans*. *PNAS* **104**, 20368-20373 (2007).

[102] Green, J. L., Inoue, T. & Sternberg, P. W. Opposing Wnt pathways orient cell polarity during organogenesis. *Cell* **134**, 646-56 (2008).

[103] Saffer, A. M., Kim, D., van Oudenaarden, A. & Horvitz, H. R. The *Caenorhabditis elegans* synthetic multivulva genes prevent Ras pathway activation by tightly repressing global ectopic expression of *lin-3* EGF. *PLoS Genet.* **7**, e1002418 (2011).

[104] Eisenmann, D. M. Wnt signaling, *WormBook*, ed. The *C. elegans* Research Community, WormBook, doi/10.1895/wormbook.1.7.1, http://www.wormbook.org (2005).

[105] Lee, R. C., Feinbaum, R. L. & Ambros, V. The *C. elegans* heterochronic gene *lin-4* encodes small RNAs with antisense complementarity to *lin-14*. *Cell* **75**, 843-854 (1993).

[106] Alon, U. *An Introduction to Systems Biology: Design Principles of Biological Circuits.* (Chapman & Hall/ CRC: 2006).

[107] Mortazavi, A., Williams, B. A., McCue, K., Schaeffer, L. & Wold B. Mapping and quantifying mammalian transcriptomes by RNA-Seq. *Nature Methods* **5**, 621-628 (2008).

[108] Gissendanner, C. R., Crossgrove, K., Kraus, K. A., Maina, C. V. & Sluder, A. E. Expression and function of conserved nuclear receptor genes in *Caenorhabditis elegans*. *Dev. Biol*. **266**, 399-416 (2004).

[109] Page, A. P. & Johnstone, I. L. The cuticle, *WormBook*, ed. The *C. elegans* Research Community, WormBook, doi/10.1895/wormbook.1.138.1, http://www.wormbook.org (2007).

[110] Jeon, M., Gardner, H. F., Miller, E. A., Deshler, J. & Rougvie, A. E. Similarity of the *C. elegans* developmental timing protein LIN-42 to circadian rhythm proteins. *Science* **286**, 1141-1146 (1999).

[111] Bagga, S. *et al*. Regulation by *let-7* and *lin-4* miRNAs results in target mRNA degradation. *Cell* **122**, 553-563 (2005).

[112] Wightman, B., Ha, I. & Ruvkun, G. Posttranscriptional regulation of the heterochronic gene *lin-14* by *lin-4* mediates temporal pattern formation in *C. elegans. Cell* **75**, 855-862 (1993).

[113] Olsen, P. H. & Ambros, V. The *lin-4* regulatory RNA controls developmental timing in *Caenorhabditis elegans* by blocking LIN-14 protein synthesis after the initiation of translation. *Dev. Biol.* **216**, 671-680 (1999).

[114] Ambros, V. A hierarchy of regulatory genes controls a larva-to-adult developmental switch in *C. elegans*. *Cell* **57**, 49-57 (1989).

[115] Euling, S. & Ambros, V. Heterochronic genes control cell cycle progress and developmental competence of *C. elegans* vulva precursor cells. *Cell* **84**, 667-676 (1996).

[116] Martinez, N. J. *et al*. Genome-scale spatiotemporal analysis of *Caenorhabditis elegans* microRNA promoter activity. *Genome Res.* **18**, 2005-2015 (2008).

[117] Knight, C. G., Patel, M. N., Azevedo, R. B. R. & Leroi, A. M. A novel mode of ecdysozoan growth in *Caenorhabditis elegans*. *Evolution and Development* **4**, 16-27 (2002).

[118] Hristova, M., Birse, D., Hong, Y. & Ambros, V. The *Caenorhabditis elegans* heterochronic regulator LIN-14 is a novel transcription factor that controls the developmental timing of transcription from the insulin/insulin-like growth factor gene *ins-33* by direct DNA binding. *Mol. Cell. Biol.* **25**, 11059-11072 (2005).

[119] Ruvkun, G. *et al*. Molecular genetics of the *Caenorhabditis elegans* heterochronic gene *lin-14. Genetics* **121**, 501-516 (1989).

[120] Zhang, H. & Fire, A. Z. Cell autonomous specification of temporal identity by *Caenorhabditis elegans* microRNA *lin-4*. *Dev. Biol.* **344**, 603-610 (2010).

[121] Frand, A. R., Russel, S. & Ruvkun, G. Functional genomic analysis of *C. elegans* molting. *PLoS Biol* **3**(10): e312 (2005).

[122] van Wynsberghe, P. M. *et al*. LIN-28 co-transcriptionally binds primary *let-7* to regulate miRNA maturation in *Caenorhabditis elegans*. *Nat. Struct. Mol. Biol.* **18**, 302-308 (2011).

[123] Calvin, H. J., Friedman, R. C., Ruby, J. G., & Bartel, D. P. Formation, regulation and evolution of *Caenorhabditis elegans* 3'UTRs. *Nature* **469**, 97-101 (2011).

[124] Tsang, J., Zhu, J. & van Oudenaarden, A. MicroRNA-mediated feedback and feedforward loops are recurrent network motifs in mammals. *Mol. Cell.* **26**, 753-767 (2007).

[125] Siré, C., Moreno, A. B., Garcia-Chapa, M., López-Moya, J. J. & Segundo, B. S. Diurnal oscillation in the accumulation of *Arabidopsis* microRNAs, miR167, miR168, miR171 and miR398. *FEBS Lett.* **583**, 1039-1044 (2009).

[126] Savageau, M. A. Parameter sensitivity as a criterion for evaluating and comparing the performance of biochemical systems. *Nature* **229**, 542-544 (1971).

[127] Sönnichsen, B. *et al*. Full-genome RNAi profiling of early embryogenesis in *Caenorhabditis elegans*. *Nature* **434**, 462-469 (2005).

[128] Hedgecock, E. M. & White, J. G. Polyploid tissues in the nematode *Caenorhabditis elegans*. *Dev. Biol.* **107**, 128-133 (1985).

[129] Hirsh, D., Oppenheim, D. & Klass, M. Development of the reproductive system of *Caenorhabditis elegans*. *Dev. Biol.* **49**, 200-219 (1976).

[130] Hristova, M., Birse, D., Hong, Y. & Ambros, V. The *Caenorhabditis elegans* heterochronic regulator LIN-14 is a novel transcription factor that controls the developmental timing of transcription from the insulin/insulin-like growth factor gene *ins-33* by direct DNA binding. *Mol. Cell. Biol.* **25**, 11059-11072 (2005).

[131] Bar-Or R. L. *et al.* Generation of oscillations by the p53-Mdm2 feedback loop: a theoretical and experimental study. *PNAS* **97**, 11250-11255 (2000).

[132] Reinhart, B. J. & Ruvkun, G. Isoform-specific mutations in the *Caenorhabditis elegans* heterochronic gene *lin-14* affect stage-specific patterning. *Genetics* **157**, 199-209 (2001).

[133] Pulak R. & Anderson P. mRNA surveillance by the *Caenorhabditis elegans smg* genes. *Genes Dev.* **7**, 1885-1897 (1993).

[134] Larsson, E., Sander, C. & Marks, D. mRNA turnover rate limits siRNA and microRNA efficacy. *Mol. Sys. Biol.* **6**: 433 (2010).

[135] Calvin, H. J., Friedman, R. C., Ruby, J. G., & Bartel, D. P. Formation, regulation and evolution of *Caenorhabditis elegans* 3'UTRs. *Nature* **469**, 97-101 (2011).

[136] Ramakrishnan, V. Ribosome structure and the mechanism of translation. *Cell* **108**, 557-572 (2002).

[137] Saijou, E., Fujiwara, T., Suzaki, T., Inoue, K. & Sakamoto, H. RBD-1, a nucleolar RNA-binding protein, is essential for *Caenorhabditis elegans* early development through 18S ribosomal RNA processing. *Nucleic Acids Res*. **32**, 1028-1036 (2004).

[138] Frank, D. J. & Roth, M. B. *ncl-1* is required for the regulation of cell size and ribosomal RNA synthesis in *Caenorhabditis elegans. The Journal of Cell Biol*. **140,** 1321-1329 (1998).

[139] Altun, Z. F. & Hall, D. H. Epithelial system, hypodermis. In *WormAtlas*. Doi:10.3908/wormatlas.1.13 (2009)